Airborne-based Geophysical Investigation In Dronning Maud Land, Antarctica

Dissertation

zur Erlangung des Grades Dr. rer. nat.
vorgelegt dem Fachbereich Geowissenschaften
der Universität Bremen

von

SVEN RIEDEL

Alfred Wegener Institut für Polar- und Meeresforschung
Bremerhaven

August 28, 2008

Sven Riedel

Alfred-Wegener-Institut für Polar- und Meeresforschung
Columbusstrasse
D-27568 Bremerhaven

gegenwärtige Anschrift:

Christian Albrechts Universität zu Kiel
Institut für Geowissenschaften, Abt. Geophysik
Otto Hahn Platz 1
D-24118 Kiel

Die vorliegende Arbeit ist die inhaltlich unveränderte Fassung der Dissertationsschrift, die 2008 dem Fachbereich Geowissenschaften der Universität Bremen vorgelegt wurde.

Gutachter:
Prof. Dr. H. Miller (Universität Bremen/AWI)
Prof. Dr. H. Villinger (Universität Bremen)
Prüfer:
Prof. Dr. C. Spiegel (Universität Bremen)
Prof. Dr. R. Tiedemann (Universität Bremen/AWI)
Promotionskolloquium:
am 04.Februar 2009

This is about the times, the places,
the people, that have shaped me.

Kurzfassung

Die Antarktis steht bei der Rekonstruktion der Großkontinente Rodinia und Gondwana jeweils im Mittelpunkt erdgeschichtlicher Untersuchungen. Geologische Großstrukturen zeugen von der Bildung und dem Zerfall dieser Superkontinente, jedoch ist deren direkte Erschließung, bedingt durch die Eisbedeckung Antarktikas, nicht möglich und begrenzt sich nur auf spärliche, geologische Aufschlüsse. Daher ermöglichen nur satelliten- und flugzeuggestützte, also indirekte Messungen, eine flächenhafte Erfassung geophysikalischer Daten in polaren Gebieten.

Geologische Untersuchungen manifestieren drei tektonische Großereignisse im Gebiet um Dronning Maud Land (DML): die Grenvillische Orogenese (1.1 Ga) führte zur Bildung Rodinias, die Pan-Afrikanisch-Antarktische Orogenese (EAAO, 500 Ma), gipfelte in der Entstehung von Gondwana sowie dessen Zerfall, um 180 Ma, als letztes tektonisches Großereignis der Region.

Im Rahmen der vorliegenden Arbeit, die Teil des VISA Projektes ist (Validierung, Verdichtung und Interpretation von Satellitendaten zur Bestimmung von Magnetfeld, Schwerefeld und Eismassenhaushalt sowie Krustenstruktur in der Antarktis, gestützt durch flugzeugbasierende und terrestrische Messungen) wurden flugzeuggestützte Daten über einen Zeitraum von 4 Jahren (2001-2005) erhoben, bearbeitet, zusammengefaßt und strukturell analysiert. Die Methodik der Messungen wird vorgestellt, wobei der umfangreichen, rechentechnischen und zeitaufwändigen Bearbeitung der Topographie-, Magnetik- und Schweredaten ein Großteil der Arbeit gewidmet wird.

Die Arbeit resultiert in der flächenhaften Darstellung des Magnet- und Schwerefeldes, sowie der Topographie und bietet erstmals eine einheitliche Datenbasis für die Region um Dronning Maud Land, zwischen 14° W-20° E und 70° S-78.5° S. Weiterführend wurden Verfahren angewandt, wie Wellenlängenfilterungen, Tiefenbestimmungen geologischer Störkörper, Betrachtungen zur Isostasie und Attributbestimmungen, um die geologische Situation umfassend zu analysieren.

Das präsentierte Kartenmaterial zeigt den Verlauf geologisch-tektonischer Großstrukturen, die zwar in der Literatur vermutet und eingehend diskutiert, jedoch in ihrer Lage, Form und Ausprägung nicht vollständig bekannt waren. In Bezug zu bestehenden Daten aus aerogeophysikalischen Befliegungen im Gebiet um Dronning Maud Land, umfassen nahezu 85% der Schwere- und 65% der Magnetikdaten, welche in dieser Arbeit vorgestellt werden, bisher nicht erforschte Regionen. Dies stellt einen großen Beitrag für die geologische Forschung in der Antarktis dar.

Die lithospherische Grenze zwischen dem Archaischen Craton, der Grunehogna Provinz, und dem Proterozoischen- / Früh-Paleozoischen mobilen Gürtel, der Maudheim Provinz, konnte aufgrund der gewonnenen Datenbasis sowie weiterführenden Betrachtungen zur Isostasie und der Curvature-Analyse, interpretiert werden. Die detaillierte Kartierung von Störungszonen weist auf Verlauf und Ausrichtung tektonischer Großereignisse hin. Diese Beobachtungen bilden ein kombiniertes geologisches Modell, welches bestehende Vorstellungen erweitert und verfeinert sowie lokale Aussagen seismologischer, seismischer und geologischer Arbeiten bestätigt.

Abstract

Antarctica represents a key component in the investigation of the geological history and reconstruction of the supercontinents Rodinia and Gondwana. Remnants of the formation and disintegration of these former land masses can be found, although great uncertainties remain in the location of tectonic boundaries beneath the ice sheet of Antarctica due to general lack of outcrops and the limited amount of geological data. Space and airborne measurements are the only possibility to obtain comprehensive spatial data coverage of geophysical data over the extensive large polar areas.

Common knowledge of the geological framework displays three major tectonic events which formed Dronning Maud Land (DML): the Grenvillian Orogen (1.1 Ga) build up Rodinia, the Pan-African-Antarctic Orogen (EAAO, 500 Ma) rose in the supercontinent Gondwana and finally the breakup of Gondwanaland, at around 180 Ma.

During this work, as part of the VISA project (Validation, densification and interpretation of satellite data for the determination of magnetic field, gravity field, ice mass balance and structure of the Earth crust in Antarctica using airborne and terrestrial measurements), four years of investigated airborne based data (2001-2005) are processed, compiled and interpreted. The methods of measurements are explained in the methodology chapter, focused on the complex computational and time-consuming processing, to handle topographic-, magnetic-, and gravity data.

Finally, the thesis displays a compilation of a homogeneous database for the DML region from 14° W to 20° E and from 70° S to 78.5° S. Furthermore, comprehensive studies and techniques, such as wavelength-filtering, depth estimation routines, isostatic analysis and Curvature discussions, are applied for final geological interpretation.

The presented maps display detailed boundaries of geologic and tectonic structures, which already have been suggested or discussed in recent literature, but have never been known to full extent, concerning detail, locations, boundaries and structures. With respect to earlier conducted geophysical investigations in DML, up to 85% of the gravity data and 65% of the magnetic data, presented in this thesis, cover unexplored regions and contribute therefore a large amount of new data to the Antarctic geological research.

Old lithospheric boundaries between the Archaen Craton, the Grunehogna Province, and a Proterozoic to Early Paleozoic mobile belt, the Maudheim Province, were be interpreted on the basis of the new database and the use of isostatic and curvature analysis. Detailed mapping of thrust faults show the strike of major tectonic events. All of these observations constitute an integrated geological model, which is confirmed by recent seismologic-, seismic,- and geologic results.

Contents

Chapter 1

INTRODUCTION

1.1 Antarctica

The Antarctic continent plays a keyrole in the development and study of plate tectonics. The study of the lithosphere and identification of lateral discontinuities in Antarctica and the surrounding areas are essential to an understanding of the geodynamic evolution of the continent.

Airborne acquisition of potential field and other remote-sensed data is essential due to the extensive ice cover of the Antarctic continent. This large ice sheet hinders direct observations of the surface geology.

Potential field anomaly maps are particularly helpful in connection with geological mapping of the sparse outcrop, enabling the detection of major structures and interpretation of the composition of Antarctica. Magnetic and gravity data provide regional maps of the structural grain in the basement, suture zones between basement terranes, the basement terranes themselves, and the nature of intra continental rifts and the extent of major faults.

The relative timing and kinematics of the evolution of the Antarctic continent can be derived from the detailed geophysical mapping of rock units. Distinctive magnetic signatures provide important markers for extracting both the orientation of regional faulting, and its relative timing.

Information on the isostatic state of the lithosphere is contained in long wavelength anomalies, providing significant insights into the thermal structure of the Antarctic lithosphere.

From reconstructions of Gondwana, it should be possible to identify the shapes of old oceans and therefore to infer the pathways of currents, that would have played a role in past climates.

Thus, receiving information on the crustal makeup of this remote and poorly understood region is essential. Furthermore, such projects will provided improved global potential field modelling and assist with the verification and calibration of observations obtained from polar orbiting satellite missions.

A significant amount of airborne data have been collected during the past 40 years and have contributed toward a better understanding of regional tectonic provinces within Antarctica. For example the Russian regional aeromagnetic surveys undertaken by VNIIOkaengeologia in the 80s have imaged magnetic pattern and tectonics from the Weddell Sea to the boundary of Dronning Maud Land (DML). More high detailed investigations, but much smaller in extent were flown by British Antarctic Survey (BAS) in the Jutulstraumen region and by the Bundesanstalt für Geowissenschaften und Rohstoffe (BGR) in the Schirmacher oasis and adjacent areas.

Previous investigations by the Alfred Wegener Institute (AWI) within the EMAGE project were focused on the break-up history of Gondwana and the opening of the Weddel Sea. The interpretation of this extensive magnetic anomaly dataset in the eastern Weddell Sea constrained the ages and orientations of sea floor spreading anomalies and were used to calculate a new set of model parameters for the opening of the Weddell Sea. These parameters were combined with constraints on the South America-Africa and Africa-Antarctica spreading systems, based on a compilation of magnetic anomaly and fracture zone data, to determine a new model for Gondwana break-up between 176Ma and 83Ma (König, 2005).

Within the new VISA project, as described in the following chapters, the efforts were made to conduct purely continental investigations, including systematic airborne coverage over an area of more than 1.2 Million km^2, from 2001 to 2005.

1.2 The VISA project

The VISA project **(Validation, densification and Interpretation of Satellite data for the determination of magnetic field, gravity field, ice mass balance and structure of the Earth crust in Antarctica using airborne and terrestrial measurements)** is an interdisciplinary project undertaken in collaboration between the Technical University Dresden (TUD) and the Alfred Wegener Institute for Polar- and Marine Research, Bremerhaven (AWI).

The primary goal of this long-term project is to estimate the mass balance of Antarctica's continental ice sheet based on temporal changes of the gravity field of the Earth. All processes which result in a growth or shrinkage of an ice sheet also cause temporal changes of the gravity field, as, for instance, mass is redistributed between the ice sheets and the world's oceans. Such temporal variations of the global mass distribution should be determined by new satellites with mission periods of up to 5 years measuring the Earth's gravity field. A very precise identification and quantification of all signals influencing the gravity field is necessary in order to determine mass induced effects and thus minimize errors in the calculation of the mass balance of the ice sheet.

Apart from these, there is a huge need to understand the subglacial geology, of which observations are impossible due to the ice cover.

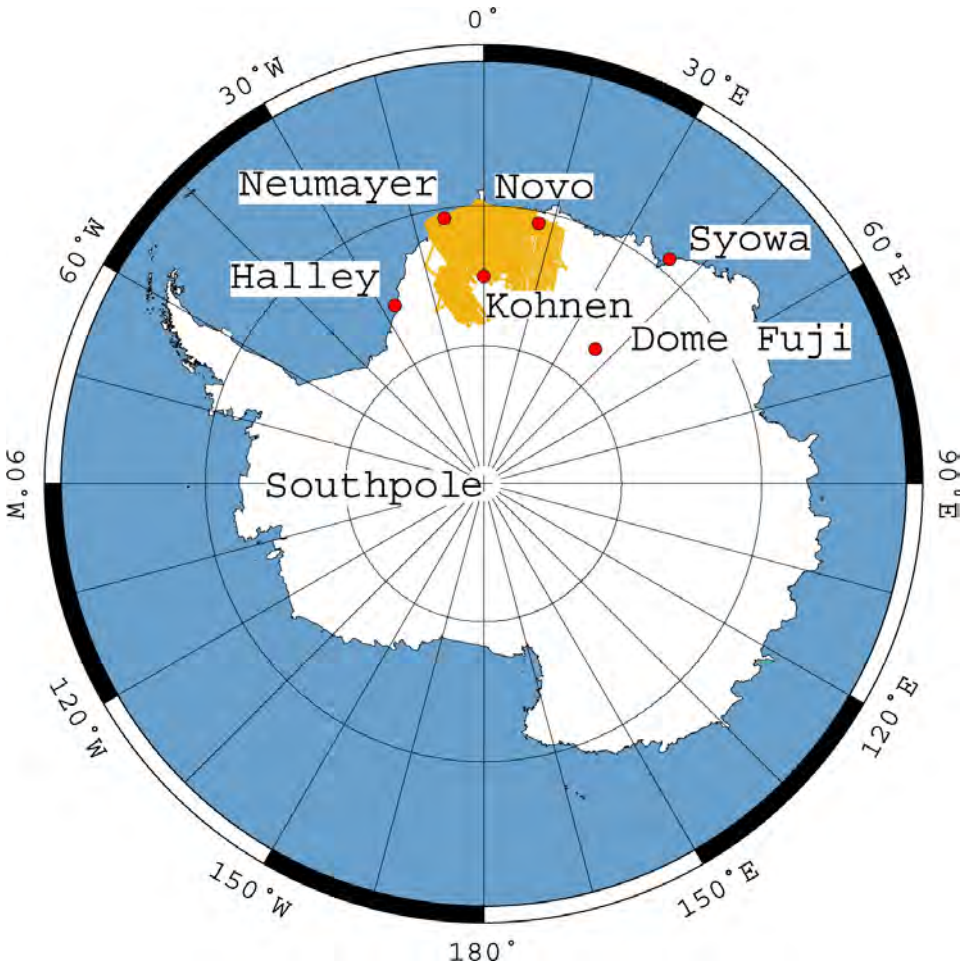

Figure 1.1: The Antarctic continent and the related area of investigation within the VISA project.

Finally, other complementary indirect methods are utilized in this multidisciplinary project, and are listed as follows:

- Validation and densification of gravity satellite mission data (CHAMP, GRACE and GOCE) in Antarctica, using airborne gravity.
- Detailed investigations on ice, including height, gravity and mass changes including glaciological and geodetic field campaigns.
- Investigations of vertical motions due to lithospheric processes, using geodetic determinations of height and gravity changes on bedrock, estimation of seismicity, and determination of focal mechanisms.
- Detailed investigations into the structures of the gravity field, magnetic field, ice thicknesses, surface and bedrock topography, from airborne measurements.

This thesis deals mainly with the processing and interpretation of airborne data, in detail: The evolution of the South Atlantic region, including the Weddell Sea and its adjacent areas, is of crucial importance for understanding the processes responsible for the structure and tectonics of the Antarctic lithosphere and its relation to geodynamic processes, especially to the timing and geometry of the initial stages of the Mesozoic break-up between Africa, Antarctica and South America. The sub-glacial geology is of utmost importance for unraveling the geological evolution of Antarctica prior to the break-up of Gondwana. Understanding the sub-ice geology allows reconstruction of ancient mountain chains (collision zones) across continents, which are separated by large ocean basins in the present world.

Since only the peaks of the Dronning Maud Land mountains can be geologically sampled, geophysical methods are required to uncover the geological structure beneath the ice. Therefore, extensive airborne surveys were conducted across DML between 2001 and 2005 to close data gaps and to improve existing data sets.
The compilation of previous regional Russian investigations (magnetic and gravity) gave a first impression on the sub-glacial geology in the Weddel Sea and adjacent areas (Aleshkova et al., 2000; Golynsky et al., 2000), but the data are of insufficient accuracy for direct comparisons with satellite missions. In addition, the variable spacing of flight lines will cause in problems with their interpretation.

The extent of the new survey areas from 14°W to 20°E and from 70°S to 78.5°S, is large enough to fully recognize long wavelength regional anomalies. However, smaller features could also be mapped, owing to an average line spacing of about 10 km.
In detail, the new compilation of airborne magnetic and gravity data across DML is focused on:

East Antarctic Craton / Maud boundary: The Grunehogna Craton is only sparsely exposed at a small number of nunataks. Detailed airborne-geophysical investigations will define the Cratonic units exactly, as well as their regional extension. The continent-ocean boundary is of utmost interest.

Grenvillian mountain chains: The southern extension of the Grunehogna Craton is the Maudheim Province, which has an Grenvillian age of 1.1 Ga. The mutual boundary is marked by strong magnetic anomalies and may correlate with structures in Southern Africa. The exact boundary of the Grunehogna Unit (GU) is not well developed.

Pan African overprinted crust: The Heimefrontfjella, Kirnvanveggen and Sverdrupfjella ridges mark the boundary of the influence of the East Antarctic African Orogen (EAAO, 500 Ma), which is the result of the collision of East and West Gondwana. The existing, limited, datasets permits no detailed interpretation.

1.3 Previous geological investigations

In the distant past, Earth was a very different planet than the one we know today. If you could travel through time to arrive at the Earth of a billion years ago, you would have a hard time navigating. A strange giant continent and a single planetary ocean would replace the familiar continents and oceans of todays world. [1]

1.3.1 Supercontinent Cycle

During the Neoproterozoic, a supercontinent, referred as Rodinia, formed at ca. 1100 Ma and broke apart at around 800-700 Ma. Rodinia is thought to have included Laurentia, Australia, Antarctica, Greater India and Amazonia, but their exact relative positions and the timing on break-up are the subject of ongoing debate in a number of papers dealing with palaeomagnetic and geological data. Grenvillian/Kibaran aged deformation is exposed along margins of Laurentia, East Gondwana, Amazonia and Baltica. Geologic records indicate that Neoproterozoic and early Paleozoic rift margins surrounded Laurentia, while similar-aged collisional belts crosscut Gondwana. Hence, the breakup of one supercontinent was followed rapidly by the assembly of another, smaller, one: Gondwana.

1.3.2 Gondwana assembly and breakup

The reorganization of cratonic blocks following by the Neoproterozoic breakup of Rodinia gave birth to Gondwana. This reassembly of various continental fragments into a new supercontinent started between 800-700 Ma and continued up to 500 Ma, with the occurrence of collisional tectonics along orogenic belts (Pan-African/Brasiliano). Traditionally, Gondwana can divided into three separate blocks. West Gondwana, consisted of the Amazonia Craton of South America and the West African Craton. Central Gondwana comprised the Congo and Kalahari cratons of Africa and the Grunehogna Province of East Antarctica. While East Gondwana includes eastern Madagascar, India, Sri Lanka, the East Antarctic shield and Australia.

1.3.3 Connection between Antarctica and South Eastern Africa

Geological correlations suggest that the crustal evolution of DML and SE Africa were quite similar from Archea until Mesozoic times. The assembly of DML took place before 1000 Ma as both the Grunehogna and Maudheim provinces are transected by orogenic belts. The lithostratigraphic, metamorphism and deformation of the late Archean to Mesoproterozoic granite-greenstone rocks and the volcanic-sedimentary sequences of the Kaapval-Zimbabwe cratonic provinces are closely comparable to those of the Grunehogna Province. Western DML consists of numerous Precambrian elements, together referred to as the Grunehogna Craton, a fragment of the Kalahari-Kaapval-Craton (KKC). These cratons parted during Gondwana breakup (Jurassic

[1] Burke Museum of Natural History and Culture, University of Washington

times). Correlation with the KKC is on the bases of Archean and Mesoproterozoic sediments with similar age.

The rocks of southern DML are grouped together as the Maudheim Province (MP), which consists of high grade metamorphic rocks of Grenvillian age. The MP can be seen as an eastward continuation of the Namaqua-Natal-belt in South Africa. Limited outcrops exist and are confined to the nunataks at Sverdrupfjella, Kirvanveggen and Heimefrontfjella.

The Heimefrontfjella (HF), a 140 km SW to NE oriented mountain range, is divided into several blocks (Trottanfjella, Sivorgfjella, XU-Fjella and the Kottas-Mountain). The range divides the EAAO into a western and an eastern, more overprinted part (Jacobs, 1996). A prominent shear zone is recognized within the HF.

Central DML was strongly influenced during the assembly of Gondwana. The crystalline basement melted and the Grenvillian structures of the EAAO were covered. An element of crustal extension is recognized within the continent-continent collision settings, and has been suggested as possible related to the replacement of the orogenic root during delamination. Elsewhere, such processes are known to have caused topographic uplift and subsequent orogenic collapse.

The youngest tectonic event in DML occurred during Jurassic times, the break-up of Gondwana. A volcanic rifted continent margin formed and the Weddell Sea and Lazarev Sea were established by rifting processes. Permo-triassic shear zones where reactivated and forced strike-slip movements between Africa and Antarctica (Cox, 1992).

1.3.4 The EAAO

Due to the strong influence of the East African Antarctic Orogen (EAAO) on the geological history of DML, some detailed notes are needed to help in understanding the complexity.

The EAAO is one of the largest orogenic belts on the planet. It resulted from the collision of various parts of proto–East and West Gondwana during late Neoproterozoic to early Paleozoic times (between 650 and 500 Ma). The orogen extents for over nearly 8000 km, from Arabia in the north (Arabian–Nubian shield) along the East African margin (Mozambique belt) into East Antarctica (e.g., Muhongo and Lenoir, 1994; Stern, 1994; Jacobs and Thomas, 2002). In most places along its length, the orogen is more then 1000 km wide (see figure 1.2, left).

The southern part of the EAAO reaches from Kenya to East Antarctica. In East Antarctica, rocks of late Neoproterozoic-early Paleozoic age are exposed between western Dronning Maud Land and the Lützow-Holm Bay area. Although only exposed in nunataks, the dominant orogenic structures can be traced under the ice by aeromagnetic anomalies (e.g., Golynsky and Jacobs, 2001). The core of this part of the orogen is exposed in central and eastern Dronning Maud Land (e.g., Jacobs et al., 1998, 2003; Shiraishi et al., 1994), see figure 1.2, right.

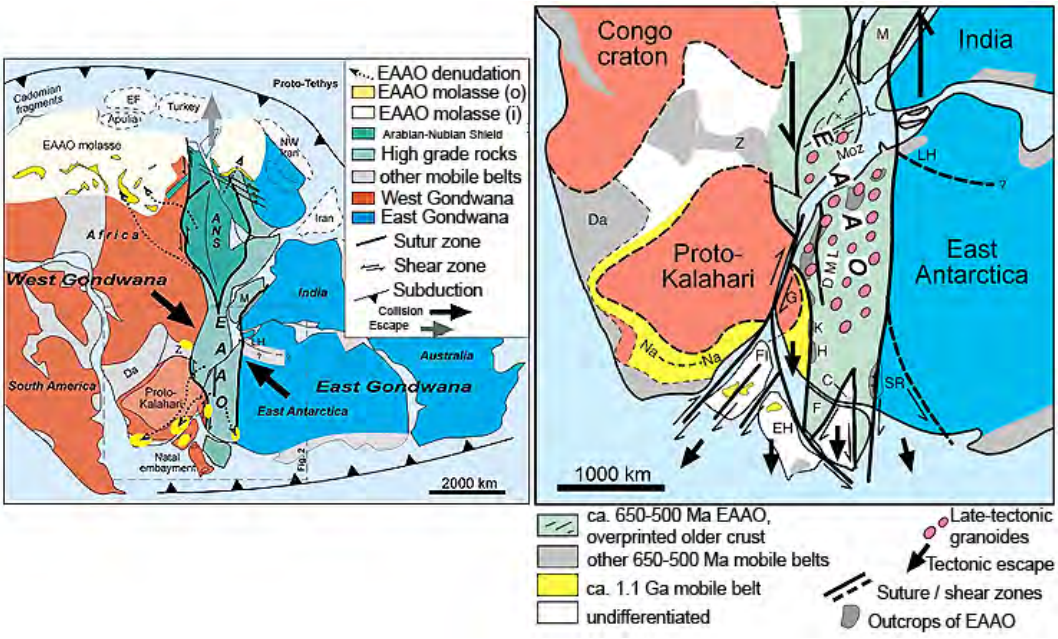

Figure 1.2: The East African Antarctic Orogen and escape tectonics in DML. *left:* The East African Antarctic Orogen (EAAO) is interpreted as the main collisional orogen along which parts of proto-East and West Gondwana collided to form Gondwana. *right:* Escape tectonics model for the southern termination of the EAAO. *Abbreviations:* ANS-Arabian-Nubian shield; C-Coats Land; Da-Damara belt; DML-Dronning Maud Land; EF-European fragments; EH-Ellsworth-Haag; F-Filchner block; FI-Falkland Islands; G-Grunehogna; H-Heimefrontfjella; K-Kirvanveggen; LH-Lützow-Holm Bay; M-Madagascar; Na–Na-Namaqua-Natal; SR-Shackleton Range; Z-Zambesi belt, (after Jacobs, 2004).

Large volumes of high-temperature post tectonic granitoids occur in central Dronning Maud Land (>50 percent outcrop area). Their petrology and geochemistry indicate that they are crustal derivatives, probably the consequence of asthenospheric upwelling following delamination of the orogenic root, and subsequent orogenic collapse (Jacobs et al., 2003).

In western Dronning Maud Land the 20 km-wide Heimefront transpression zone (Jacobs and Thomas, 2002) separates Mesoproterozoic rocks with a strong Pan-African tectonothermal overprint to the east from unaffected rocks to the west. Consequently, this shear zone has been interpreted as the western front of the orogen (Golynsky and Jacobs, 2001). Further evidence that the Heimefront transpression zone is a major crustal discontinuity is provided by geophysical data, which show that the high-amplitude, elongate magnetic anomalies that characterize the eastern half of the ca. 1.1 Ga Namaqua-Natal-Maud belt (southeast Africa and East Antarctica juxtaposed in Gondwana) terminate sharply against it.

The Pan-African collision history of the southern part of the orogen in Antarctica and Mozambique can be separated into three major phases:

- An earliest stage, recorded in the Schirmacher Oasis at ca. 620 Ma (Henjes-Kunst, 2004), followed by anorthosite magmatism in the main mountain range of DML at ca. 600 Ma.
- The main deformation and medium- to high-grade metamorphism in the main mountain range of DML and the Nampula Province of Northern Mozambique is bracketed in age by metamorphic zircon rims to between ca. 590 and 550 Ma and is interpreted to represent the collision phase (Jacobs et al., 2003).
- A late Pan-African stage is associated with extension, tectonic exhumation and south-directed extrusion between ca. 530 and 500 Ma, exposing mid- to lower crustal levels (e.g. Jacobs and Thomas, 2004). This period is accompanied by syn-tectonic and late- to post-tectonic intrusions. The volume of igneous rocks seems to drastically increase toward the end of the extensional period, culminating in voluminous and extensive granitoid-charnockoid magmatism. Late to post-tectonic granitoids with dominantly charnockitic mineralogy cover an area of at least 15000 km^2 in East Antarctica (where they can be traced under the ice by geophysical means) and NE Mozambique, see figure 1.2.

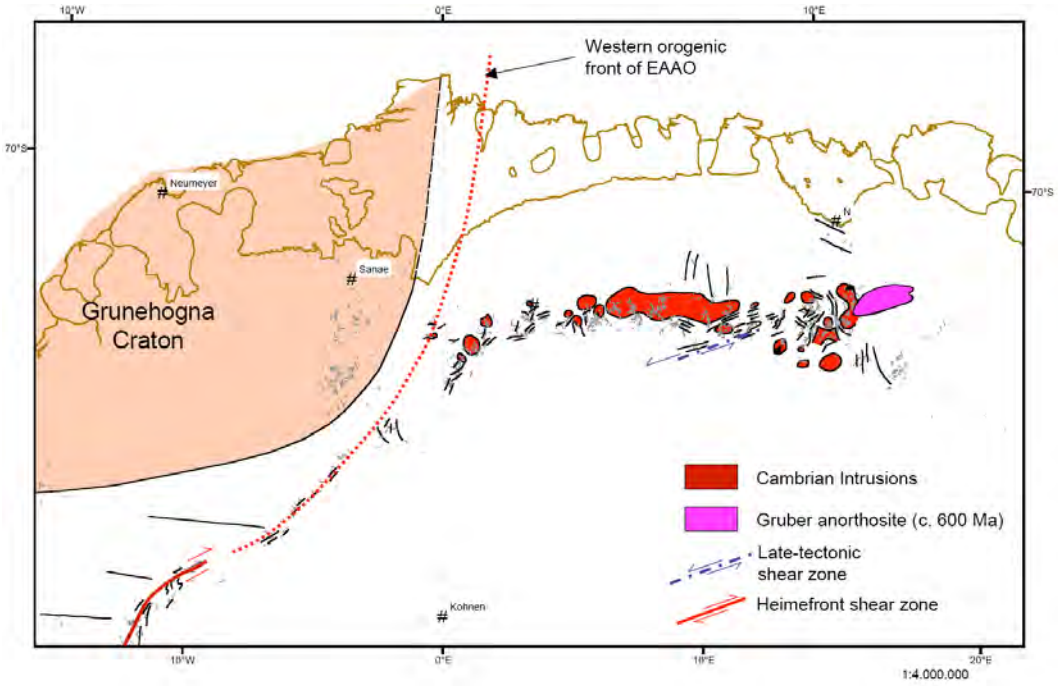

Figure 1.3: Detailed geological sample work, including mapped intrusions and shear zones, after Jacobs [pers. comm.].

Summarizing this, a widespread late-to post-tectonic Cambrian (Pan-African) magmatic province is recognized in the southern part of the East African-Antarctic Orogen in NE Mozambique and Central Dronning Maud Land, two areas that were thought to be contiguous within Gondwana. It covers an area of at least 15000 km^2, and would have stretched from the northern margin of the Nampula Province (the Lurio Belt) in Mozambique, through to central Dronning Maud Land, decreasing gradually westwards in volume to the eastern Sverdrupfjella, where the magmatism stops, close to the frontal zone of the orogen in that region. New SHRIMP dates from Dronning Maud Land reveal that the intrusion of the granitoids is tightly constrained to almost exactly 500 Ma, preceded and/or accompanied by extensional shearing dated at c. 510 Ma. The intrusions are interpreted to have crystallized at mid-crustal levels after collapse and extension of the orogen, possibly accompanied by delamination of the lithosphere root. Hot asthenosphere, rising to the lower crust above the subsiding orogenic root would have provided the heat source for the magmatism which is typically anhydrous, high temperature and charnockitic (Jacobs, 2007).

Chapter 2

METHODOLOGY

2.1 Aircraft handling and design

[1]The Alfred Wegener Institute for Polar and Marine Research, Bremerhaven (AWI), owns the aircraft POLAR2 (D-CAWI) and POLAR4 (D-CICE). The planes are platforms for geophysical, meteorological, air chemistry and remote sensing research. They provide logistical support for expeditions. Aircraft management is presently commissioned to The Deutsche Forschungsanstalt für Luft- und Raumfahrt (DLR, German Aerospace Research Establishment) by the Alfred Wegener Institute. The DLR subcontracted OPTIMARE, Sensorsysteme AG, for the operational use of the aircraft. OPTIMARE is responsible for the scientific instrumentation and data acquisition.

Figure 2.1: Polar 2 aircraft, operated by AWI, during field activities.

Airborne Polar missions need long-term planning, a task which is performed by the Aircraft Planning Group of the Alfred Wegener Institute. It prepares an aircraft operation plan based on applications from the research group. The plan is presented to the User Advisory Council, consisting of scientists from German research institutions and universities. The board advises the director of the Alfred Wegener Institute on

[1]taken from users handbook for the POLAR 2 and POLAR 4 research aircraft

the missions of the aircraft. The membership covers different disciplines interested in aircraft based research in polar regions.

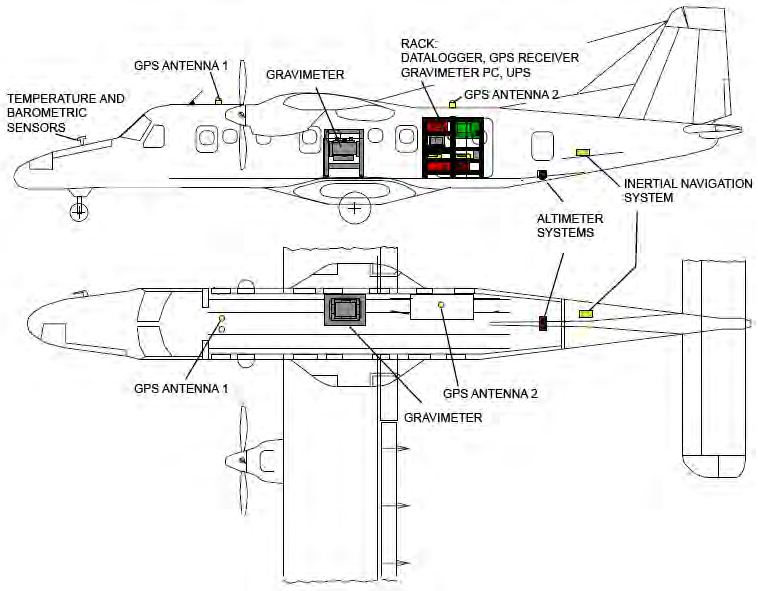

Figure 2.2: Cross-section of Dornier 228-200 Polar 2 aircraft showing the geophysical configuration on board, adopted from Boebel (2000).

Figure 2.2 displays the aircraft used, Polar 2 or Polar 4, with the geophysical configuration on board, which is used within the VISA project. The combined system consists of:

- two GPS-Trimble 4000ssi receivers for the estimation of the flightpath trajectory; inclusive geodetic GPS antenna onboard the aircraft roof
- one Honeywell LaserNav II inertial navigation system for estimation of the aircraft orientation; aircraft rear-end
- one ADMB OPTECH- or Riegl LD 90 Laseraltimeter for estimation of the altitude; roller door
- one ZLS Ultrasys gravity meter based on a LaCoste&Romberg AirSea S56 gravimeter for the acquisition of scalar gravity; near aircraft balance point
- two Geometrics CS-2 magnetometer measuring the total magnetic field; wing tips
- one tri-axial Bellington fluxgate magnetometer, measures three components of the magnetic field with respect to the movement of the plane for compensation purposes; in the tail of the aircraft
- one 150 MHz Radio Echo Sounding system to map ice thicknesses and internal layering of glaciers using Short Backfire Antenna; below each wing

Apart from these sensors, a data acquisition system were installed and mounted in a rack to store the acquired data in a common database.

2.2 Radio Echo Sounding System

The Radio Echo Sounding System is used to map ice thicknesses and the internal layering of glaciers, ice sheets and ice shelf areas. Installed on board the aircraft, it is capable of penetrating ice thicknesses of up to 4 km. It uses radio pulses transmitted downwards into the ice that are partly reflected at layers with contrasting electrical properties, as well as by the boundary between ice and sea water.

The system was designed and built in cooperation between AWI, TUHH (Technische Hochschule Hamburg-Harburg, Institut für Hochfrequenztechnik), and Aerodata Flugmesstechnik GmbH, Braunschweig.

The system uses two antennae of the short backfire type mounted underneath the wings, see figure 2.1. A burst of 150 MHz with a duration of 60 ns or 600 ns is transmitted by the left-wing antenna and the reflected signal are received by the right-wing antenna. The amplified and filtered signal is sent into a logarithmic detector which produces a low frequency envelope signal from the bursts. This output signal is passed onto the data acquisition system for printout and storage. The transmitter and the preamplifier are mounted in the wings in order to reduce noise and cable ringing.

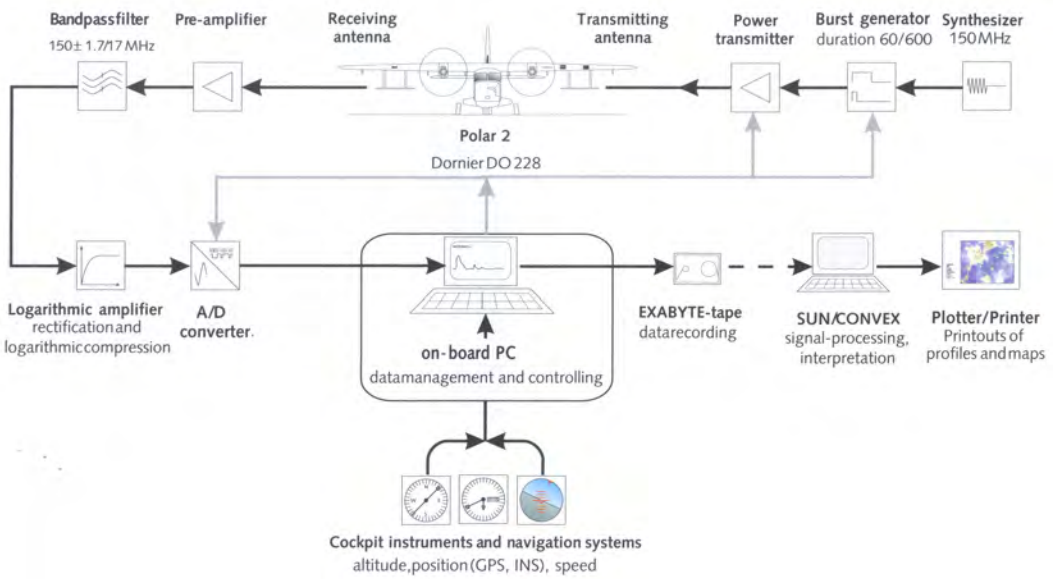

Figure 2.3: Polar 2 Radio Echo Sounding instrumentation and principles, adopted from Steinhage (2001).

A compression (stacking) of the signal is calculated, with the well calculated loss of phase information. The advantage of this is faster processing of the data set, with signal repetition frequency of 20 Hz; 1000 pulses are consecutively digitized and stacked. At a speed over the ground of 130 knots (240 kmh^{-1}), the horizontal resolution is 3.25 m. The vertical resolution depends on the pulse-length setting, the duration and the shape of the pulse, and the physical properties of the ice. Theoretically, a pulse of 60 ns provides a resolution of 5 m, a pulse of 600 ns about 50 m. By using the RES-system in toggle mode (after each registration the pulse changes between 600 ns and 60 ns) it is possible to arrive a signal that combines the highest vertical resolution and maximum power (penetration depth). A corollary is the loss of horizontal resolution by a factor of 2 (3.25 m with a single pulse to 6.5 m in toggle mode), but this is compensated for by the increased vertical information content.

The received signals are converted into digital format at a rate of 75 MHz and 24 bit resolution. This data stream is stored in a database and post-processed to SEGY-format. The hard disks can hold up 7.5 hours of airborne ice radar survey. The RES system can be entirely computer supervised except for setting the transmitting frequency (between 100 and 200 MHz) and the signal filter.

When a wave encounters an interface between materials of different properties, the wave may be refracted, reflected, or both. Snell's Law describes the reaction of light to a boundary between materials of different dielectric contrasts (or refractive index), based on the angle at which a ray (perpendicular to the wave front) hits the interface. The angle of the incoming ray (Angle of Incidence α_i) is equal to the Angle of Reflection α_r. The Angle of Refraction α_R is determined by the ratio of the sines of the Angle of Incidence to the Angle of Refraction and the ratio of the dielectric constants for the upper and lower layers (ϵ_1 and ϵ_2).
There is a point where the Angle of Incidence is large enough, close to horizontal, that there is no refraction. This is called the Angle of Critical Refraction where all the incoming waves are either reflected or refracted along the interface. Any angles larger than the Angle of Critical Refraction result in only reflection.

The receiver records the amount of time between the arrival of the transmitted wave and any reflected waves as well as the strength of the waves. The radio waves travel at different speeds through different materials. For example, the velocities of radio waves are known with 3 x 10^8 ms^{-1} through air and a little less than half as much in ice at 1.69 x 10^8 ms^{-1}. Where a glacier bed echo is recorded, the time delay is used to calculate the ice thickness.

An example of a 500 km length RES profile (cross section over Jutulstraumen) is shown in figure 2.4. This profile is measured with the 60 ns pulse, is 50 times stacked, and has been band-pass filtered, amplitude scaled and corrected to a constant flight level.

Dark gray represents the travel path through air. The first reflection represents the surface-topography shown with the dark black line. A strong surface multiple reflection (result of reverberation within the ice) is clearly seen as is the internal layering of the ice sheet. The subglacial topography is marked as second main reflection horizon. The loss of signal is clearly recognized over locations with strong gradients in surface topography.

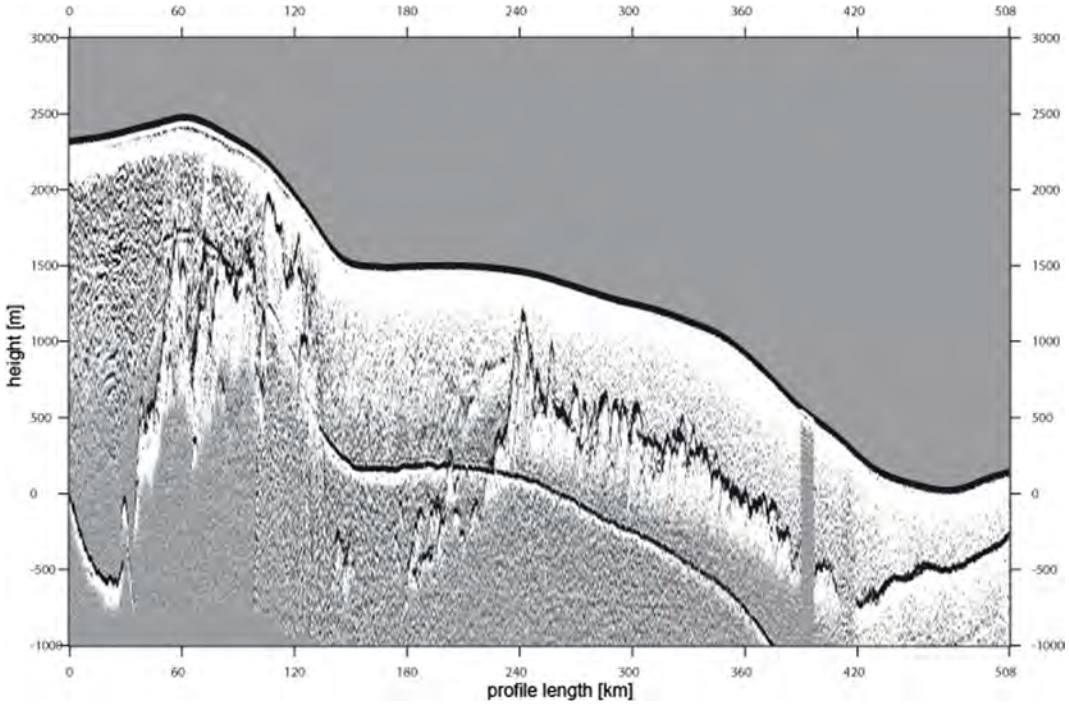

Figure 2.4: Cross section of RES sounding profile. Data are measured with 60 ns pulse, 50 times stacked, band-pass filtered, amplitude scaled and corrected to a constant flight level [Steinhage (pers. comm.)].

2.3 GPS System

Precise navigation of the aircraft is of utmost importance for the later interpretation of scientific data. In particular the gravity field measurements, are sensitive to positioning accuracy and accelerations. Due to this, it is necessary to understand GPS techniques more then just a basic tool.[2]

The Global Positioning System (GPS) is a network of 24 Navstar satellites orbiting Earth at 21000 km, originally established by the U.S. Department of Defense (DOD). GPS provides specially-coded satellite signals that can be stored or processed in a GPS receiver, enabling the receiver to compute position, velocity and time. Using the stored data to enable post-processing options yields advantages from having more precise algorithms and additional information.

For normal code processing, the signals of four GPS satellite have to be used to compute positions in three dimensions and the time offset in the receiver clock. Higher accuracy can be archived with phase observations of the GPS signal. Here, an additional unknown variable has to be determined, so that a minimum of five GPS satellite observations is needed. The Global Positioning System is comprised of three segments: satellite constellation, ground control/monitoring network and user receiving equipment.

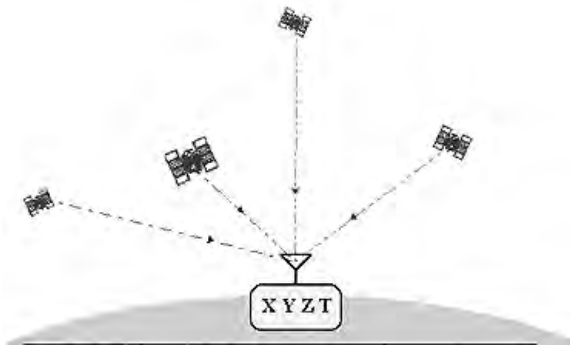

Figure 2.5: The Global Positioning System; Measurements of code-phase arrival times to estimate position and time (after Dana, P.H.).

The formal GPS Joint Program Office (JPO) programmatic terms for these components are the space, operational control and user equipment segments, respectively.

2.3.1 Satellite Constellation

The satellite constellation comprises satellites in the orbit that provide the ranging signals and data messages to the user equipment. A GPS satellite transmits two microwave carrier signals. The L_1 frequency (1575.42 MHz) carries the navigation message and the single point positioning code signals. The L_2 frequency (1227.60 MHz) is used to measure the ionospheric delay by pulse per second (PPS) generator equipped receivers. Three binary codes shift the L_1 and/or L_2 carrier phase.

[2]most illustrations and suggestions are taken from P. H. Dana, The Geographer's Craft Project, Department of Geography, The University of Colorado at Boulder,
$http://www.colorado.edu/geography/gcraft/notes/gps/gps_f.html$

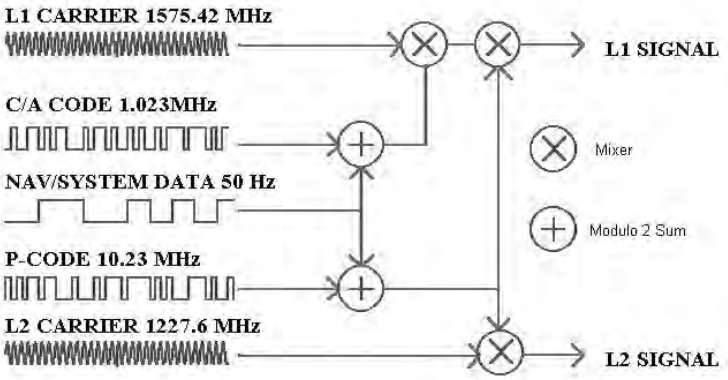

Figure 2.6: GPS satellite signals, adopted from Dana, P.H.

The C/A code (coarse acquisition) modulates the L_1 carrier phase. This C/A signal is a repeating 1 MHz pseudo random noise (PRN) code. This noise-like code modulates the L_1 carrier signal, "spreading" the spectrum over a 1 MHz bandwidth.
The C/A code repeats every 1023 bits (one millisecond). There is a different C/A code PRN for each satellite. Their PRN number, the unique identifier for each PRN code, often identifies GPS satellites. The C/A code that modulates the L_1 carrier is the basis for the civil single point positioning (SPS). The P-code (precise code) modulates both the L_1 and L_2 carrier phases. The P-Code is a very long (seven days) 10 MHz PRN code. In the anti-spoofing (AS) mode of operation, the P-code is encrypted into the Y-code. The encrypted Y-code requires a classified anti-spoofing module for each receiver channel and is for use only by authorized users with cryptographic keys. The P (Y)-Code is the basis for the PPS. The navigation message also modulates the L_1-C/A code signal. The navigation message is a 50 Hz signal consisting of data bits that describe the GPS satellite orbits, clock corrections, and other system parameters.

The nominal GPS operational constellation consists of 24 satellites that orbit the earth in 12 hours (see figure 2.7). There are often more than 24 operational satellites as new ones are launched to replace older satellites. The satellite orbits repeat almost the same ground track (as the earth turns beneath them) once each day. The orbit altitude is such that the satellites repeat the same track and configuration over any point approximately each 24 hours (4 minutes earlier each day). There are six orbital planes (with nominally four satellites in each), equally spaced (60 degrees apart), and inclined at about 55 degrees with respect to the equatorial plane. This constellation provides the user with between five and eight satellites visible from any point on the earth.

2.3.2 Control Segment

The Control Segment (OCS) has responsibility for maintaining the satellites and their proper functioning. This includes maintaining the satellites in their proper orbital positions (called station keeping) and monitoring satellite subsystem health and status. The OCS also monitors the satellite solar arrays, battery power levels, and propellant levels used for manoeuvres, and activates spare satellites. The overall structure of the operational ground/control segment is as follows: Remote monitor stations constantly track and gather C/A and P(Y) code from the satellites and transmit this data to the Master Control Station, which is located at Falcon Air Force Base, Colorado Springs. There is also the ground uplink antenna facility, which provides the means of commanding and controlling the satellites and uploading the navigation messages and other data. The unmanned ground monitor stations are located in Hawaii, Kwajalein in the Pacific Ocean, Diego Garcia in the Indian Ocean, Ascension Island in the Atlantic and Colorado Springs, United States. Ground antennas are also located in these areas. These locations have been selected to maximize satellite coverage.

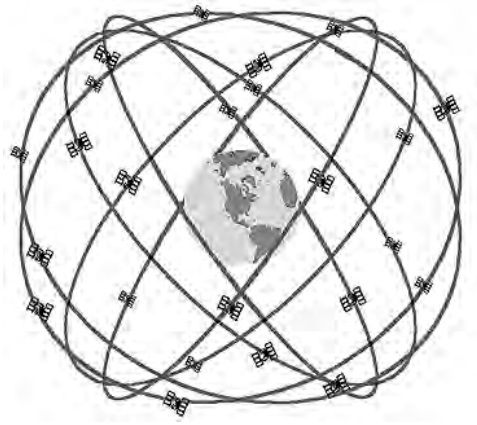

Figure 2.7: GPS nominal constellation: 24 satellites in 6 orbital planes, 4 satellites in each plane, 20.200 km altitudes, 55 degree inclination, after Dana, P.H..

2.3.3 User Segment

The GPS user segment consists of the GPS receivers and the user community. As mentioned before, four satellites are required to compute the four dimensions of x, y, z (position) and time. GPS receivers are used for navigation, positioning, time dissemination, and other purposes. Navigation in three dimensions is the primary function of GPS.
Carrier-phase tracking of GPS signals has resulted in a revolution in land surveying. A line of sight along the ground is no longer necessary for precise positioning. This use of GPS requires specially equipped carrier tracking receivers. The L_1 and/or L_2 carrier signals are used in carrier phase surveying. L_1 carrier cycles have a wavelength

of 19.029 cm, while L_2 has 24.421 cm. If tracked and measured, these carrier signals can provide ranging measurements with relative accuracies of millimeters under special circumstances. Tracking carrier phase signals provides no time of transmission information. The carrier signals, while modulated with time tagged binary codes, carry no time-tags that distinguish one cycle from another. Therefore, to archive the range between satellites and receivers, the ambiguity of phases has to be solved.

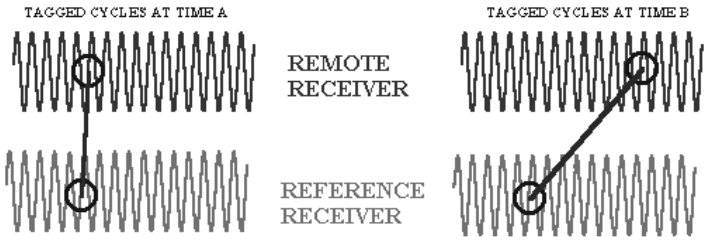

Figure 2.8: Carrier phase tracking: range from SV to remote has changed by 7 cycles if no cycle slips have occurred, after Dana, P.H..

The measurements used in carrier-phase tracking are differences in carrier-phase cycles and fractions of cycles over time. At least two receivers track carrier signals at the same time. Ionospheric delay differences at the two receivers must be small enough to insure that carrier phase cycles are properly accounted for. This usually requires that the two receivers are within about 30 km of each other. Carrier phase is tracked at both receivers and the changes in tracked phase are recorded over time in both receivers.

All carrier-phase tracking is differential, requiring both a reference and remote receiver tracking carrier phases at the same time, see figures 2.8 and 2.9. Unless the reference and remote receivers use L_1-L_2 differences to measure the ionospheric delay, they must be close enough to ensure that the ionospheric delay difference is less than a carrier wavelength. Using $L_1 - L_2$ ionospheric measurements and long measurement averaging periods, relative positions of fixed sites can be determined over baselines of hundreds of kilometers. Phase difference changes in the two receivers are reduced using software to differences in three position dimensions between the reference station and the remote receiver. High-accuracy range difference measurements with sub-centimeter accuracy are possible. Problems result from the difficulty of tracking carrier signals in noise or while the receiver moves.

Two receivers and one satellite over time result in single differences. Two receivers and two satellites over time provide double differences. Post-processed static carrier-phase surveying can provide 1-5 cm relative positioning within 30 km of the reference receiver given a measurement time of 15 minutes for short baselines (10 km), or one hour for long baselines (larger than 30 km). Rapid static or fast static surveying can provide 4-10 cm accuracies with 1-kilometer baselines and 15 minutes of recording time. Real time kinematic (RTK) surveying techniques can provide centimeter measurements in real time over 10 km baselines tracking five or more satellites and real time radio links between the reference and remote receivers.

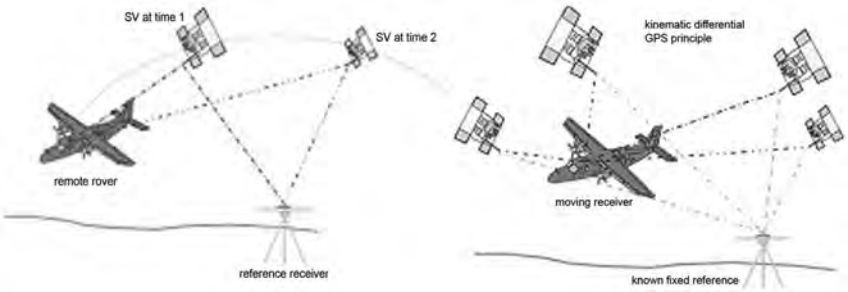

Figure 2.9: Carrier phase positioning, adopted from Meyer, U..

2.3.4 GPS Errors

GPS errors are a combination of noise, bias and blunders. Noise errors are the combined effect of PRN code noise (around 1 meter) and noise within the receiver (around 1 meter). The potential accuracy of the C/A code, of around 100 meters, is reduced to 30 meters (two standard deviations). A is the intentional degradation of the SPS signals by a time varying bias. The SA bias on each satellite signal is different, and so the resulting position solution is a function of the combined SA bias from each satellite vehicle used in the navigation solution. Because SA is a changing bias with low frequency terms in excess of a few hours, position solutions or individual SV pseudo-ranges cannot be effectively averaged over periods shorter than a few hours. Differential corrections must be updated at a rate less than the correlation time of SA (and other bias errors).

SV clock errors uncorrected by the Control Segment can result in one-meter errors. Ephemeris data errors are about 1 meter, tropospheric delay errors around 1 meter. The troposphere is the lower part of the atmosphere from ground level up to around 8 to 13 km, that experiences the changes in temperature, pressure, and humidity associated with weather changes. These effects are independent for both frequencies, and so cannot be eliminated by L_1/L_2 processing. Models of tropospheric delay are complex and require estimates or measurements of these parameters. Un-modeled tropospheric delay errors are in the range of 10 meters. The ionosphere is the layer of the atmosphere from 50 to 500 km that consists of ionized air. The transmitted model can only remove about half of the possible 70 ns of delay leaving a ten meter un-modeled residual. The ionospheric delay can indeed be calculated by L_1/L_2 observations, but for low satellite constellation, the error increases.

Multi-path errors are about 0.5 meters. Multi-path is caused by reflected signals from surfaces near the receiver that can either interfere with, or be mistaken for, the signal that follows the straight-line path from the satellite. Multi-path is difficult to detect and sometimes hard to avoid.

Table 2.1: Precise error model, C/A code. This is the statistical ranging error (one-sigma) that represents the total of all contributing sources. The dominant error is usually that arising from the ionosphere.

	one-sigma error in meter			
error sources	bias	random	total	DGPS
Ephemeris data	2.1	0.0	2.1	0.0
Satellite clock	2.0	0.7	2.1	0.0
Ionosphere	1.0	0.5	1.2	0.1
Troposphere	0.5	0.5	0.7	0.1
Multipath	1.0	1.0	1.4	1.4
Receiver measurement	0.5	0.2	0.5	0.5
User equivalent range error (UERE), rms	3.3	1.5	3.6	1.5
filtered (UERE), rms	3.3	0.4	3.3	1.4

2.3.5 GPS Processing

As shown before, each satellite transmits signals on two sinusoidal carrier waves, L_1 and L_2. Modulated onto L_1 are two pseudo random noise codes, in RINEX (receiver independent exchange format) notation called C_1 and P_1. A second P-code, P_2, is modulated onto the L_2 frequency. Assuming the clocks in the satellite and in the receiver are synchronized, the travel time signal can be determined by measuring the shift between the internal and the incoming versions of the code in the receiver. The pseudo random noise codes are designed to have a low autocorrelation, allowing the shift to be measured precisely and without ambiguity. Multiplication of the transmission time by the speed of light gives the range between the satellite and the receiver. However, in practice the time synchronizations between receivers and satellites are not perfect. Because of this effect and the influence of other error sources these ranges are called pseudo-ranges. It is possible to measure the carrier beat phase more precisely than the codes themselves, however integer ambiguities must be resolved for centimeter and better positioning.

2.3.5.1 DGPS Processing

The idea behind all differential positioning is to correct bias errors at one location with measured bias errors at a known position. A reference receiver, or base station, computes corrections for each satellite signal. Because individual pseudo-ranges must be corrected prior to the formation of a navigation solution, DGPS implementations require software in the reference receiver that can track all SVs in view and form individual pseudo-range corrections for each SV. These corrections are passed to the remote, or rover, receiver which must be capable of applying these individual pseudo-range corrections to each SV used in the navigation solution. Applying a simple position correction from the reference receiver to the remote receiver has limited

effect at useful ranges because both receivers would have to be using the same set of SVs in their navigation solutions and have identical Geometric Dilution of Precision terms (GDOP, not possible at different locations) to be identically affected by bias errors.

Differential corrections may be used in real-time or later, with post-processing techniques. Therefore, in this work, a kinematic DGPS program, Trimble Geomatic Office (TGO) in post-processing option was used.

The first crucial step in DGPS processing is the so-called static positioning process of the base stations, which are normally grounded on surface rock. Due to limited available outcrops it was also necessary to use ice grounded GPS stations. Because the ice sheet flows, the static GPS solution has limited value (only during flight time) or a model of ice sheet movement has to be calculated, see Kirchner (2002).

Static GPS processing was done twice within the VISA-project. First, calculations are done by the geodetic group of TU Dresden, using Berner software. Static ground stations are combined with a known station, i.e. SANAE 4, in the International Terrestrial Reference Frame (ITRF). A second calculation, within this work, uses the TGO software. Direct comparisons of both static solutions show similar results. For example the Weigel-Nunatak station (2002/2003), grounded on surface rock, displays differences in a range of Δ x=0.033 m, Δ y=0.012 m, Δ z=0.019 m.

With respect to the calculations of disturbing accelerations in gravity processing, differences in absolute positioning of the so called static GPS stations will not affect the result of the "relative position" of the aircraft.

Two kinematic datasets are available for the positioning of the aircraft, namely, those from the front and rear antennae solutions. Both receiver solutions are calculated and quality checked, in that we expected their spacing with respect to each other to be fixed at 4.5 m: the onboard spacing of the receivers. Irregularities are noted and, if necessary, the decision for one receiver solution was made. Furthermore, the acceptance of one receiver solution can be supported by a kind of statistical analysis, done by the TGO software.

The "variance of the probability distribution" can be defined as the relationship of the variance to the best and second-best solutions. A high value can be interpreted for the correct, or best, calculation. If the calculated variance is below the setting parameter, the output solution is set to false and the float solution is used.

The handling of the qualitative "variance of the reference" is not well documented, but seems to have characteristics of a-posteriori to a-priori analysis. A low value indicates a good comparison with the parameter settings and the model, but gives, in reality, no quality check, because a single spike can arise in a high value. Parameter settings for the TGO software, depending on 1 s data frame (kinematic) and 30 s data (static) are displayed in the Appendix A.

2.4 Aerogravity

Detailed theoretical descriptions of airborne gravity measurements are given by several authors, like LaCoste (1967; 1982; 1988), Harlan (1968), Childers (1999), LaFehr (1967; 1991), Nettleton (1960), Swain (1996), Vailliant (1991; 1976; 1992) and others. Here, just a summary of the main points is given to brief readers on the sensor system, refer to Boebel (2000) and Meyer (2004).

For all geodetic and geophysical tasks of airborne gravity, Newton's Gravitational Law is still valid. In rotating Earth's system the gravity potential is the sum of the potential of the gravitation and the potential of the centrifugal force. From the scalar field of the gravity potential, $\Phi(x)$, the gravitational acceleration, g_i, will be calculated by gradient operations:

$$g_i = -\nabla_i \Phi = \frac{-\partial \Phi}{\partial x_i} \tag{2.1}$$

with

$$\Phi(x) = -G \int_V \frac{\rho(x^{'})}{|x - x^{'}|} dV + \frac{{\omega_{earth}}^2}{2} d^2 \tag{2.2}$$

Here G = $6.67\,10^{-11}$ [$\mathrm{m^3 kg^{-1} s^{-2}}$], d is the orthogonal distance to the rotation axis, and ω_{earth} is the angular velocity of the Earth. The force f, which works on the test mass (gravimeter) is the product of its own mass and the gravity acceleration due to the density $\rho(x^{'})$ or mass distribution $\mu(x^{'})$. Gravity unit is $[10^{-5}\mathrm{ms^{-2}}] = 10^3\mathrm{Gal} = 1\,\mathrm{mGal}$.

Scalar gravity measurements will be recognized along the lot-line, as shown in figure 2.10. Measurement of the gravitational attraction on a moving platform is influenced by disturbances which for a given altitude, can be solved as follows:

$$\delta g(\varphi, \lambda, h, t) = \delta g_{sensor}(\varphi, \lambda, h, t) + \Delta_{inner_{error}} + \Delta_{outer_{error}} + \Delta_{corr} + \Delta_{redu} \tag{2.3}$$

$$\begin{aligned}
\Delta_{inner_{error}} &= sensor - dependent \\
\Delta_{outer_{error}} &= \tfrac{g}{2}(\epsilon^2_{x,initial} + \epsilon^2_{y,initial} + \ddot{r}_x(t) sin\epsilon_x(t) + \ddot{r}_y(t) sin\epsilon_y(t) \\
\Delta_{corr} &= \ddot{r}_z(t) + \Delta_{Etv}(\varphi, \alpha, \dot{r}_{aircraft}) \\
\Delta_{redu} &= \gamma(\varphi, \lambda, h_{normal}) + \Delta g(\varphi, \lambda, h_{normal}, t)_{tidal}.
\end{aligned}$$

φ, λ, h are set for geographic longitude, latitude and height above sea level, defined on a reference ellipsoid, with the definition of the normal gravity $\gamma(\varphi, \lambda, h_{normal})$. The flight height, h, is given above the ellipsoid. h_{normal} is the surface of the ellipsoid and t represents the time, related to the GPS system (most above WGS 84 and UT (World Geodetic System 1984 and Universal Time)). α is the flight direction, $\dot{r}_{aircraft}$ the aircraft velocity in the given flight height.

ϵ_x and ϵ_y are the orthogonal errors of leveling (tilt correction) for the longitudinal and transverse axes of the aircraft. $\ddot{r}_x$, $\ddot{r}_y$, $\ddot{r}_z$, are the corresponding orthogonal components of aircraft accelerations. g, the static gravity measurement on ground before take off, will represent the gravity level within the area of investigation.

The $\Delta_{outer_{error}}$ are representing the leveling mismatch (only if a scalar system is used). Errors due to vibrations are not taken into account as they will be eliminated using damping and filters within the instrument. Another assumption is that the time varying data are well synchronized. The measured gravity disturbance at flight level can be reduced to gravitational disturbances (reference on ellipsoid) and Free-air Anomaly (reference geoid).

The main task are pointed out as follows and yielding in the correction for Eötvös-effect, Vertical accelerations and Tilt correction.

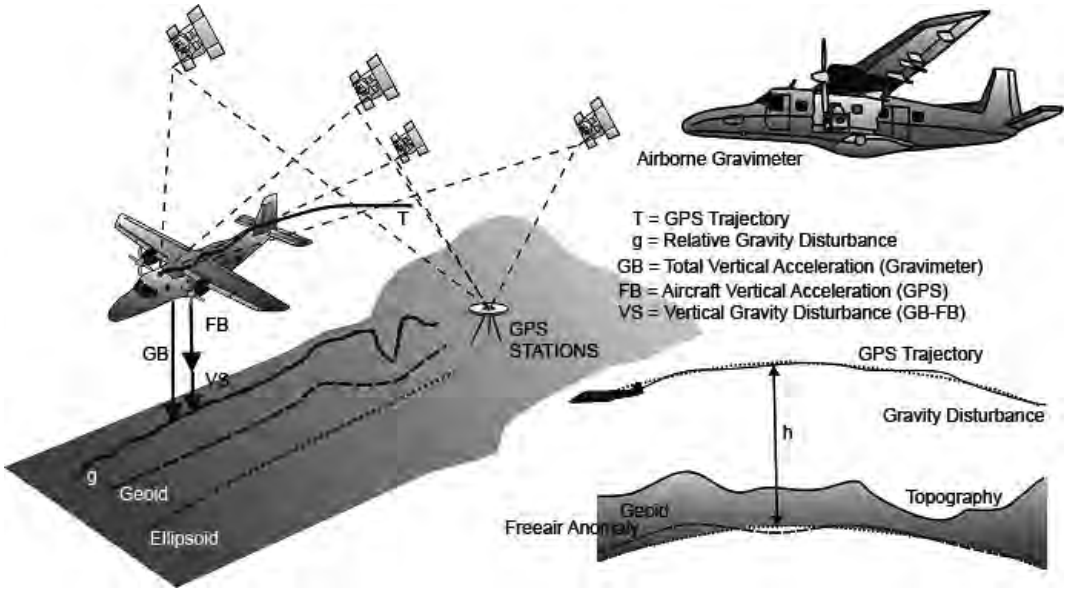

Figure 2.10: Principle of scalar gravimeter systems, adopted from Meyer, 2004.

2.4.1 Eötvös correction

In general, all types of gravity meters or accelerometers, when based on a moving platform, are affected by their motion over a curved, rotating Earth. The motion of a unit of mass in a rotating coordinate system is expressed by the vector equation [Harlan, 1968]:

$$a = \ddot{r} + 2\omega_{earth}\dot{r} + \dot{\omega}_{earth} \times r + \omega_{earth} \times \omega_{earth} \times r \tag{2.4}$$

with ω_{earth} = angular velocity, r = radius vector. This formula is the precise expression for the Eötvös correction and differs from the Eötvös' original expression in that is takes the aircraft speed into account.

Using the ellipsoidal coordinate system, the formula can be rewritten to correct for the Eötvös effect on airborne measurements, refer to velocities over ground and velocities in flight height, the effect due to measurements on a platform moving with respect to the Earth, Harlan [1968]:

$$\Delta_{Eotv} = \frac{\dot{r}^2}{a}(1 - \frac{h}{a} - \epsilon(1 - cos^2\phi(3 - 2sin^2\alpha))) + 2\dot{r}\omega_{earth}cos\phi sin\alpha(1 + \frac{h}{a}) \tag{2.5}$$

$$\Delta_{Eotv} = \frac{\dot{r}^2}{a}(1 - \frac{h}{a} - \epsilon(1 - cos^2\phi(3 - 2sin^2\alpha))) + 2\dot{r}\omega_{earth}cos\phi sin\alpha \tag{2.6}$$

Errors in navigation have a large impact in the Eötvös correction. Consequently, only the best possible navigation solution should be used for airborne gravity correction.

2.4.2 Vertical Accelerations

No gravity sensor can distinguish between gravity and platform acceleration. Therefore, any raw, relative scalar "gravity" measurement on a moving platform is actually the addition of the vertical acceleration and the change in gravity. Consequently, the accelerations have to be calculated using the GPS solution.

$$g_{sens} = g + \ddot{z} \tag{2.7}$$

Furthermore, during airborne operations, the instantaneous vertical accelerations are generally 10000 to 100000 times greater, and of much higher frequency, than the expected variation of the gravity signal. Solutions become less stable for high frequencies in vertical accelerations. It is therefore mandatory to filter the data. The amount of filtering is highly dependent on the quality of the gravity meter, the quality of the platform, and the flight conditions. Due to the problems described,

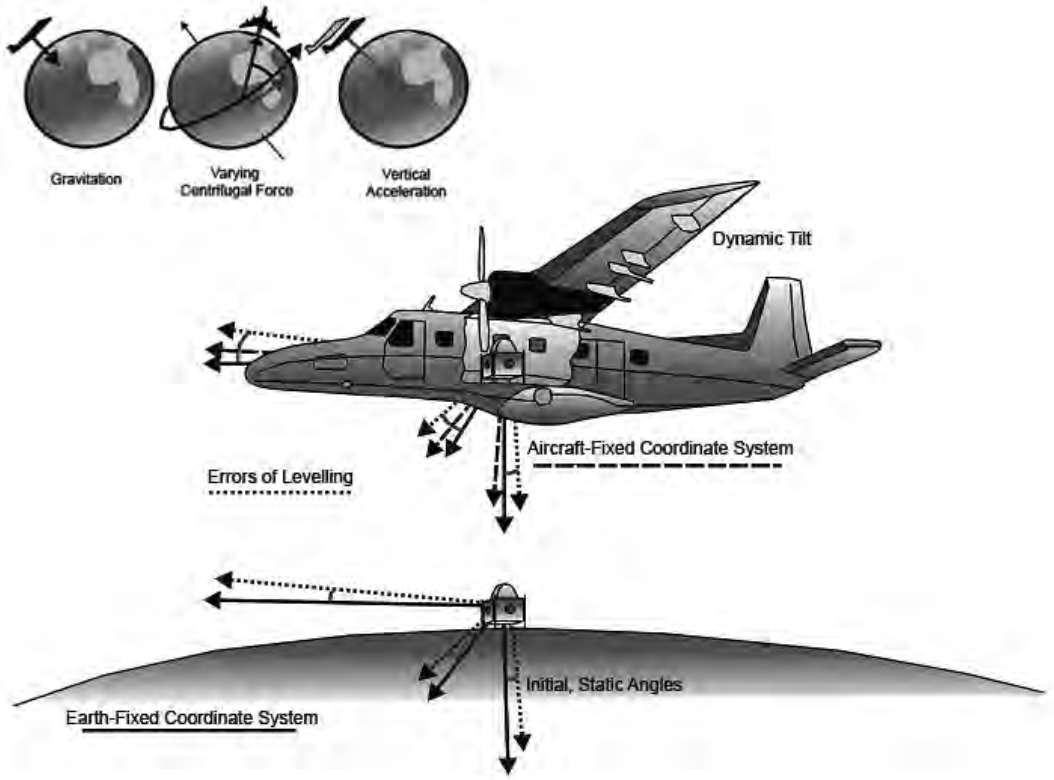

Figure 2.11: Effects on moving platform, adopted from Meyer, 2004.

the gravity meter response and the filter response must both be linear and stable in phase to avoid artifacts in the filtered and Eötvös-corrected data. Various filters are available, for example a Butterworth filter with a cut-off wavelength of 200 s and RC-filter (3x20 s), depending on data quality.

Filtering the data has an influence on the averaged gravity measurements as well as on the gradient in the vertical acceleration. Due to the fact that g and the platform are both sensor-dependent, the vertical accelerations must be calculated due to a non-inertial mass-system with the focus on non-implementation of mass distributions.

2.4.3 The scalar ZLS Ultrasys gravity meter system

The ZLS Ultrasys gravity meter system is based on the older LaCoste & Romberg S56 air/sea gravity meter. The sensor consists of a highly damped, zero-spring type gravity sensor mounted on a gyro stabilized platform with associated electronics.

The sensor incorporates a hinged beam supported by a zero-length spring. A zero-length spring is a spring whose equilibrium length, with a test mass attached, is zero (see figure 2.12). Damping of the large vertical accelerations due to the aircraft's motion is achieved through the use of internal air dampers.

Nevertheless, the vertical accelerations of the aircraft make it impossible to keep the beam constantly nulled. Therefore, it is necessary to read the gravity sensor whilst the beam is in motion. A mathematical analysis of the spring type gravity sensor shows that this is possible through observations of the beam position, the beam velocity, and the beam acceleration at any given time. If the beam motion is highly damped, the beam acceleration term can be neglected. If the gravity sensor has a very high sensitivity over a high range, the beam position can be neglected as well. The ZLS Ultrasys gravity meter fulfills both requirements. Accordingly, it can be read without nulling by measurement of the beam position parallel to the adjusted spring tension.

Utilizing the zero-length spring principle in a particular geometry results in a vertical suspension that can have infinite periods [LaCoste et al., 1988]. When the period is infinite and the torque exerted by the spring exactly balances the torque exerted by gravity, the beam will remain stationary at any position. When this position is achieved, the smallest change in gravity will cause the beam to rotate to one stop or the other. Thus, infinite period corresponds to infinite sensitivity [Valliant et al., 1992]. If the period is less than infinite and the beam is displaced from its equilibrium position, a restoring torque will return it back to the equilibrium position - this is the case for land gravity meters.

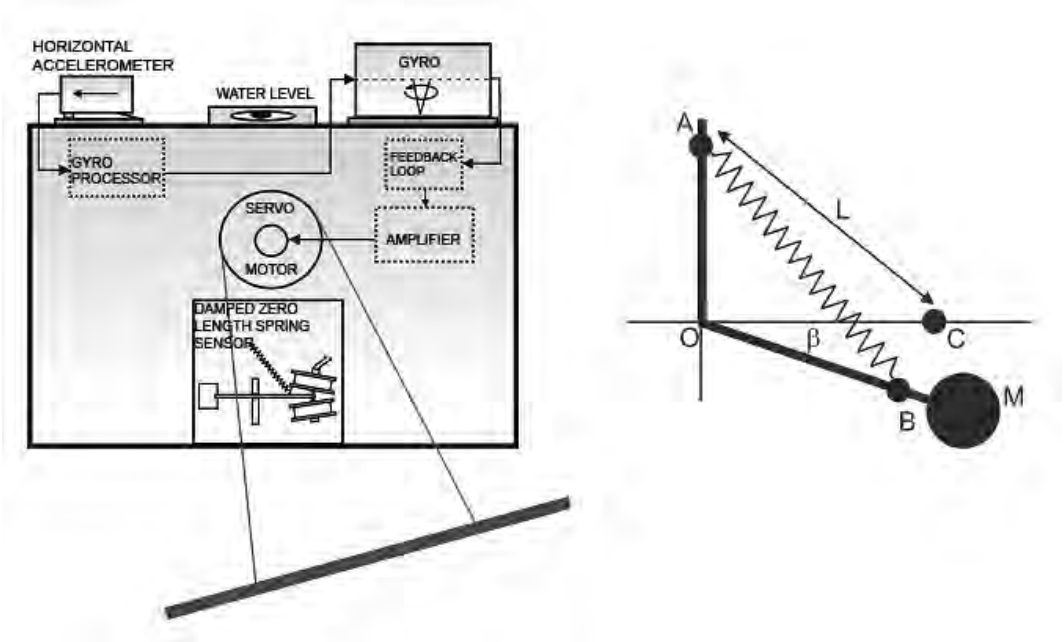

Figure 2.12: Simplified gravimeter (left) and sensor (right): The mass M is attached to the movable beam OB that is free to rotate about O. The beam is supported by a zero-length spring attached at the points A and B. In practice, the beam's total travel distance between top stop and bottom stop is some mm in the gravity meter.

So finally, for the gravity meter, the basic equation to gain the relative gravity at a given time, and thus at a given location, is:

$$\delta g_{sens}(\phi, \lambda, h, t) = ST + k\dot{B} + CC \tag{2.8}$$

The movement of the beam depends on ST (spring tension)- and is needed for the linear expression of worldwide measurements. The velocity of the beam, $\dot{B}$, itself is defined by the gravitational attraction, while the correction term, CC, named as Cross Coupling will be used for the mathematical expression of the sensor-mechanics. k is a constant, which is a function of the average beam sensitivity and the damping system.

For best performance and accuracy of the airborne gravity measurements it is imperative to keep the gravity meter system as close as possible to horizontal. For this task, a platform with two accelerometer and two gyroscopes is implemented.
The platform itself is controlled manually and levelled when the gravity meter is in an undisturbed environment.
The gyroscopes itself only measures the angular rates of the platform, which can keep the platform in the stable orientation, but delivers no information on its own about orientation. For this, the accelerometer input is needed.
The output signal of the accelerometer varies linearly with the tilt angle of the platform. The accelerometer signal is sent to the gyro processor in order that the signal is appropriately shaped for gyroscopes input.
The combined signals are filtered and sent to the servomotor to correct actual deviations of the platform from the horizontal. This Proportional-Integral Feedback algorithm maintains a stable platform that performs like a damped pendulum. The reaction time of this negative feedback loop is close to immediate but it has a limited "memory" due to the gyroscope drift. The memory time used with the filter is about 4 minutes for airborne application.

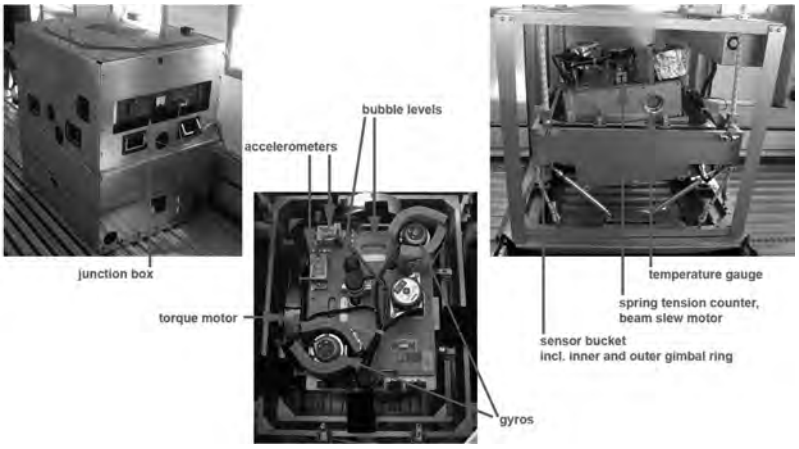

Figure 2.13: The scalar ZLS Ultrasys S56 Air/Sea gravity meter.

Table 2.2: Overview of gravity measuring systems, in use worldwide. In center of the table, the aircraft system used is shown. For VISA, this system will be the connection between satellite- and ground-based measurements as well and will be used to validate satellite gravity data, overview after Meyer (2004).

		satellite missions	
system	CHAMP	GRACE	GOCE
principle:	trajectory from GPS correction non- conservative forces by accelerometer	trajectory from GPS distance via microwave correction non-conservative forces by accelerometer	trajectory from GPS 3D accelerometer (gradiometer)
height:	450-300 km, decreasing	490-300 km, decreasing	250-200 km
velocity:	2700 km^{-1}, I=87°	2700 km^{-1}, I=89°	3000 km^{-1}, I=96.5°
error:	0.1-10 mGal, decreasing	0.1-5 mGal, decreasing	1 mGal
resolution:	650 km until Earth revolution	450 km until Earth revolution	100 km until Earth revolution
application:	global gravity and geoid	global gravity and geoid	global gravity and geoid
		aircraft missions	
system	long range	middle range	short range
principle:	scalar and vector gravity meter velocity and accelerations from GPS position by INS/IMU	scalar and vector gravity meter velocity and accelerations from GPS position by INS/IMU	scalar and vector gravity meter and gradiometer velocity and accelerations from GPS position by INS/IMU
height:	5-15 km	0.5-5 km	0.1-3 km
velocity:	750-1000 km^{-1}	200-300 km^{-1}	50-200 km^{-1}
error:	1-5 mGal	1-5 mGal	1-5 mGal
resolution:	20-8000 km, continental scale	5-500 km, regional scale	1-250 km, regional to local scale
application:	mountains, fracture zones deserts, ocean structures	mountains, fracture zones deserts, coastal structures	mountains, fracture zones marshes, deltas
		surface missions	
system	ship and submarine	airborne-point	surface
principle:	scalar gravity meter velocity and accelerations from GPS position by INS/IMU	scalar gravity meter one point measurement observatory studies	scalar gravity meter and gradiometer
height:	sea surface	topography	topography
velocity:	10-30 km^{-1}	-	-
error:	1-5 mGal	0.1-2 mGal	0.1-2 mGal
resolution:	0.1-1000 km	0.1-300 km	0.1-300 km
application:	oceanic structures	regional to local structures	regional to local structures

2.4.4 Aerogravimetry Data Processing

Airborne-based gravity measurements are the difference of two data records: gravity signal and accelerations from flight trajectory.

The kinematic differential GPS data are computed in the initial phase of data processing. The second primary data input are the raw gravity readings from the gravity meter.

This subtraction requires precise synchronization of both datasets. To ensure this, the symmetry of the cross correlation between gravity signal and vertical acceleration is used (Olesen and Fosberg, 1997).

After synchronization is ensured, the vertical aircraft accelerations are computed from the GPS heights, as well as the horizontal accelerations from the positions in the X and Y directions, yielding the Eötvös correction, Tilt correction, and Free-air reduction. All these computations are applied within the unfiltered, common 1 Hz data frame. Once all corrections and reductions are applied, the data are low-pass filtered, with filter choice, depending on data quality and flight behavior. Optional low-pass filters are 3x20sec RC, Infinite Impulse Response (IIR), Butterworth and Finite Response (FIR). The final result is further reduced for the normal gravity field and related to sea level, thus reaching the Free-Air Anomaly, having a mean spatial resolution of about 6.5 km.

2.4.5 Gravity data corrections

To compare measurements made at different sites, several corrections must be applied to the datasets:

$$\delta g = \delta g_m - \delta g_t - \delta g_l - \delta g_d - \delta g_{fa} - \delta g_b - \delta g_{ice} - \delta g_w - \delta g_{topo} \tag{2.9}$$

δg_m	value determined in the field,
δg_t	correction for tides, neglected for airborne operations,
δg_l	correction for geographic latitude,
δg_d	correction for instrumental drift,
δg_{fa}	Free-air correction.

The first four corrections result in the **Free-air Anomaly** by subtracting the latitude correction (theoretical gravity) from the absolute gravity and adding a correction for the station elevation.

The **Bouguer Anomaly** is the result of correcting the Free-air anomaly for the mass of material that exists between the station elevation and the spheroid. In the Antarctic there are four typical cases for correction for different media: rock only; ice/rock; ice/water/rock; water/rock, such that:

$$\delta g_{ba} = \delta g_{fa} - 0.0419088[\rho h_s + (\rho_w - \rho)h_w + (\rho_i - \rho_w)h_i] + \delta g_{curv} \tag{2.10}$$

in which

δg_{ba}	Bouguer anomaly [mGal],
δg_{fa}	Free-air anomaly [mGal],
ρ	Bouguer density of rock [gcm^{-3}],
ρ_w	Bouguer density of water [gcm^{-3}],
ρ_i	Bouguer density of ice [gcm^{-3}],
h_s	station elevation [m],
h_w	water depth [m] including ice,
h_i	ice thickness [m], and
δg_{curv}	curvature correction.

The additional curvature correction converts the geometry for the Bouguer correction from a infinite flat slab to a spherical cap whose thickness is the elevation of the station and whose radius from the station is 166.735 km. The formula from LaFehr (1991) was applied.

The **Complete Bouguer Anomaly** is the result of correcting the Bouguer anomaly for irregularities in the Earth due to terrain in the vicinity of the observation points.

$$\delta g_{cba} = \delta g_{ba} + \delta g_{tc} \tag{2.11}$$

The terrain corrections are calculated using a combination of the methods described by Nagy (1966) and Kane (1962), which calculate the regional terrain correction from a coarse regional Digital Elevation Model (DEM) draped over a more finely sampled local DEM that covers the survey area. For this purpose, a more regional DEM from the BEDMAP database and, for the local DEM, VISA's own calculated DEMs was used. This yields in a regional correction grid that represents the terrain correction beyond a local correction distance.

2.5 Aeromagnetic

The success with which the magnetic method can be applied depends on the contrast in magnetic properties of the rock types concerned. These magnetic properties arise from the presence of magnetic minerals such as magnetite, pyrrhotite, ilmenite, franklinite and specular hematite in the rock. By far the most common of there minerals is magnetite. The magnetic effect of rocks is almost entirely due to their magnetite content.

Crustal rock material becomes magnetized within the core field, the inducing field on the magnetic minerals in the crustal material. Magnetic domains within the minerals align themselves in the direction of the inducing field and thereby generate their own magnetic field, which is superposed on the core field. This causes anomalies in the smoothly varying core field.

The main magnetic field generated in the Earth's core and that induced in the crust are both vector quantities, which interact with each other. At Earth's surface, only the magnitude of this resultant force is measured by the magnetometer. A further complication is that the field present in the crustal rocks consists of two parts, a remanent or permanent field and the temporarily induced field describes above. The strength of the induced field is proportional to the core field and parallel to it. Remanent magnetization represents a remnant of the magnetic field imprinted at an earlier stage in the Earth history.

The magnetization is a measure of the magnetic polarization $\mathbf{M}$. The magnetic field is proportional to the magnetizing field $\mathbf{H}$:

$$\mathbf{M} = k\,\mathbf{H} \tag{2.12}$$

Since $\mathbf{M}$ and $\mathbf{H}$ are both measured in [Am], the susceptibility k is dimensionless in the SI system. The magnetic induction, $\mathbf{B}$ (unit: [nT]) is the total field, including the effect of magnetization:

$$\begin{aligned} \mathbf{B} &= \mu_0\,(\mathbf{M} + \mathbf{H}) && (2.13)\\ &= \mu_0\,(1 + k)\,\mathbf{H} && (2.14)\\ &= \mu\,\mu_0\,\mathbf{H}\,. && (2.15) \end{aligned}$$

Magnetized matter contains a distribution of microscopic magnetic moments. Unpaired electron spins are the most important sources of magnetic moment. Magnetization, $\mathbf{M}$, is defined as the magnetic dipole moment per unit volume of the material. Induced magnetization, $\mathbf{M}_{ind}$, is the component of magnetization produced in response to an applied field. The induced magnetization varies in proportion with changes in the applied field and vanishes when the field is removed. Remanent magnetization or remanence, $\mathbf{M}_{rem}$, is the permanent magnetization that remains when the applied field is removed, and is essentially unaffected by weak fields.

The total magnetization is the vector sum of the induced and remanent magnetizations:

$$\mathbf{M} = \mathbf{M}_{ind} + \mathbf{M}_{rem} \tag{2.16}$$

For sufficiently weak fields, such as the geomagnetic field, the induced magnetization is approximately proportional to the applied field.

For most rock, the induced magnetization is essentially parallel to the applied field, irrespective of the field direction. In this case the susceptibility is a scalar quantity, i.e. it is characterized simply by its magnitude and is isotropic. The Koenigsberger ratio, Q, is a convenient parameter for expressing the relative importance of remanent and induced magnetizations. It is given by:

$$Q = \frac{\mathbf{M}_{rem}}{\mathbf{M}_{ind}} = \frac{\mathbf{M}_{rem}}{k\mathbf{H}} \tag{2.17}$$

Thus, $Q > 1$ indicates that remanence dominates induced magnetization, whereas $Q < 1$ implies that the induced magnetization is dominant.

2.5.1 Processing of Airborne Magnetic Data

The processing of aeromagnetic flight line data to a grid of values ready for the application of enhancement techniques and interpretation involves the following sequential process: editing, correction for diurnal effects, the levelling of all data to a common base and removal of the core magnetic field and, finally, the application of a gridding algorithm.

Thus, the overall processing of aeromagnetic data involves the following major steps in two phases:

Phase 1-Pre-processing:

- Verifying and editing the raw data
- Merging the raw magnetic data with the flight path coordinates via GPS time

Phase 2-Processing:

- Removing diurnals
- Removing the component attributable to the core field (IGRF correction)
- Levelling the data
- Gridding and contouring

Despite this, sources of errors still exist and are listed as follows:

Magnetometers: Modern magnetometers give absolute measurements with high sensitivity and virtually no drift and, to all intents and purposes, can be regarded as giving an exact reading. The noise envelope of the Geometrics CS-2 Magnetometer used is 0.2 nT including all orientation errors.

Aircraft effects: The magnetic signature of the aircraft consists of three components, namely those due to its permanent magnetization, the magnetization induced by the motion of the aircraft through the Earth's magnetic field, and that due to the flow of electrical currents within the aircraft. The permanent magnetization of the aircraft leads to the familiar heading errors caused by the vector addition of the aeroplane's induced field to Earth's field. Higher frequency errors are introduced by aircraft movements and is called manoeuvre noise. The general method for removing these effects is called compensation, and involves measuring the pitch, yaw and roll of the aircraft. The use of feedback compensators (flying periodic manoevers in each direction) will detect these additional field components and allow to remove them in real time.

Navigational effects: The availability of the Global Positioning System (GPS) improved the quality of navigational data, in this case to positional accuracies of better then 1.5 m for the x- and y directions.

IGRF: The main component of the measured magnetic field originates from the magnetic dynamo in the earth outer core. This field is preliminary bipolar, with amplitudes of 50000 nT, but spherical harmonic terms up to about order 13 are significant. Since the core field is much larger than that due to crustal magnetization, and since it has a significant gradient in many parts of the world, it is desirable to remove a model of the global field from the data before further processing. The model most widely used today is the International Geomagnetic Reference Field (IGRF). The IGRF is modified every 5 years and includes coefficients for predicting the core field into the near future. The contour values of 47000 nT in the unprocessed data show that the regional (non-geologic) field component still persists in the magnetic data. So it was necessary to remove the regional field as approximated by the IGRF for the corresponding epoch of the survey from the total magnetic field (observed value) to obtain the anomalous field due to crustal sources according to normal convention.

Time variation in the magnetic field (diurnal): Earth's magnetic field varies with time. The variations can be random or cyclic, varying from effects of the 11 year sunspot cycle (secular variation) down to geomagnetic pulsations with periods of the order of seconds. To remove these effects a stationary magnetometer that simultaneously measures the time varying magnetic field for later subtraction from the survey data is necessary. There is still considerable debate on how many such base stations are needed to adequately sample the spatial variations of the external field for large surveys or when the survey area is at a considerable distance from the base of operations.

Ground clearance and altitude variation/common datum: The amplitude of local magnetic anomalies varies with distance from the recording instrument, i.e. with respect to the ground clearance of the aircraft. The rate of change increases as the wavelength of the anomaly decreases. Earth's magnetic field thus varies with height above the ellipsoid. Typically, the rate of change with height is $0.025\,\mathrm{nT\,m^{-1}}$. Because the surveys were carried out at different flying heights, ranging from 1500 to 4500 m, all the line data and grids needed to be reduced to a common datum. A datum of 3500 m was chosen because the majority of the data under consideration were flown at that heights. Difficulties arise with data of VISA III-campaign, for which a few lines were flown at 4500 m, and downward continuation produced poor results (see chapter Surveys and Database).

Levelling: Some flight path errors were evident in the initial grids as narrow elongate anomalies along the flight lines. This noise is often prominent in that it interrupts the real anomaly pattern of the images, making it difficult to interpret real anomalies. Thus, it was necessary to minimize this effect. Levelling using tie lines was originally developed as an alternative method to the use of base stations. Nowadays it is a standard step after base station corrections. The purpose today is to minimize residual differences in level between adjacent lines, and the long-wavelength errors along lines that inevitably remain after compensation and correction for external field variations by base station subtraction. The differences in field value at the intersections of lines and tie lines are calculated, and corrections are applied to minimize these differences. The most common method is to calculate a constant correction for all lines by least squares fitting, sometimes using a low order polynomial. Another method is to treat the tie lines as fixed and to adjust only the survey lines. Note that all these procedures are empirical.

Gridding: The x y z data were gridded separately for each data set using the Minimum Curvature Interpolation Method. As the spacing of the flight lines is approximately 10 km, except in parts of the VISA III-campaign where it is 20 km, and the track spacing reaches 66 m, a grid cell size of 3 km was chosen to reconstruct the crustal anomalies.

2.6 Data Visualisation

Gridded data were used to produce images and maps for interpretation at suitable scales for the complete region as well as interesting fragments, using the Lambert Conformal projection (2sp).

Maps were interpreted to identify regional features like tectonic boundaries between cratons and mobile belts, major faults and shear zones, dykes etc. Qualitative interpretation involved zoning of a map by outlining zones with distinct characteristic anomaly patterns. Thus, zoning helps in mapping the subsurface extents of geological units. Total Magnetic Intensity (TMI) maps were used for zoning, Tilt derivative (TDR) maps were used to delineating linear features, and the Analytic Signal (AS) for simplification of complex magnetic anomalies. Furthermore, calculation of Complete Bouguer Anomaly, Isostasy- and Curvature discussions are used to define structural boundaries as well.

Presently, two procedures exist for the interpretation of potential field data, namely the solution of the so-called direct and indirect cases. The indirect problem deals with theoretically-calculated anomalies based on a postulated model which is altered and compared with the observed anomaly until a reasonably "good fit" is obtained. When the body parameters are calculated directly from the observed magnetic field a direct interpretation approach is used. Considering this, it must be borne in mind that the accuracy of any quantitative analysis is reduced by three main factors:

- Imperfect source body geometry, e.g. deviation from flat top and parallel sides and infinite depth extension,
- Heterogeneity of i) the magnetic susceptibility, e.g. chilled margins will be finer grained and thus of a lower susceptibility, ii) density contrasts,
- remanent magnetism.

Due to the fact that geological control on Antarctic anomalies is lacking or limited to nunataks, the huge extent of the compiled surveys and the more regional aspect of the project lead to the decision only to apply direct methods and interpretation techniques. Magnetic interpretation of terrains in particular is often difficult, due to their complex geological and tectonic evolution, resulting in uneven distributions of magnetic minerals, polyphase deformation and associated metamorphism and variability in remanent magnetization.

The use of different Fourier filtering techniques will enable numerical analysis and interpretation of potential field data. All the filter outputs are based on the measured field and are limited by the data quality, the quality of filter techniques and the observer's experience. Sharpening filters, such as high-pass, downward continuation, vertical and horizontal derivatives are useful to enhance short wavelength features. The opposite effect can be realized with smoothing filters, like low-pass-filter and upward continuation, to enhance longer wavelength features. A third class of task includes transformations to convert data from one phase to another, for example by Reduction to the Pole.

2.6.1 Basic Interpretation of Magnetic Anomalies

Magnetic interpretation is somewhat complicated by the fact that the magnitude and shape of the anomaly is not only related to the magnetic mineral content, depth and attitude of the causative body but also to its attitude or orientation to the direction of the inducing field. It may be further complicated by the presence of remanent magnetism often in a different direction to that of the present magnetism induced field component.

The amplitude is determined by the depth, the magnetic susceptibility of the body, the magnitude of the inducing field and to a lesser extent by the attitude of the body. Surprisingly though it may seem, amplitude is of least interest in interpretation. This is because of the large ranges of susceptibilities of apparent similar rock types.

The shape of the anomaly is of prime importance. From the shape it is possible to determine the depth below the surface, the dip and to get some idea of the dimensions of the body.

As already known by potential field data its often not possible to distinguished between different types of the body geometry, like sphere and horizontal cylinder or vertical cylinder, vertical thin dyke and thick dyke structures. The thin dyke is a very common form of magnetic body and beside true intrusive dykes many other geologic bodies take on the form or appearance of a dyke. A thin dyke is defined as a sheet like body extending in strike to infinity and extending from surface or subsurface to infinite depth and having a width of less then one-third of the depth to the top of the body.

As mentioned, the anomaly shape stays in relation to dip, strike, depth and magnetic inclination. For a deeper interpretation they are several catalogs and tables available, which display these relationships, refer to body geometry. These help was used within the detailed interpretation.

2.6.2 Total Field Shaded Relief Map

Directional sun-shading of the data can be done with varying inclination (elevation) and declination (azimuth) angles of the illumination source. Shaded relief images prove to be useful in determining geological strike and delineating linear features like faults, shear zones etc. as they enhance the visibility of features in a desired direction and suppress those in other directions. In essence, a shaded relief image represents the first horizontal derivative in a given direction. As such, the near surface features that are not well resolved in a simple color raster map tend to appear more prominently in shaded relief maps.

2.6.3 Derivative Based Filters

The first vertical derivative is theoretically equivalent to observing the vertical gradient directly with a magnetic gradiometer. A vertical derivative map enhances the response from shallow sources, suppressing deeper ones by enhancing high-wavenumber components of the spectrum. Thus, closely-spaced sources can be better differentiated on derivative maps. The (first) vertical derivative, $n = 1$, sharpens the anomaly amplitudes, thus helping in the identification of more geological features.

$$L(\omega) = \omega^n \tag{2.18}$$

and uses ω as angular wavenumber in radians per ground units as well as n as order of differentiation.

The use of horizontal derivatives can be useful for the identification of geological boundaries:

$$L(\omega) = (\omega i)^n \tag{2.19}$$

2.6.4 Curvature attributes

The aim of the curvature analysis is to improve visualization of potential data and hence optimize interpretation. The analysis of horizon attributes is not new at all, but already have a prowen track record in many disciplines, e.g. medical brain scanners, Optometry and Terrain Analysis. The application of curvature attributes to potential field data is described by Kollersberger (2005).

Curvature attributes are related to surface attributes. The term surface is taken to mean any surface, which is either flat, interpreted or used to control a window from which a volume attribute can be extracted (Roberts, 2001).These surface-related attributes can be grouped in: *surface-associated* attributes are those which use a surface to extract values from a secondary data source, e.g. seismic amplitude, volume attributes. *Surface-derived* attributes are computed directly from the surface itself (dip, edge and azimuth). Within this category, curvature falls into a separate group, the second derivative attributes, which includes Laplace-based attributes. The third category involves *surface-rendered* attributes, like shaded relief and 3D visualization.

Curvature is a two-dimensional property of a curve and describes how bent a curve is at a particular point on the curve, i.e. how much the curve deviates from a straight line at this point ($K = dw/ds$ rate of change of angle dw with respect to the arc length dS). For one point P on a curve the curvature can be defined by means of the radius of curvature R of the osculated circle, i.e. possesses that circle of the one common tangent T with this curve. Then one gets the simple connection that the curvature K is the reciprocal of the radius of curvature R: $K = 2\pi/2\pi R = 1/R$.

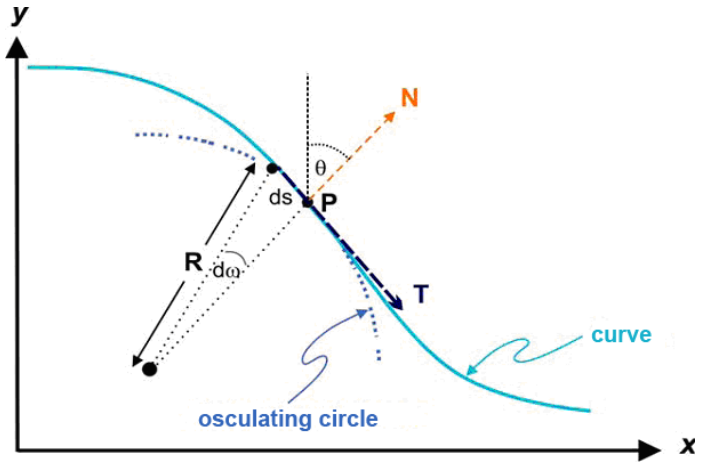

Figure 2.14: Definition of curvature: For a particular point P on a curve, the curvature can be defined in terms of the radius of curvature, R of the osculating circle. This circle possesses a common tangent T with the curve. N is the vector normal to the curve at point P, which defines the local dip angle θ. The curvature at point P is defined as the reciprocal of the radius of curvature.

The smaller the radius of curvature, the more strong the curvature of the curve is defined. Over the entire range of a circle the curvature is constant. The curvature K is related to the 2nd derivative of a curve.

For interpretation purposes, surface anticlines will yield in positive curvatures, synclinal surfaces will yield in negative curvatures and saddles will yield both. Ridges will yield positive curvature in the direction across the ridge (zero curvature in the direction along). Troughs will yield negative curvature in the direction across and zero curvature along the trough line. More than 40 attributes are available and only the applied techniques are briefly described.

Dip angle: extracts the curvature in the direction of maximum dip as a measure of the rate of change of dip in the maximum dip direction, magnitude and direction of faults is preserved, method of first derivative.

Azimuth: indicates from point of view the angle distance between point which are on horizontal circle and the north pole, indicates changes in properties, method of first derivative.

Minimum curvature: smallest curvature values are computed and illustrated, if the minimum values are very small or zero, then their surface is evolved. if the minimum values are very large, then minimum curvature shows where it folds or the break came, this attribute is suitable more for bodies with small density/susceptibility contrast.

Maximum curvature: the maximum curvature stands perpendicularly to the minimum. is suitable for distinguishing disturbances in geometry, moreover, the curvature defines the orientation of these disturbances, positive curvature values indicate the ascending side and the negative values show the sloping side, distinction between disturbances and other lineaments is possible, however, due to enormous information

contained in the data at times it could be confusing.

Most negative/positive curvature: is suitable only for seeking out lineaments, here one can recognize nearly each individual lineament within a surface, it is possible to filter the size of the lineaments and get generally better resolution in identifying lineaments.

Dip curvature: attribute is called also "profiles curvature" and computes the idea curvature, this is the process of extracting curvature in the direction of maximum breaking and is a measure of the rate of the change of the angle of incidence toward the maximum angle of incidence, size and direction of the disturbances are conserved, method bends and exaggerates each local relief contained within the surface and can be used to increase the differential connectivity characteristics.

Strike curvature: gives an extraction of the curvature in a direction, which runs in the angles to the "Dip Curvature"(along the impact), separates the surface into ranges of descending forms and edges.

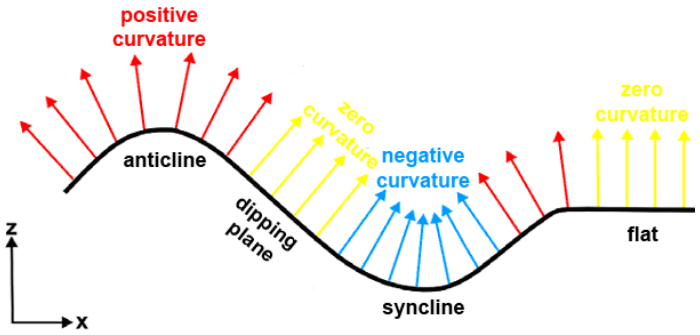

Figure 2.15: Sign convention for curvature attributes: Arrows represent vectors, which are normal to the surface. Where these vectors are parallel on flat or planar dipping surfaces, the curvature is zero. Where the vectors diverge over anticlines, the curvature is defined as positive and where they convergence over synclines, the curvature is defined as negative.

The analysis of curvature attributes has been done using topography, gravity and magnetic data and with the help of algorithm as describes by Robertson (2001). The curvature-code was written by Dr. S. Schmidt, Geophysics Division, at Christian Albrechts University Kiel.

Each of the attributes gives slightly individual insight into the mapped surface depending on the step and size of the analyzing window used. It may be possible to differentiate between local (short wavelength and related to near surface anomalies) and more regional/global (long wavelength) anomalies. Regional (50 km analyzing window) and local (10 km analyzing window) characteristics of the data are presented in the APPENDIX D.

No surface attribute should be used in isolation and must be interpreted with reference to the origin. Within this thesis, the focus lies not within a detailed analysis of curvature attributes.. The displayed attributes do not belong to specific physical properties. The aim of the selected comparison (local and regional) is to identify

similarities to outline geologic structures (more quantifying then qualifying). Thus, in combination with the more classical interpretation methods (see chapter Data Visualisation), the Curvature analysis will lead to the combined terrain model of DML lithosphere.

2.6.5 Analytic Signal

The interpretation of observed magnetic anomalies is often complicated by their horizontal displacements with respect to their sources. This displacement, or skewness, results from the fact that the directions of the geomagnetic field and induced magnetization are, in general, not vertical. Repositioning of anomalies by reduction to the pole can be complicated, when magnetization inclination is low. Most methods assume knowledge of the orientation of the present day magnetic field and of the source body magnetization. The inclination and declination of the present day magnetic field are well known. In the absence of oriented magnetic samples, one often assumes that the source body magnetization is purely induced; an assumption that is very often not justified. The Analytic Signal is given by:

$$A(x,y) = \sqrt{(\frac{\partial T}{\partial x})^2 + (\frac{\partial T}{\partial y})^2 + (\frac{\partial T}{\partial z})^2} \tag{2.20}$$

where T is the observed field at x and y. While this function is not a measurable parameter, it is extremely interesting in the context of interpretation, as it is completely independent of the direction of magnetization and the direction of the inducing field. This means that all bodies with the same geometry have the same analytic signal. Furthermore, the peaks of analytic signal functions are symmetrical and occur directly over the edges of wide bodies and directly over the centers of narrow bodies. Under the assumption that the anomalies are caused by vertical contacts, the analytic signal can be used to estimate source depth using a simple amplitude half-width rule (accuracies in depth determination are in the order of 30%). This avoids the difficulties that are often faced in the conventional process of reduction to pole for δT, when the effects of natural remanent magnetization on the source magnetization distribution are usually unknown. The implementation of the AS calculation has three steps.

- low-pass filtering of δT
- processing to obtain the gradients of δT with respect to the x, y and z directions
- calculation of the AS

The calculation of the AS is illustrate in figure 2.16, which shows how it results in the determination of source characteristics without making assumptions about the direction of source body magnetization.

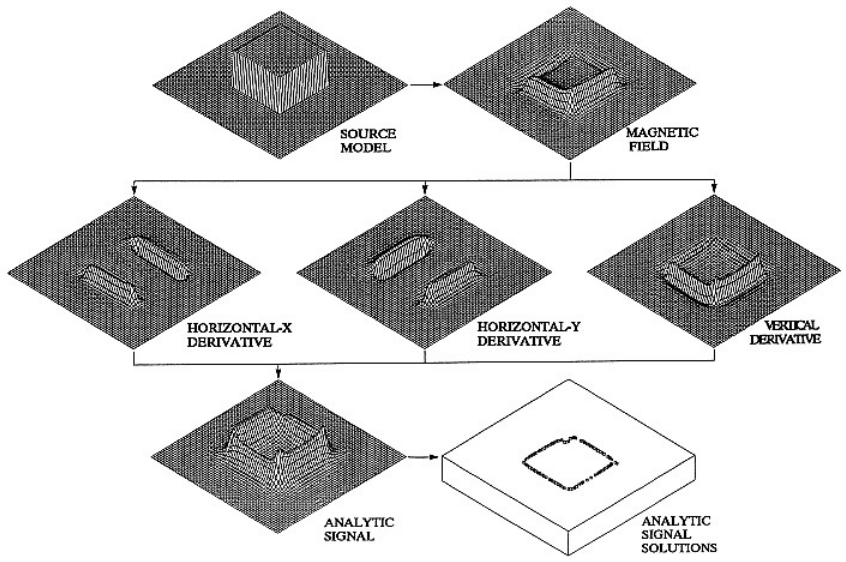

Figure 2.16: Schematic outline of the Analytic Signal, after Roest (1992).

However, the data should nevertheless be interpreted with care for the following reasons:

- The amplitude of the analytic signal varies with the effect of magnetization, and therefore remains a function of the ambient magnetic field parameters.
- The analytic signal over magnetization contrasts that are closely spaced or dipping are more complicated than the assumed bell-shape function found over a single contrast.
- The analytic signal over structures that intersect at an acute angle is complicated because of the nonlinear combination of signals.
- The calculation of the analytic signal is based on derivatives of the magnetic anomalies, so that gridding artifacts, errors like track corrugations, and noise in general, are all enhanced.

Processing was realized with Geosoft Oasis montaj software.

2.6.6 Tilt Derivative

Derivatives of potential field data can help define and estimate the physical properties of the source structure causing the anomaly. The *tilt derivative* is highly suitable for mapping shallow basement structures and has distinct advantages over many conventional derivatives.

The problems to overcome in determining the shape and edges of magnetic source structures are to identify and map:

- subtle anomalies attenuated in dynamic range due to the presence of high amplitude magnetic anomalies
- continuity of individual bodies that feature lateral changes in susceptibility and /or depth of burial and
- edges of structures by adequately accounting for the nature of the rock magnetization. Rock magnetization is a vector quantity that can consist of both remanent and geomagnetically induced components. The remanent component can affect the shape of the magnetic field response and result in spurious derivatives

The complex Analytical Signal for 2 D structures is

$$A(x, z) = |A|^{j\theta} \tag{2.21}$$

with the known Analytical Signal:

$$|A| = \sqrt{(\frac{\partial T}{\partial x})^2 + \frac{\partial T}{\partial y})^2} \tag{2.22}$$

where T is the magnitude of the total magnetic intensity (TMI) and $\theta = \tan^{-1}[\frac{\partial T}{\partial z}/\frac{\partial T}{\partial x}]$ is the local phase.
The tilt derivative is similar to the local phase, but uses the absolute value of the horizontal derivative in the denominator:

$$TDR = \tan^{-1}[\frac{VDR}{THDR}] \tag{2.23}$$

with VDR and THDR as the first vertical and total horizontal derivatives, respectively, of the TMI.

The important points to note about the tilt derivative are:

- the AS is invariant for all inclinations
- it normalizes a magnetic field image and discriminate between signal and noise

Processing was realized with Geosoft Oasis montaj software.

2.6.7 Depth Estimation

Potential field data have, by their nature, a very broad band of information in a single measurement that includes the contributions due to all physical sources (geology). The resolution of different sources is dependent on the noise levels of the measuring system and on the ability to resolve overlapping signals. Roughly qualitative information is given by a spectral analysis of gridded data. The energy spectrum is a 2D function of the energy relative to wavenumber and direction. The radially averaged energy spectrum is a function of wavenumber alone and is calculated by averaging the energy in all directions for the same wavenumber.

When considering a grid that is large enough to include many sources, the use of the log spectrum of this data is useful to determine the statistical depth to the tops of an 'ensemble of sources', using the relationship (see Spector and Grant, 1970):

$$logE(k) = 4\pi hk \tag{2.24}$$

where h is the depth in ground units and k is the wavenumber in cycles/ground units.

The Nyquist wavenumber, N, is the largest wavenumber that has been sampled by the grid, and is defined as one over twice the grid cell size.

$$N = 1/(2 * cellsize) \tag{2.25}$$

If the gridded cell size is 3 km, the Nyquist wavenumber is 0.16 km. Furthermore, the smallest detectable depths are defined using the size of the grid cell by:

$$h_{min} = 0.4\delta x \tag{2.26}$$

The grid cell size of VISA data is 3 km, which leads to an estimate of the smallest detectable source at 1.2 km depth.

It is possible to determine the depth of the source ensemble by measuring the slope of the energy spectrum and dividing by 4π. A typical spectrum may exhibit three parts: a deep source component, a shallow source component and a noise component.

However, in conjunction with the finite detectable wavelength (wavenumber), defined by the Nyquist frequency (see above), it is difficult to define a full ensemble of sources. Due to this, a 5 point average slope of the energy spectrum is used, and will be illustrated in the solutions of the approximate depth calculations (see APPENDIX C).

Note that the estimation of linear trends for the ensemble of sources is strongly subjective. For an a exponential value (energy), the estimation of the depth will be calculated using linear approximation of trends. The qualitative aspect of this trend

of interpretation is that, for the increasing depth solution, the error also increases. For low frequencies, only a few points are recognized in contrast to high frequency anomalies. This is due to the transformation process from the space domain (grid) to the wavenumber domain. Consequently, the solutions from this analysis can only be used as a rough guide in qualitative interpretation.

2.6.7.1 3D Euler Deconvolution

The objective of the 3D Euler process is to produce a map that will show the locations and corresponding depths of the geologic sources observed in a two dimensional grid.

The Standard 3D Euler method is based on Eulers' homogeneity equation, that relates the potential field and its gradient components to the location of its sources, by the degree of homogeneity N, which may be interpreted as a *structural index* [Thompson, 1982]. The *structural index* is a measure of the rate of change with distance of a field.

The calculation uses a least squares method to solve Euler's equation simultaneously for each grid position within a sub grid (a square grid that is moved along each grid row). At each grid point, there will be 10 grid window equations, from which the four unknowns (x,y,z as location and the background value) and their uncertainties are obtained for the specific *structural index*. A solution is recorded if the depth uncertainty of the calculated depth is less than a specific tolerance and the solution is within a limiting distance to the center of the data window.

Any 3-dimensional function $F(x, y, z)$ is to be *homogeneous* at the degree n if the function obeys the expression:

$$F(tx, ty, tz) = t^n F(x, y, z) \tag{2.27}$$

From this, the Euler's equation can also be satisfied:

$$x\frac{\partial F}{\partial x} + y\frac{\partial F}{\partial y} + z\frac{\partial F}{\partial z} = nF \tag{2.28}$$

An anomaly over an idealized symmetrical source can be written as:

$$F(x, y, z) = \frac{K}{r^N} \tag{2.29}$$

with $r^2 = (x-x_0)^2+(y-y_0)^2+(z-z_0)^2$, (x_0, y_0, z_0) is the position of a source whose field f is measured, K a constant and N a real number, which depends on source geometry, the measure of the fall-off rate of the field, and which may be interpreted as the structural index (SI) and thus equivalent to $-n$ in Euler's equation. The equation is homogeneous of grade $n = -N$.

For $z = 0$, the observation plane, Euler's equation can be re-stated as:

$$(x - x_0)\frac{\partial F}{\partial x} + (y - y_0)\frac{\partial F}{\partial y} + (z_0)\frac{\partial F}{\partial z} = -NF(x, y, 0) \tag{2.30}$$

Thus, Euler deconvolution provides an excellent means of gaining a broad indication of the depths and locations of various sources in a given area, provided appropriate dimensions are selected for parameters like the grid cell size, window size and structural index. Euler deconvolution is a faster method of covering the whole area for depth and boundary estimation of sources than modeling individual anomalies. It also helps in delineating linear features more precisely, as focused solutions cluster along these features.

The significant advantage of Euler deconvolution for magnetic data is that it is insensitive to the effects of magnetic inclination, declination and remanence.

The following table summarizes the structural index for simple models:

geologic model	number of infinite dimensions	magnetic SI	gravity SI
sphere	0	3	2
pipe	1(z)	2	1
horizontal cylinder	1(x-y)	2	1
dyke	2(z and x-y)	1	0
sill	2(x and y)	1	0
contact	3(x,y,z)	0	NA

The overall processing sequence for Euler deconvolution consists of the following steps:

- Preparation and gridding the potential field data with respect to sampling interval and line spacing,
- Applying of FFT and convolution grid enhancement,
- Processing to calculate derivatives,
- Analyze grids (Standard or Located Euler Deconvolution) for each structural index,
- Plot results,
- Repeat until acceptable.

The unusual aspect of using Euler Deconvolution is that one must have some initial estimate of the sources types in order to select a structural index. Accordingly, there is a need for additional information, for example from drill sites. In the case of the DML region, additional information comes from field geologists (structural geologist, J.Jacobs, University of Bergen), who has investigated DML in detail.

In regional interpretations, one is interested in identifying contacts and faults, so that an index of between 0 and 1 should be used. The maximum distance for acceptable solutions was set to 20 km, taking into account the average spectra analysis. The processing window size is 45 km, which is large enough to include variations within the data, but small enough not to include effects from multiple sources. As the deconvolution is a statistical process, with associated uncertainties, the maximum depth tolerance was set to 15 %.

The results are displayed in ordinary maps, combining the location and the depth solution. Additionally, the clustering of a given solution given the choice of an appropriate structural index, can be used as an interpretation tool. For example, a dyke structure would be displayed with a linear trend of solutions while vertical pipe would be shown as a point solution.

The results of the Standard Euler Deconvolution is displayed in the Appendix C. Due to the huge amount of information inside the Standard Euler Deconvolution, which includes uncertainties, which may be over-interpreted, the Located Euler Deconvolution was applied too.

The Located Euler Deconvolution uses the Analytic Signal to find and recognize peaks in the anomaly pattern, so that solutions are only estimated over recognized anomalies. After these peaks are localized, their locations are used for the deconvolution process. This process combines a window size that is varied according to the observed anomalies. Finally, the Located Euler Deconvolution produces far fewer solutions than the standard method, which are consequently simpler to handle.

In the interpretation chapter, the solutions of the Located Euler Deconvolution are displayed using the AS map with overlain depth solution.

Processing was realized with Geosoft Oasis montaj software, accordingly to Reid (1990) and Thompson (1982).

2.6.8 Isostasy

In order to study density variations within the upper crust, the thickness of the crust, mass distributions and isostatic adjustment have been computed. Important lithospheric units have been identified and the resulting structural information have been used in the interpretation of tectonic provinces. In view of isostasy, two classical and contrary conceptual models exist:

Pratt isostasy (Pratt, 1855): The density of the crust varies inversely with the height of the topography and the depth of compensation is at the base of the horizontal crust-mantle boundary. This model is generally accepted within the range of continental transition zones at passive continent-ocean boundaries.

Airy isostasy (Airy, 1855): The crustal density is constant beneath both the elevated topography and the level region. The roots extend beneath the elevated topography and the depth of compensation is at the base of the crust where the pressure is constant.

Both models assume the local reconciliation of the topographic loads and it is well known, that part of the loads is regionally compensated (see Barrell, Vening Meinesz, Gunn). The principle of regional compensation led to advancement of the iso-static models.

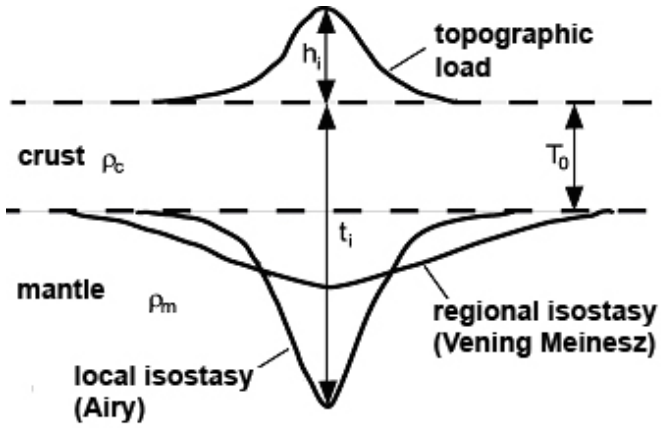

Figure 2.17: Isostasy: local isostasy (Airy) and regional isostasy (Vening Meinesz)

The computation of the Isostasy after Vening Meinesz (1939) is based on the principle of Airy's model. In addition, the model incorporates flexural rigidity of the lithosphere which partly supports the topographic load and takes into consideration the regional iso-static reconciliation. The regional compensation at the crust-mantle boundary can be considered as low-pass filter.

The calculation was realized using algorithm from Parker (1972) and Banks (1977). The following parameters have been used: crustal-density of 2670 kgm^{-3}, density contrast of 400 kgm^{-3} across the Moho accommodated the mass effects of the compensated terrain, with averaged crustal-thickness of 34 km.

Chapter 3

SURVEYS and DATABASE

3.1 Campaigns

The campaign/processing chapters will give a short summary of the main processing steps and the individual characteristics and similarities of the different datasets and campaigns. All calculations are done by the author, except the determination of the onset of the RES-data.

The extent of the survey areas, from 14°W to 20°E and from 70°S to 78.5°S, is large enough to fully recognize long wavelength regional anomalies. However, even smaller features could be mapped, owing to the average line spacing of about 10 km. The VISA project was subdivided into four austral-summer campaigns:

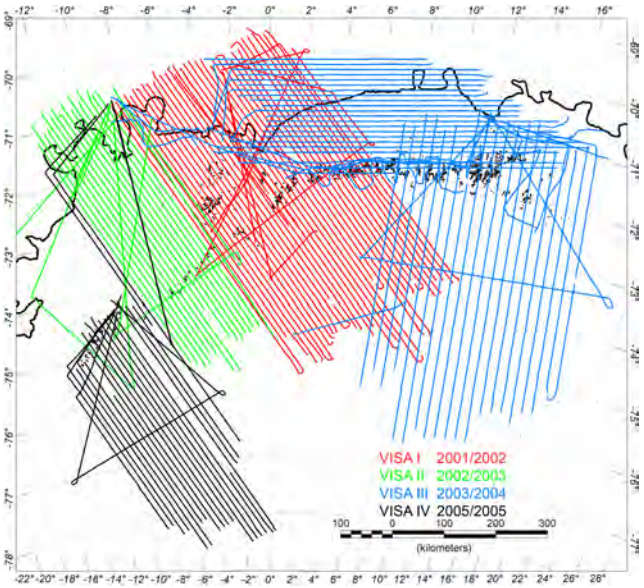

Figure 3.1: Overview of the study area and campaigns.

VISA I campaign
VISA I lasted from December 2001 to February 2002 and lasted 100 flight-hours during which 27700 profile km were flown. The survey area stretches from 4°W to 10°E and from 70°S to 75°S with Neumayer Station (Germany) and E-Base (South Africa) as operating base stations. A line spacing of 10 km was chosen. Three GPS reference stations were established at various locations in DML: Kohnen Station, Bleskamin Ice Rise and Soerasen. Additionally, magnetic base stations were established at E-Base, Kohnen and Neumayer Station.

VISA II campaign
The VISA II campaign (December 2002 to January 2003) amounted to 54.5 hours flying time, covering 13300 profile km. As gravity measurements do not allow frequent flight level changes, a level of 3960 m a.s.l. was adopted for most flights in view of the surface topography and cloud level. The spacing of the parallel profiles is 10 km. For post-processing two GPS reference stations were established, at Kohnen on Weigel Nunatak near Kottas Camp, and close by the Watzmann seismic array at Halvfarryggen. In addition, magnetic base stations were established at Kohnen and Kottas Camp. Furthermore, GPS data and magnetic data were collected at the geophysical observatory of Neumayer.

VISA III campaign
VISA III (December 2003 to February 2004) was completed with 133 hours of flying time and consists of 31150 profile km. The survey flights were carried out from Novolazarevskaya (Novo) runway and SANAE IV. While the profiles flown from Novo runway had a spacing of 20 km, a flight level around of 4000 m, and a north-south orientation (6°W to 20°W and 71.5°S to 76.5°S), the flights from SANAE IV had a spacing of 10 km and maximum flight level of 1500 m toward the north (1°W to 16°E and 70°S to 71.5°S). Four GPS reference stations were established at DML25, next to Kohnen, at Weigel Nunatak near Kottas Camp, FOR1 at Schirmacher Oasis and Novo Runway. A magnetic base station was set up at Novo Runway. Furthermore, GPS data and magnetic data were obtained at the geophysical observatories at Neumayer and SANAE IV.

VISA IV campaign
VISA IV flights were conducted in Western Dronning Maud Land with Neumayer and Kottas Camp as their main bases from December 2004 to January 2005. The survey area was located from 14°W to 0° and from 74°S to 78.5°S. The spacing of the parallel profiles was 10 km, with flight altitudes of 3200 m. GPS reference stations and magnetic base stations were established at Amundsenisen and Kottas Camp. Additional GPS and magnetic data were obtained from Neumayer Station and SANAE IV.

3.2 Airborne RES Data

The aim of processing RES data was to generate maps showing the ice surface and underlaying bedrock topographies. These are of crucial importance in understanding the geology, especially in the tectonic content. Several topographic models already exist, resulting from satellite investigations and small scale RES soundings, and are available from the international continent-scale BEDMAP database. Within the VISA project, the RES technique was used to generate a more local topographic model. Furthermore, in conjunction with airborne gravity data, these more highly detailed models are needed to calculate the Complete Bouguer Anomaly.

The input data sets are the kinematic GPS solution and the relative thicknesses of different media (air and ice) from the RES data. After merging these data by timecode we receive absolute values of surface and bedrock topography by simple subtraction from the well-known aircraft position.

The data are leveled using the tie lines as reference and archive blockshift fit. After this, the Kriging gridding routine was applied, with a cell spacing of 3 km. Ordinary Kriging is a geo-statistical interpolation method, which determines the interpolated values as a function of the distance to neighboring data points and the associated variance and relies on the spatial correlation structure to calculate the weighting values during interpolation.

The gridded ice surface topography data show a smooth surface without any noise or artifacts. Comparisons to other ice topographic datasets and models (i.e. ICESat; Bamber-model, 1997; BEDMAP-data) show that the results are good. Only in regions with strong gradients are misfits, of up to 400 m recognized after comparing VISA data to the older products (see Wesche, (submitted)). These large errors can be neglected, because each dataset is limited by its own errors. For example, BEDMAP data show strong differences along the coast lines (these data are mostly not direct measured but instead are digitized from other datasets), while ICESat data show differences at locations with strong gradients in topography, especially on the outcropping nunataks. Additionally, the ICESat data are limited due to cloud level conditions and this may result in differences of up to 50 m.

To level the ice topography data, it has to be taken into account that the electromagnetic waves of the RES have variable penetration depth with respect to snow and firn conditions. Ground GPS data are thus needed for ground truthing. These additional GPS data are provided along traverse profiles made using snow vehicles on their way to support the Kohnen Station or were done by static measurements at different camp sites within the field. Differences of up to 20 m in height between the GPS measurements and RES results are recognized, and the mean average correction was applied to the ice topography dataset.

With the exception of the VISA IV campaign which is purely continental, three topographic provinces can be recognized within each survey: The ice sheet, which has its origin in the hinterland and is continuously "fed", the mountain ranges with local nunataks and channelized ice flow, and the grounding line region which marks the transition from grounded ice sheets to floating ice shelves.

3.2.1 Topography VISA I

Ice Topography
(1) The coastal area is characterized by flat-lying ice shelves and sea ice with an average height of 40 m above sea level. This area flattens toward the north and is only disturbed where ice sheets and shelves are grounded, which yields in differences in topography of several tens to hundreds of meters at separated locations. These locations are well known, namely Soerasen and Halvfarryggen. Another interesting feature is the ice flow of the Jutulstraumen glacier, which is focused over a narrow sub-ice trough and widens out to join the sea ice over the shelf.

(2) From the continental coast line, a general increase in ice topography is recognized until the mountain range, especially in the eastern part. The western extension displays a more disturbed pattern due to the presence of mountain chains, which are separated into two linear and NNE striking lineaments, near the coast.

In the central part over the ice sheet, a smoothing effect of thick ice, without significant undulations, is recognized. Consequently, the sheet flows by following the subice topography.

(3) The hinterland is a more or less stable region, except for a central trough, with topographic heights starting ranging from 2000 m to 3400 m.
From the resulting ice-topography, the bedrock topography is calculated by simple subtraction of the ice thickness.

Bedrock Topography
(4) The offshore region, which is marked by the coastline (thick line) shows topographic features below grounded ice both at and below sea level. A pattern of troughs and basins is evident. Remarkable features are the Halvfarryggen, situated at the most north-western extent of the survey, and around E-Base, and the northern extension of the Jutulstraumen graben system, which is characterized by a trench-like lineament reaching toward the north. The exact topography north of the grounding line can not investigated with the RES technique as the ice-water interface beneath the floating ice shelves constitutes a barrier to further propagation of radar signals.

A continuous increase of bedrock topography can be recognized within a band of 50 km from sea level to the mountain range. Two thirds of this area is dominated by average elevations of 1000 m and more. Apart from this, strong segmentation due to tectonic processes is recognized.

(5) Deep-seated valleys and rift structures separate the mountainous subice topography, namely by the Jutulstraumen-Penksökket-Graben system. These, suggested to be parts of a failed rift system, are subdivided into three known parts and extend further toward the SE, beyond the edge of figure 3.2. The main branch trends NE-SW, reaching lowest topographic heights of 1500 m below sea level and ends at the shelve break. The real topography of this trench can not be traced further towards the north. A further trench, parallel to this is situated nearly 80 km towards the East. Both trenches continue in the more NE to SW oriented Penksökket graben (not shown on this map, but seen in the compilation chapter). The third trench strikes NS over a distance of more then 200 km.

The most southern extent of this survey displays a more or less stable region with average heights of 500 m above sea level, but is disturbed by EW and NE-SW trending highlands or mountain chains with average heights of 800 m, and intervening valleys which can reach depth of 200 m below sea level.

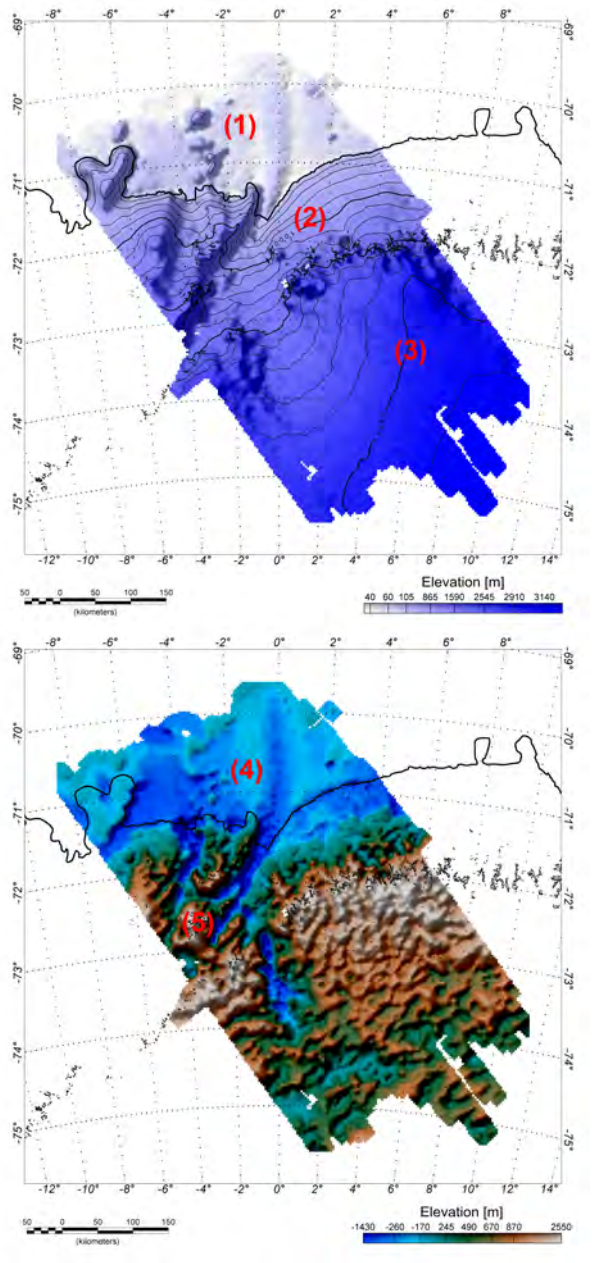

Figure 3.2: RES Results from the VISA I campaign. *top:* ice topography, overlain by 200 m contour interval, *bottom:* bedrock topography.

3.2.2 Topography VISA II

Ice Topography
(1) The northern area is characterized by the ice shelves, which display a smooth and flat surface structure, starting at 40 m a.s.l.. The Ekstroemisen bay is flanked by tongue-like topographic features, namely Halvfarryggen and Soerasen, striking towards the north. The grounded Halvfarryggen and Soerasen display heights of up to 700 m and 400 m a.s.l..

(2) A stable and continuous rise in ice topography toward the mountains in the south is recognized. Only the center-east region is characterized by stronger gradients, due to a spur of the mountains, which reaches the 2000 m level, toward the coast.

South of 73°S, the topography decreases slightly down to 1800 m over the Penksökket graben system, which strikes SW-NE beneath the ice sheet.

(3) Over the mountain chains, topography again reaches the 2000 m level. Several outcropping nunatak groups are visible. Further south, the topography becomes plateau-like at around 2800 m and more.

Bedrock Topography
(4) The sub-ice topography can be subdivided into four distinctive parts. The northern part combines both the shelf region, with a lowest depth of around 600 m below sea level and is divided by the Halvfarryggen and Soerasen. A SW-NE striking basin marks the boundary toward the continent.

(5) At 1000 m above sea level, the first prominent feature inland of the coastline toward the south is a massive block with an area of 22000 km^2 that strikes SW-NE. The SW-NE trending continuation of the Jutulstraumen-Penksökket graben system divides the area. The Penksökket graben itself is characterized by topographic depth of up to 500 m below sea level and increases up to 100 m a.s.l toward its eastern end. No direct continuation to the Jutulstraumen part is recognized due to the flank of a nearly 20 km-wide rock massif.

(6) The southern part is dominated by the SW-NE striking mountain range, with average heights of 2000 m and a width of 100 km.

The most southerly extension becomes less clear, with fragments of trenches and valleys, reaching down to 200 m below sea level, whose strikes vary wildly. Distinctive rock massifs 30 km in width are situated in the SE, reaching heights of around 400 m above sea level.

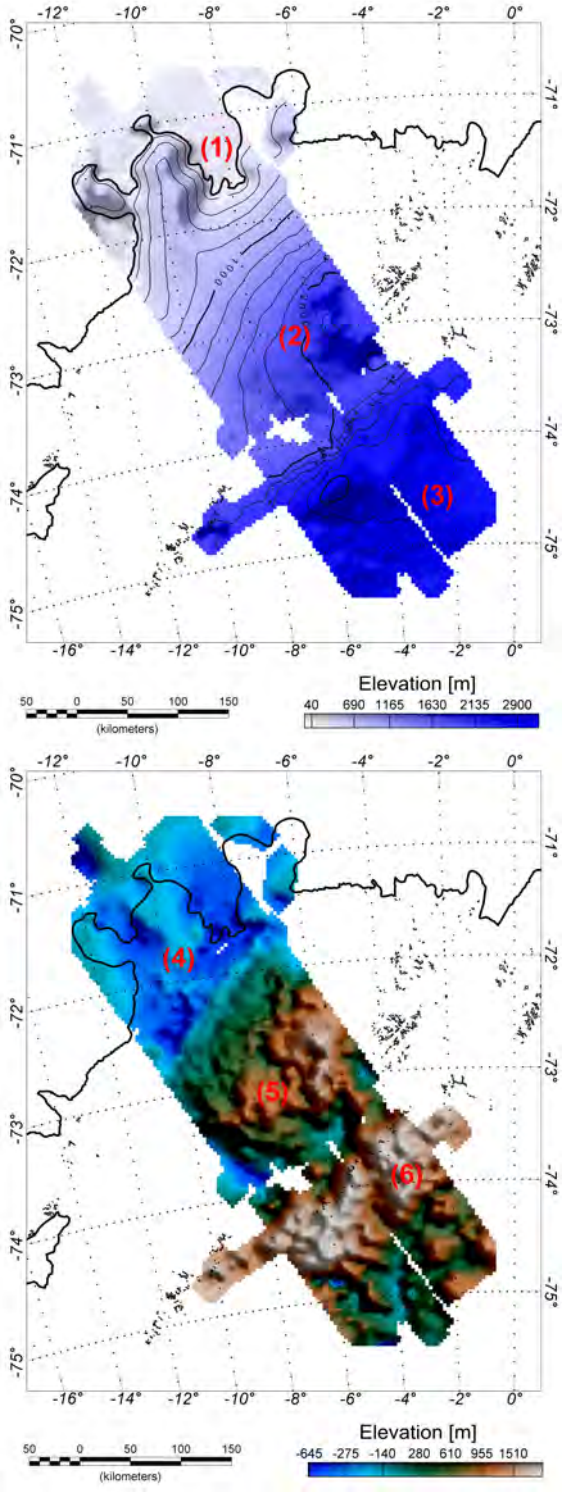

Figure 3.3: RES Results from the VISA II campaign. *top:* ice topography, overlain by 200 m contour interval, *bottom:* bedrock topography.

3.2.3 Topography VISA III

Ice Topography
The displayed topography can be divided into three parts. **(1)** The northern part consists of the ice shelf area with flat topographic behavior. Ice rises disturb the region, namely Vigridisen and Nivilisen, as do the north-trending pin points between 8-9°W.

(2) From the coastline southward, a more or less constant increase in height can be recognized until the mountain chains, with elevations around 2000 m. These mountainous regions strike E-W parallel to the coast. A wide band of nunataks is recognizable.

(3) From this linear feature, 50 to 100 km southward, the 3000 m contour marks the boundary to the south, a more stable region, very flat and plateau-like, tilted slightly upwards toward the SE. Maximum topographic heights reach the 3550 m level.

Bedrock Topography
The survey can also be divided into three major parts: the flat region, situated in the furthest north, the mountain chain in the center, and the hinterland plateau, which is internally segmented.

(4) The northern region contains the ocean transition zone with topographic heights below sea level. A well-defined basin structure extends over several hundreds of kilometers at mostly 500 m b.s.l.. This basin strikes EW, parallel to the coast. Several N-S orientated ridges reach north from the mountains, giving rise to a slight increase in topography over a width of 50 km or more. Apart from these trends, the area around the Russian base Novo and adjacent Schirmacher Oasis is characterized by a more E-W trend over an area of 2300 km^2, with elevations around 300 m.

(5) The mountainous region also trends E-W, parallel to the coastline, and is 130 km wide with maximum heights of more than 2500 m above sea level.

(6) South of the mountains, the 1000 m contour marks the boundary to the hinterland region, with maximum topographic heights between 500 and 1000 m a.s.l.. This area is characterized by prominent branches, segments, lineaments and basins up to 40 km wide and below sea level. These features display a rough and disturbed pattern without any preferred orientation.

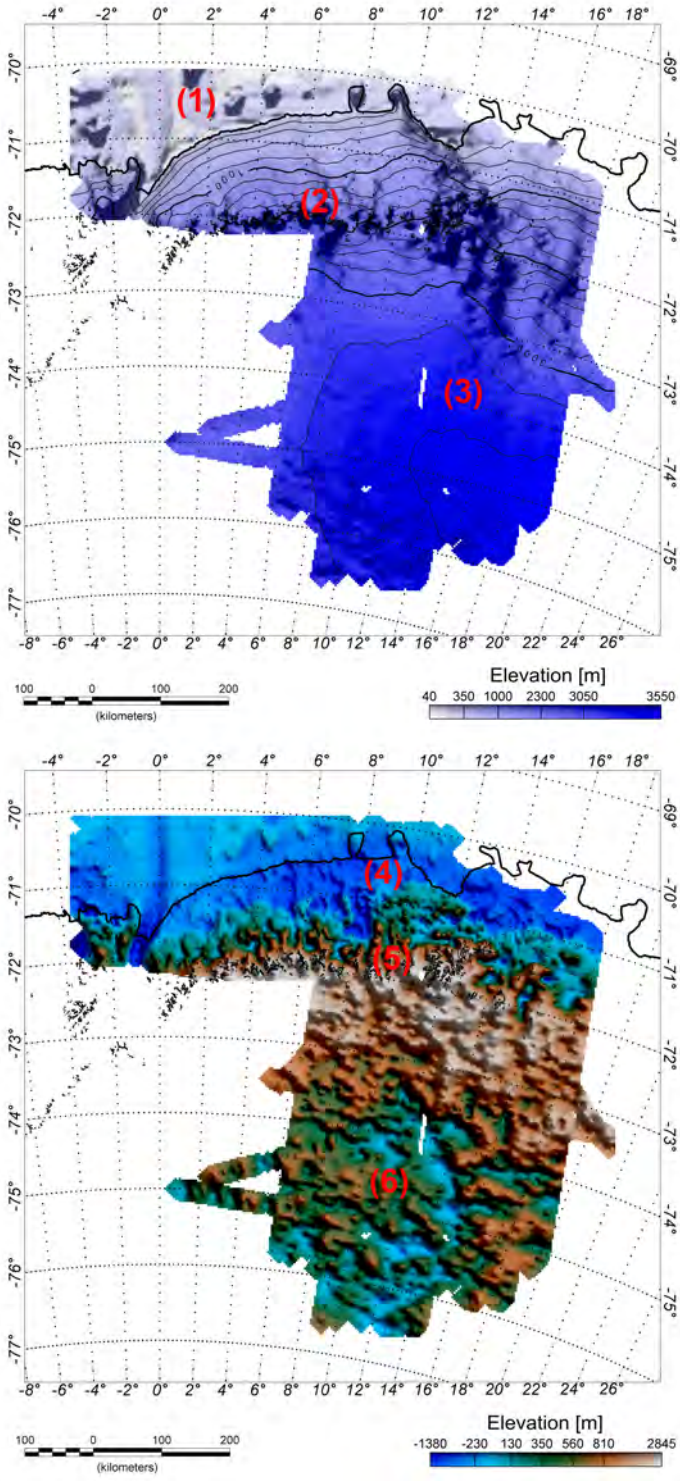

Figure 3.4: RES Results from the VISA III campaign. *top:* ice topography, overlain by 200 m contour interval, *bottom:* bedrock topography.

3.2.4 Topography VISA IV

Ice Topography
As the survey covered a purely continental area, the topography is monotonous and shows only minor signatures induced from bedrock and glacier movement.

(1) In the northernmost part, a SW-NE-trending mountain group is situated and marks a region with strong topographic gradients, climbing from 900 m a.s.l. to 2000 m over a distance of 30 km.

(2) Reaching the 2000 m level, where limited outcrops are situated, the hinterland topography becomes very stable again. A slight SW-NE trend can be recognized in elevation, which results in an average elevation of 2400 m above sea level in the further southeast.

Bedrock Topography
(3) The northern region is dominated by a small-deep valley, reaching down to 600 m b.s.l., flanked to the SE by the mountainous region with average heights of 2000 m. The strike direction is more or less SW-NE, but the upland displays several internal structures which are more N-S oriented.

A broad ridge trends SE from the mountains, and is flanked by basin structures 20 km wide and with depth down to 500 m b.s.l.. This feature marks the northern boundary of a huge basin structure that dominates the south of the survey area.

(4) The full basin is not covered by the survey, but the imaged area is more then 70400 km^2. This basin depth decreases gently to around 1000 m b.s.l.. Step sided circular features are recognized in the SE and SW corners, and reaching elevations of 500 m above sea level.

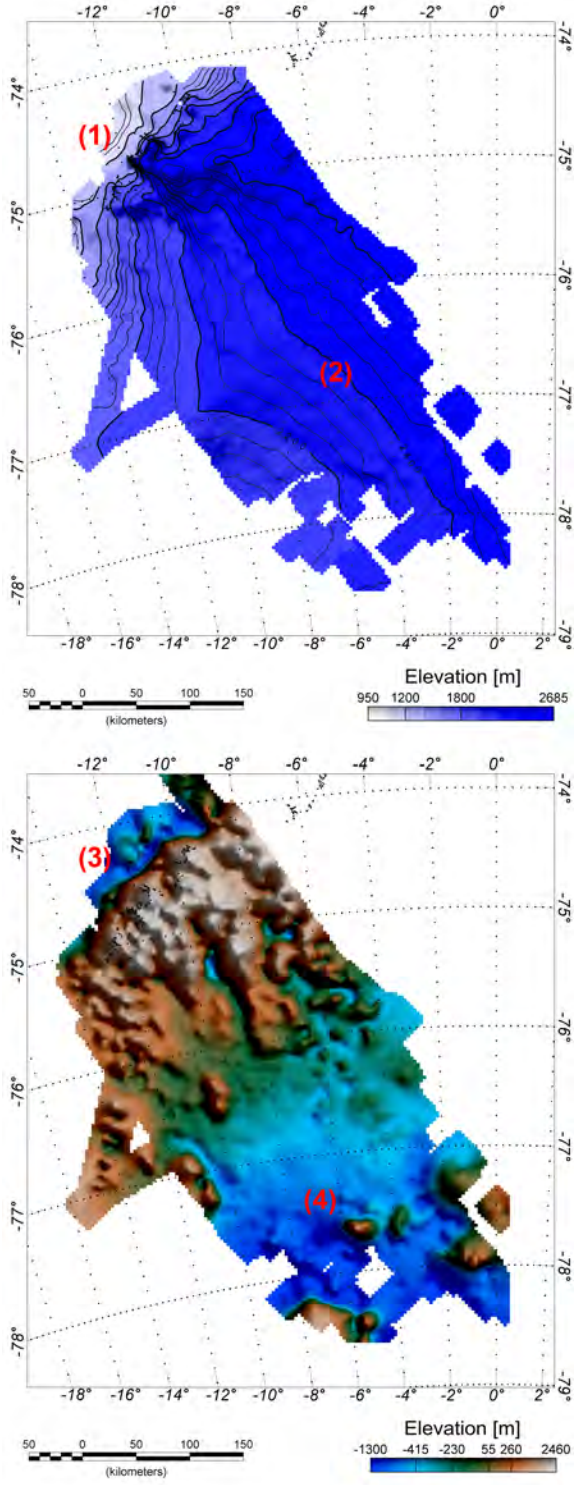

Figure 3.5: RES Results from the VISA IV campaign. *top:* ice topography, overlain by 200 m contour interval, *bottom:* bedrock topography.

3.3 Airborne Gravity Data

For accurate levelling of the airborne gravity data it is necessary to have precise knowledge of the absolute gravity at the airport and of its daily variation as well as the detection of drift and disturbance induced effects for the airborne measuring system.

To connect the local measurements to the absolute gravity net, a tie to the last absolute gravity reference point (South Africa) was made. This first crucial step must be done due to the relative absence of absolute gravity readings in Antarctica.

3.3.1 Free-air Anomaly VISA I

The tying process to the IGSN-71 net started in Cape Town, the nearest absolute gravity observatory point to the survey. At Cape Town, the following measurements were made at:

station	absolute gravity value [mGal]	measured relative gravity value [mGal]
Poller 94	979657.90	3159.52

The following gravity values were obtained for the three stations in Dronning Maud Land, Boreas/Passat-nunataks, Neumayer Station and E-Base:

station	absolute gravity value [mGal]	measured relative gravity value [mGal]
Boreas/Passat	982648.49	6150.11
Neumayer Station	982748.67	6250.28
E-Base	982723.41	6225.03

Gravity values at Neumayer Station and E-Base are used for the tie process, because these where the base stations. The quality of the calculated absolute gravity values are difficult to assess, because both stations are situated on the ice shelf, which is moving due to glaciological processes as well as influenced by tidal movement.

A second important step involves making daily base station readings, normally before and after flight, to compare the ground truth data with the airborne gravity meter. This will give a main level base value and detect sensor disturbances due to the sensor's mechanical system. Also, drift parameters are recognized and these are part of quality control. A table of base station, ground-truth and airborne-sensor readings is given in the Appendix B.

Summarizing the observed drift by base station and stage of operation- the sensor system was demounted during the campaign; the survey had a medium quality. The first part of the campaign, based on Neumayer, display a 3.5 mGal drift (9 days).

Based on E-Base, a drift of 6.7 mGal (17 days) is recognized and may have been influenced by a hard landing procedure. The last stage of the campaign, based on Neumayer station again, displays 0.7 mGal drift over 15 days. The real drift will decrease due to the influence of tidal movement of up to 0.5 m of the ice shelf, which is not recognized. The raw data indeed will highlight jumps in gravity readings and drift processes.

The levelling routine minimizes these uncertainties, but we have to bear in mind, that the application of levelling, although a numerical routine, is influenced by the operator's technique. Levelling was difficult due to the limited number of tie lines, so that every single line was levelled separately on different intersection points, meaning not even every tie line (1 full tie line and 2 half tie lines) was generally used as reference-level.

Other difficulties arise during the process of calculating the Free-air anomaly itself. Due to in flight-disturbances, or survey design limitations, changes in the flight path trajectory gave rise to additionally forces on the gravity meter's sensor. As a result it was necessary to separate each line due to the external disturbances and this results in a strong segmentation. The levelling (only zero order trend applied) minimized the intersection error to 4.4 mGal, with an standard deviation of 5.7 mGal.

The free-air gravity map is characterized by long wavelength anomalies that represent mostly deep-seated crustal structures. As expected, there is a strong correlation between free-air gravity and sub-ice elevation.

A prominent SW to NE trending gravity low can be interpreted as the expression of the Jutulstraumen-Penksökket graben system **(2)**. The measured values on this sharply defined gravity low is -113 mGal, which is the most negative gravity anomaly in this survey.

Positive gravity anomalies are situated over the flanks of the Jutulstraumen rift system and the sub-ice mountain range, mostly induced due to the topography. These long wavelength anomalies reach a maximum of 170 mGal.
A gravity low orientated parallel to and NW of the Jutulstraumen terminates at an E-W orientated gravity anomaly low **(1)**. Orientated along the coast this long wavelength and gravity anomaly low is interpreted as a basin structure near the transition zone between ocean and continent. Further north, positive high-amplitude gravity anomalies with average values of 100 mGal represent seaward dipping reflectors and a shallow crust-mantle boundary (Jokat et al., 2003, 2004).

A NW-SE trending low branches off from the center of the Jutulstraumen rift system and continues well to the south, although here it is much broader with a minimum value of -80 mGal **(3)**.

Influenced by strong gradients in topography the free-air anomaly displays a disturbed pattern with extreme values ranging from 170 mgal down to -110 mGal.

Comparison with the detailed BAS survey from 2001, situated in the center of the area around Jutulstraumen, published by Ferracioli et al., (2005), shows no significant differences.

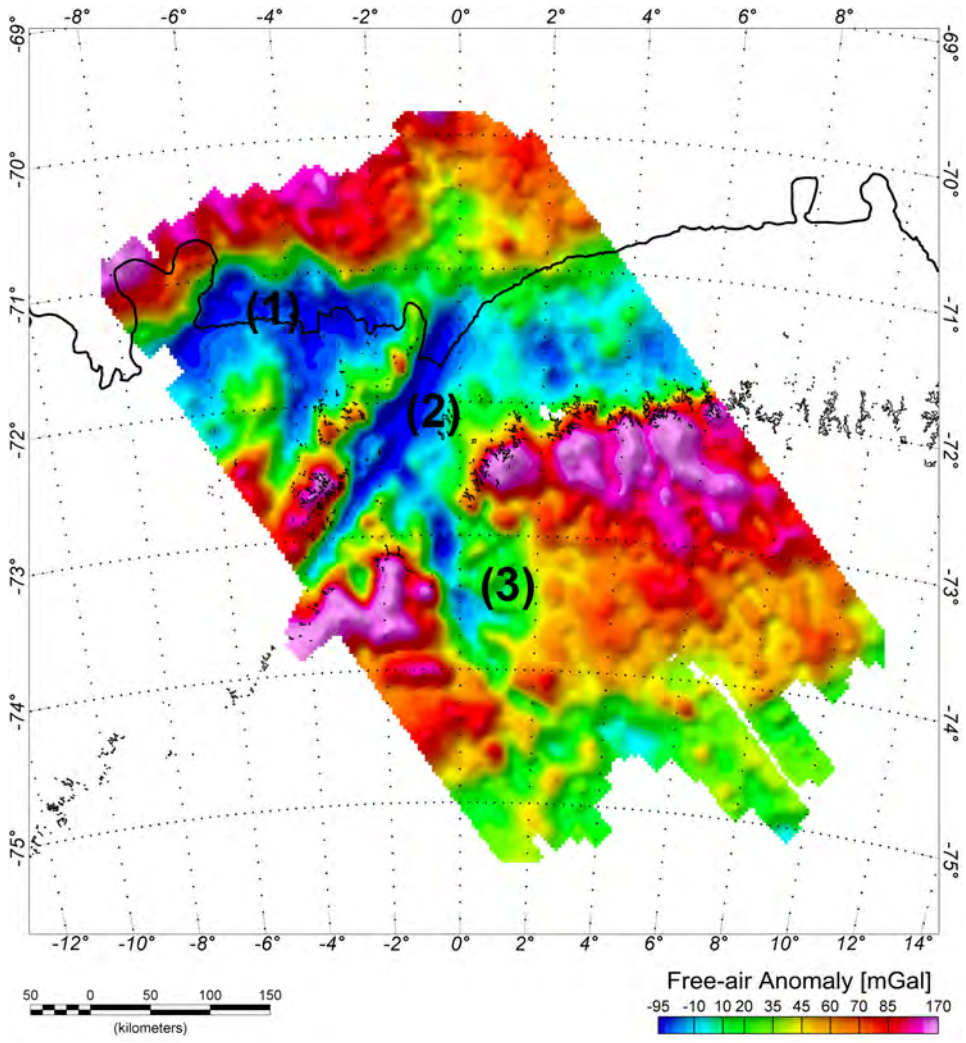

Figure 3.6: Free-air anomaly of VISA I campaign.

3.3.2 Free-air Anomaly VISA II

The tying process was less accurate due to the absence of any gravity reading at a known station in the IGSN 71 net before surveying. The only way of using the investigated survey data was the use of a dummy value from the year before readings as well as the post survey tying process. This, of course, involves questionable assumptions, but there are no other information available.

Using this "virtual" Cape Town station with readings of 3159.50 mGal (relative), 979657.90 mGal (absolute) with the single reading at Neumayer Station yields the following absolute gravity value for the VISA II campaign:

station	absolute gravity value [mGal]	measured relative gravity value [mGal]
Neumayer Station	982738.83	6240.42

In fact, it is not possible to make any statement about the quality of gravity measurements. Long term experience, combined with the knowledge of gravity measurements of the upcoming seasons (2003/2004) makes these reading/calculations repeatable. A yearly drift of 10 mGal for the Neumayer station seems likely in view of the slow movement of the ice shelf by nearly 160 m per year.

Summarizing, the drift of 3.9 mGal over 16 days for the aero-gravimeter during surveying and the tying uncertainties together mean that the survey has bad input quality, but is internally very stable.

The levelling (only zero order trend applied) minimized the intersection error to 3.6 mGal, with an standard deviation of 3.9 mGal.

The strong correlations with sub-ice topography are clearly recognized within the free-air anomaly map. Compared to the topography, the free-air anomaly is much smoother and is mainly influenced by the masses of rock material above the reference as well as separates due to deep-seated crustal structures. This is especially seen in the most northern part, where positive long wavelength anomalies with values up to 150 mGal, can be interpreted as seaward dipping basalt flows, in conjunction with reduced crustal thickness in the continent-ocean transition zone **(1)**.

A prominent gravity low, with measured values of -100 mGal, trends SW-NE, with a wavelength of 80 km and characterizes the boundary to the massive SW-NE trending mountainous region **(2)** seen in the sub-ice topography, whose gravity reaches 100 mGal. The southern region is divided by the Penksökket graben, which displays a gravity low with values of -50 to 10 mGal.

The E-W trending mountain range **(3)** is characterized by a chain of positive gravity anomalies, 80 km wide, with partially high amplitudes of 170 mGal and a wavelength along the chain of 50 km. Two additional features are recognized from the main mountain chain, which strikes mostly parallel to the coastline. In the south-eastern and the south-western parts, the free-air anomaly field is characterized by isolated anomalies, divided by a distinctive 20 km wide low of 0 mGal. Summarizing this,

the free-air anomaly displays a more or less undisturbed pattern with respect to the topographic behavior.

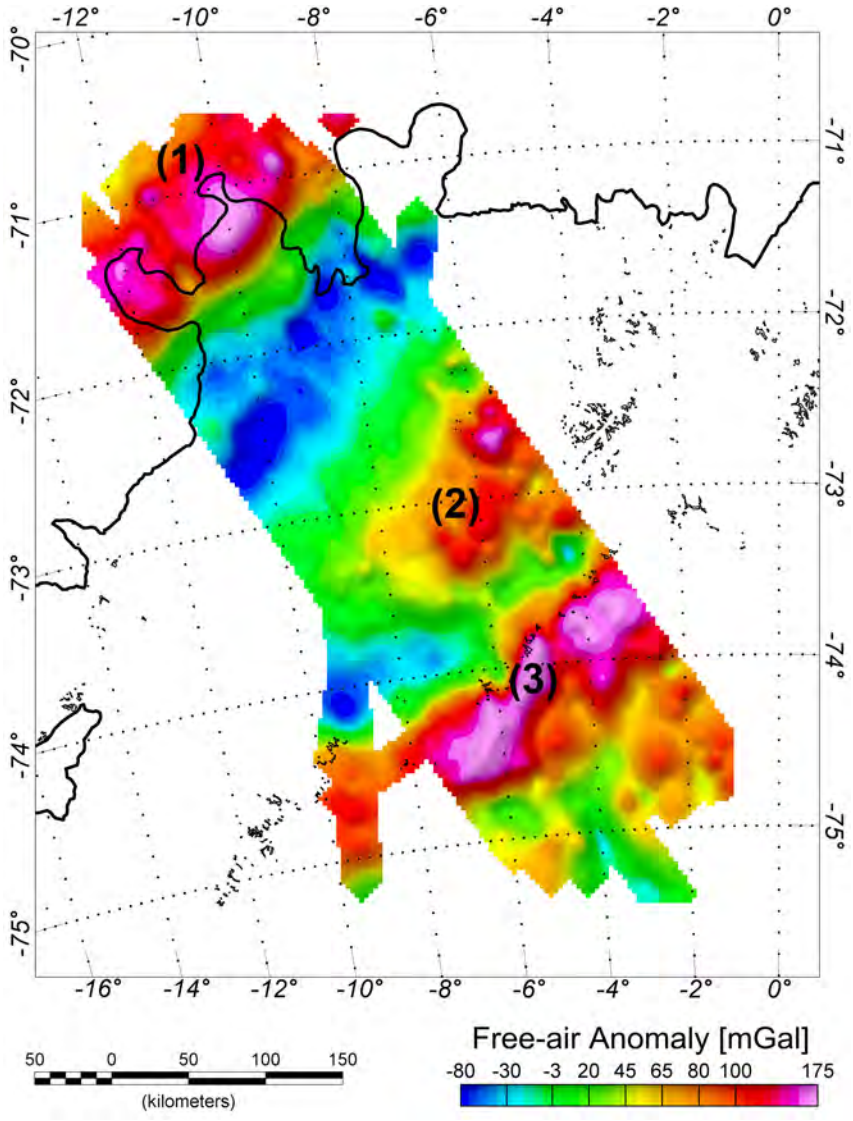

Figure 3.7: Free-air anomaly of VISA II campaign.

3.3.3 Free-air Anomaly VISA III

The procedure for tying the local gravity measurements to the IGSN 71 network was difficult because no gravity measurements were made before survey. Only the post survey reading at Cape Town (South Africa) was used as a real measured value for this purpose. Under the assumption that no disturbing effect was encountered during the survey, the following measurements and calculations are used:

station	absolute gravity value [mGal]	measured relativ gravity value [mGal]
Cape Town (UTC)	979616.80	3254.19
Novo (airfield)	982467.58	6104.98
Sanae (airfield)	982457.72	6095.12

During this austral summer campaign, an absolute gravity measuring project carried out by J. Mäkinen. His absolute values, also measured at the Novo airfield and Sanae station, much later confirmed our tying process within an accuracy of 1.0 mGal.

The drift process is referred to the airborne gravimeter, with the corresponding base stations displaying normal sensor operations. A drift of 4.28 mGal over 9 days at Novo might be quite high, but is within the acceptable range. The observed drift at Sanae station, of 0.2 mGal over 4 days, displays normal operation.

The levelling (only zero order trend applied) minimized the intersection error to 5.5 mGal, with an standard deviation of 6.9 mGal.

With respect to the survey and topographic behavior, the interpretation of the free-air anomaly can be made with reference to four different areas.

The northern extent, flown with E-W profiles, displays the continent-ocean transition. Strong field gradients are recognized, beginning from 150 mGal offshore and dominantly striking parallel to the coast. As elsewhere, these can be interpreted as structures and seaward dipping basalt flow sequences **(1)**.

The positive anomalies are followed inland by an extensive gravitational low. This -100 mGal low dominates the foreland of more than 400 km E-W and 150 km N-S extent. There is a good correlation with the bedrock topography, which displays a basin structure **(2)**.

The central part of the survey is dominated by the mountain region, with values of around 150 mGal. Apart from the bedrock topography, segmentation in N-S direction disturb this mostly homogeneous part of the field **(3)**.

The southern reaches show a smooth field, with levels of about -20 to 20 mGal and corresponding to topographic features, which are characterized by individual segmentation **(4)**.

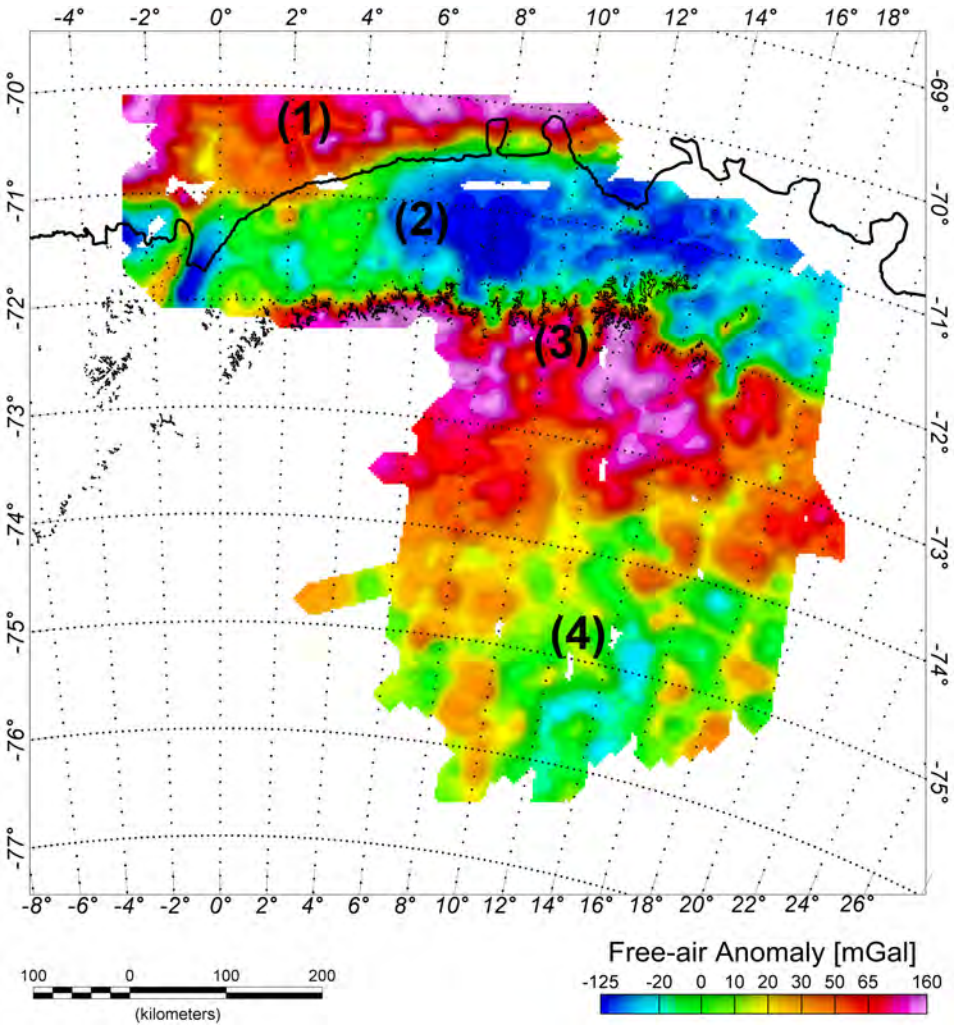

Figure 3.8: Free-air anomaly of the VISA III campaign.

3.3.4 Free-air Anomaly VISA IV

The tie process to connect the local gravity measurements to the IGSN 71 network was realized by colleagues of TU-Dresden, who undertook local GPS measurements within the field campaign. As reference station in the IGSN 71 network, they used the South African UCT NEW station, situated at Cape Town University.

station	absolute gravity value [mGal]	measured relative gravity value [mGal]
Neumayer (construction)	982733.48	6372.29
Neumayer (airfield)	982729.61	6368.43
Kottas (campsite)	982311.87	-
Kottas (airfield)	982310.57	-

The observed airborne gravity sensor drift of 2.9 mGal over 11 days is consistent with normal operation during the campaign.

The levelling (only zero order trend applied) minimized the intersection error to 3.8 mGal, with an standard deviation of 4.3 mGal.

Compared to the bedrock topography, the map shows a much smoother field. The influencing changes in topography, with a dominant N-S trend, are clearly recognized.

The most northerly extent is characterized by a gravitational low, while the mountain range itself displays high positive values of around 150 mGal, and trending SW-NE **(1)**. Within this anomaly complex, local E-W and N-S trends are recognizable. A smooth change in free-air anomaly to a level of 20 mGal describes the mountainous hinterland region, with N-S trends.

Further south, values of around 0 mGal are measured, trending SW-NE. The most southern area is dominated by a gravitational low of down to -80 mGal, striking E-W, with a N-S striking branch in the furthest southeast **(2)**. This pattern is disturbed by small-scale and local positive anomalies of 40 mGal, which are entirely contained within the survey.

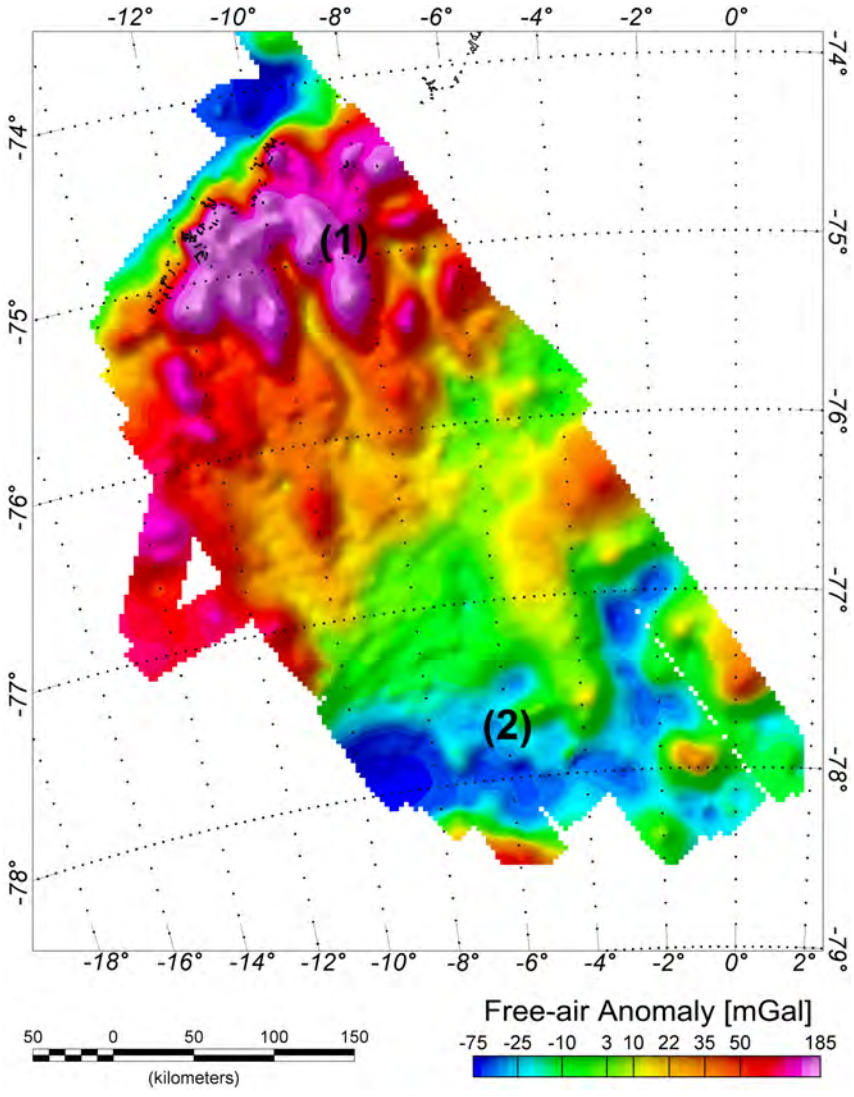

Figure 3.9: Free-air anomaly of the VISA IV campaign.

3.4 Airborne Magnetic Data

A sequence of processes, see section Aeromagnetic, is applied to produce maps of the TMI. The quality of the resulting map depends on the quality of the dataset and on the use of different, operator based (subjective) techniques. Manual editing will remove disturbances or spikes of noise induced by current flow inside the aircraft. The correction for diurnal effects is mainly based on the ground recording sample interval and distance between the magnetic base station and the area of operation.

3.4.1 TMI VISA I

Problems with magnetic base station recordings (malfunction results in recording stop) resulted in strong segmentation of these datasets. To close existing base station data gaps during flight times, magnetic data from the Neumayer Station are also used to correct for diurnal variations. This involves on the other hand long baselines of up to 700 km, which may result in a phase shift of the base station record. Other problems occur due to strong daily variations in the magnetic field, and especially influence the tie lines and night time flights.

Due to limited number of tie lines in the origin flight level, it was necessary to use profiles from draped flown previous campaigns for levelling after upward continuation. Following continuation to a common datum, at 3500 m a.s.l., the errors at intersection points are reduced to 5.1 nT after levelling, with a standard deviation of 4.7 nT.

The map shows strong variations in magnetic intensity, suggesting a wide variety of different magnetic properties. The survey marks a boundary between magnetic provinces, and probably also includes several magnetic subunits.

E-W striking magnetic anomalies mark the northern extent of this survey **(1)**. With high amplitudes of up to 150 nT, these coast-parallel anomalies can be related to seaward dipping basalt layers [Jokat et al., 2003, 2004]. A magnetic low, with amplitudes of -200 nT, is recognized parallel to the south of these anomalies, and can also be related to these basalts.

Further southeast lies a prominent band of positive magnetic anomalies **(2)**, with wavelengths of up to 30 km, striking SW-NE. These anomalies peak with amplitudes of 1200 nT, with an average of around 170-300 nT. This feature can be interpreted as the border between two magnetic units.

To the north-west **(3)**, past a subdued magnetic low of around -150 nT, the Jutulstraumen rift is characterized by positive anomalies that are more isolated, and separated from one another at moderate wavelengths of 5-30 km with intensities of 100 nT.

The central and eastern region is dominated by singular high amplitude anomalies of limited extent, with 5-10 km wavelength, flanked by a magnetic low of -150 nT. The maximum amplitudes of these anomalies can reach values of 400 nT.

Eastward of the SW-NE striking anomaly complex, individual spot-like anomalies

(4) are recognized, which are high in amplitude (200 nT) and of limited extent up to 25 km. These are aligned along the SW-NE direction, and can be interpreted as forming over intrusive igneous bodies.

The southern region of the survey is characterized by a more parallel orientated ensemble of magnetic anomalies **(5)**, striking WSW-ENE, consisting of well separated anomalies with wavelengths of 10 km and intensities of 200 nT. Further south, the magnetic pattern becomes less organized, with amplitudes up to 50 nT.

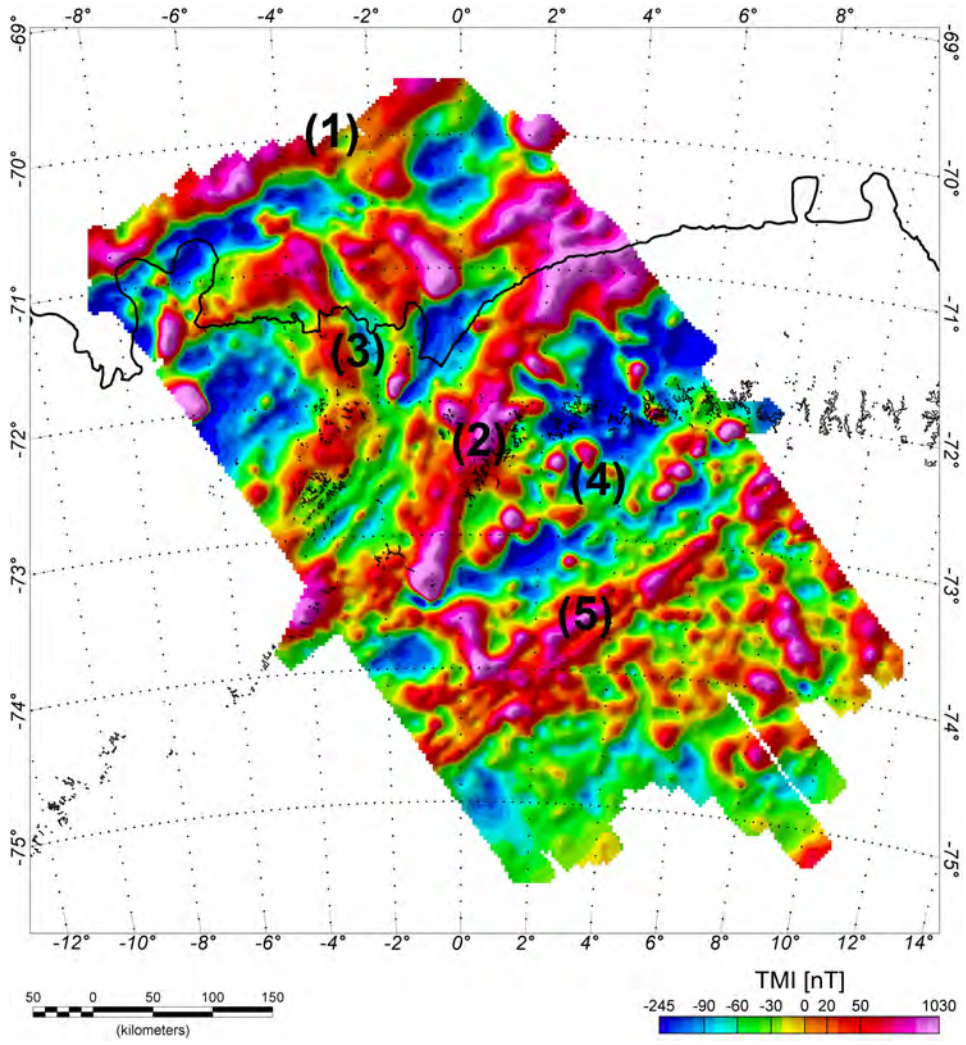

Figure 3.10: Total Magnetic Intensity map of VISA I campaign.

3.4.2 TMI VISA II

The data quality can be described as good to excellent. The analyzed ground-truth base station recordings display normal diurnal variations and these datasets, recorded at Neumayer Station and Kohnen Station, could be used without any problems. Base lengths, depending on base stations, are moderate, with maximum distances of around 300 km.

Levelling was undertaken after continuing the data to a common datum, at 3900 m a.s.l., using a statistical block-shift method, which yields a mean error at intersection points of 7.3 nT with a standard deviation of 5.9 nT.

The resultant TMI-map shows a more or less quiet area with short wavelength anomalies, separated only by a few discrete point-like and linear anomalies in the north of the surveyed area. These linear features occur within the continent-ocean transition zone, strike E-W and parallel to the coast and are more then 100 km in length, with wavelengths of 25 km and amplitudes of 300 nT **(1)**.

A distinctive low of -250 nT, also E-W striking, lies to the south.

A positive anomaly complex, 175 km long, with a discrete boundary of 20 km in wavelength and amplitudes of 170 nT, is situated further south. Two discrete elliptical anomalies are situated on the eastern flanks, each 40 km in length and 18 km wide, with amplitudes of 220 nT **(2)**.

Further south, in the central part of the survey an extensive low amplitude low with values around -70 nT is situated **(3)**. Short wavelength anomalies are recognized, superimposed on this feature. Single circular spot anomalies, as well as bands of lineaments up to 12 km in wavelength, and with intensities of 100 nT mark a change in the magnetic pattern.

The most prominent anomaly in this area is the Penksökket Anomaly **(4)**, which strikes E-W and is more then 200 km in length, with maximum amplitudes of 230-330 nT.

A magnetic anomaly low parallel to and south of the Penksökket Anomaly forms a discrete boundary to two distinctive lows with -200 to -400 nT, which are followed by two elongate anomalies, nearly 50 km in extent and up to 20 km in wavelength with intensity of 150 nT. The anomalies show different strike directions, E-W and SW-NE, and are surrounded by discrete and short wavelength anomalies on their flanks **(5)**.

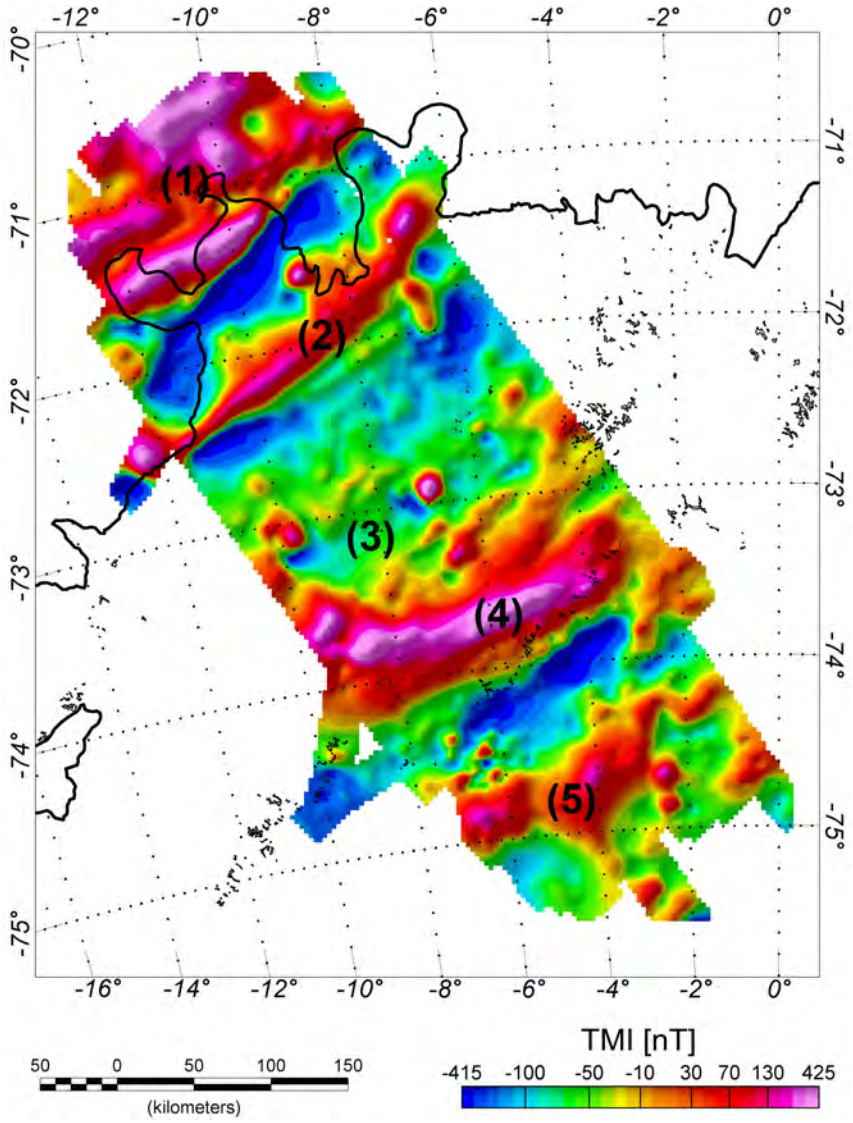

Figure 3.11: Total Magnetic Intensity map of VISA II campaign.

3.4.3 TMI VISA III

The survey had to be divided into two operative parts, see below, each of which required a different data processing sequence. The N-S flight lines, with a spacing of 20 km had their operational base station at Novolasarewskaja and the second, the W-E orientated flight pattern with 10 km spacing was flown from Sanae station.

Data handling, especially removing diurnal variations, levelling to a common datum and the statistical levelling process, was influenced by the operator and strongly subjective, due to:

- strongly spiked base station recordings at Novo station,
- long baseline induced phase shift of diurnal variations (Sanae station as magnetic base station),
- different flight altitudes,
- the absence of any tie lines for the E-W orientated flights.

For the N-S pattern, the magnetic base station recordings at Novo are strongly influenced by disruptive cultural noise. Despiking of the dataset shows partially useful solutions (time windows), but unfortunately not for all flights. Transformation to a common flight datum failed for levels between 3500 and 4600 m. This means a common datum (upward continued) might be around 4600 m, which results in a significant loss of information. A trial downward continuation to 3800 m displays data which are strongly influenced by filtering. Comparison of the different solutions (upward, downward, without) led finally to the decision to level the line-data individually, for their best solution, and not to attempt any transformation to any the common datum for the whole campaign.

The E-W-pattern was flown at heights of between 800 to 3500 m. This survey was levelled to a common datum at 3500 m. The use of magnetic base station data from Sanae station, situated up to 650 km distant resulted in a phase shift of borderline usefulness, but shows good primary results due to the absence of any other ground-truth data as well as the nonexistent tie lines for levelling.

The first attempt to level the data used the intersection points with the VISA I dataset at the most western extent of VISA III. This yielded a bad solution, as only the most western part (i.e. 1/5 of the complete flight line length) was levelled under control, while the most important parts of the profiles are "free" of any levelling control, which result in uncontrolled shifts in intensities.

Consequently a new levelling strategy was developed, to make the dataset viable. This strategy takes the following steps:

- use of the VISA I campaign data in the furthest east and level base
- use of the GEOMAUD data (BGR Hannover) in the furthest northwest as second data base

- different trials of forward-backward levelling-procedures (statistical, individual, automatic) to combine these two datasets with the VISA III data.

Finally, the displayed TMI map shows, except in the most south-eastern part (marked with **(x)**), good results from this individual levelling procedure. In the marked area, the influences of the different base levels of the flight lines are visible at around 73.5°S. Direct conclusions about the internal quality with respect to the error at intersection points are not useful, but can be given at 15.3 nT with a standard deviation of 12.1 nT.

This most eastern region of the investigated parts of DML shows, except for the continent-ocean transition zone, low amplitudes and short wavelength anomalies with little or no continuity.

The most northern part of the survey, over the continent-ocean transition, is characterized by strong coast parallel orientated anomalies **(1)**, with high amplitudes between 200 and 480 nT and wavelengths of up to 25 km.

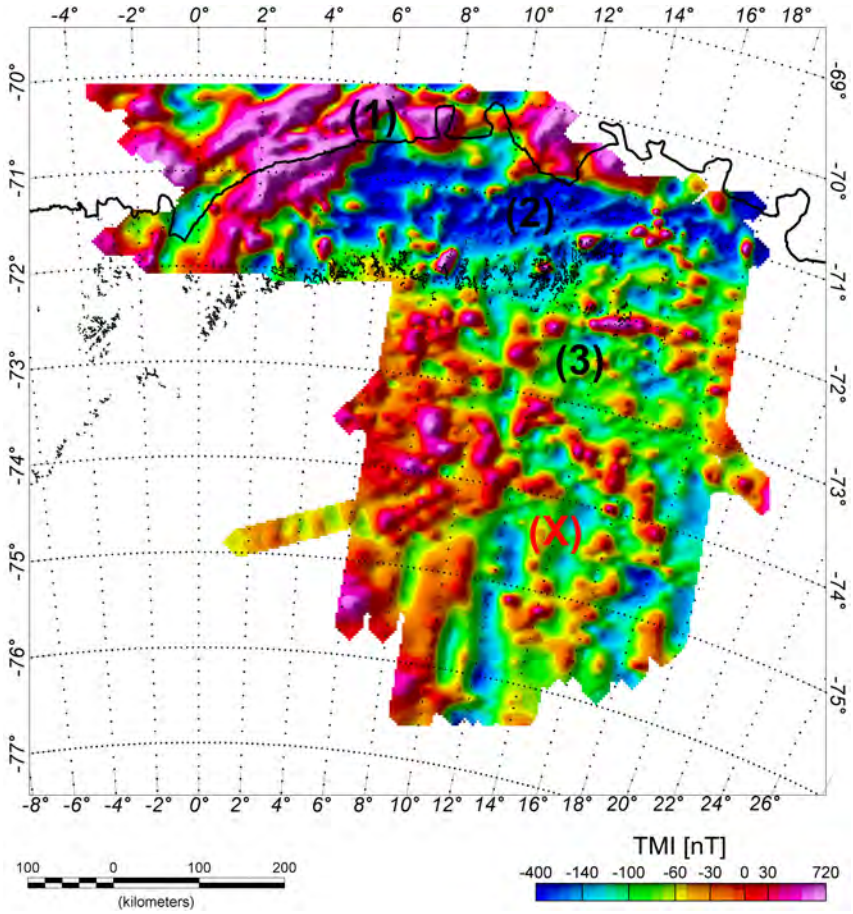

Figure 3.12: Total Magnetic Intensity map of VISA III campaign.

An extensive low **(2)**, of averaging -250 nT, is displayed between the coast and the mountain chains. Small changes in intensity occur with this low. These well located anomalies disturb a magnetically quiet area over a region of nearly 50000 km^2.

South of the mountain chains (i.e. Wohlthat-Massive), the magnetic structure displays several anomalies and can be described as irregular, with short wavelength variations of hundreds of nT **(3)**. E-W and possible NW-SE trends can be interpreted but, due to the campaign uncertainties, it would be inappropriate to interpret the southern area in more detail.

3.4.4 TMI VISA IV

The quality of the airborne based data can be defined as good. No significant additional noise was observed during the flights. Recordings of the diurnal variations were problematic when it came to the correction of three flight lines. Additional ground truth data from Neumayer Station, Sanae or Kohnen could not fix the problem. Consequently, two flights were unsuitable for levelling and do not contribute to the gridded data. The levelling (only zero order trend applied) minimized the intersection error to 7.5 nT, with an standard deviation of 6.6 nT.

Two magnetic trends are visible in this map: an E-W and a N-S segmentation.
The northern part, where the SW-NE trending mountain chain group is situated, is dominated by a magnetic low of -200 nT, which separates into east-west and south-east trending branches **(1)**. The branches are flanked by magnetic highs of several hundreds of nT.

Beginning at 75° S the magnetic field adopts a background level of around -50 nT, with long wavelengths. Positive, around 100-150 nT anomalies, 40 km in length and striking SW-NE, with wavelengths of 15 km are superimposed on this field. A sharp boundary to the west is recognized **(2)**.

Southward, the dominant strike direction changes more to SW-NE, in an area that is separated from the northern part by a magnetic low of -250 nT, followed by 110 km in long and 35 km wide positive anomaly complex with amplitudes of 300 nT **(3)**.

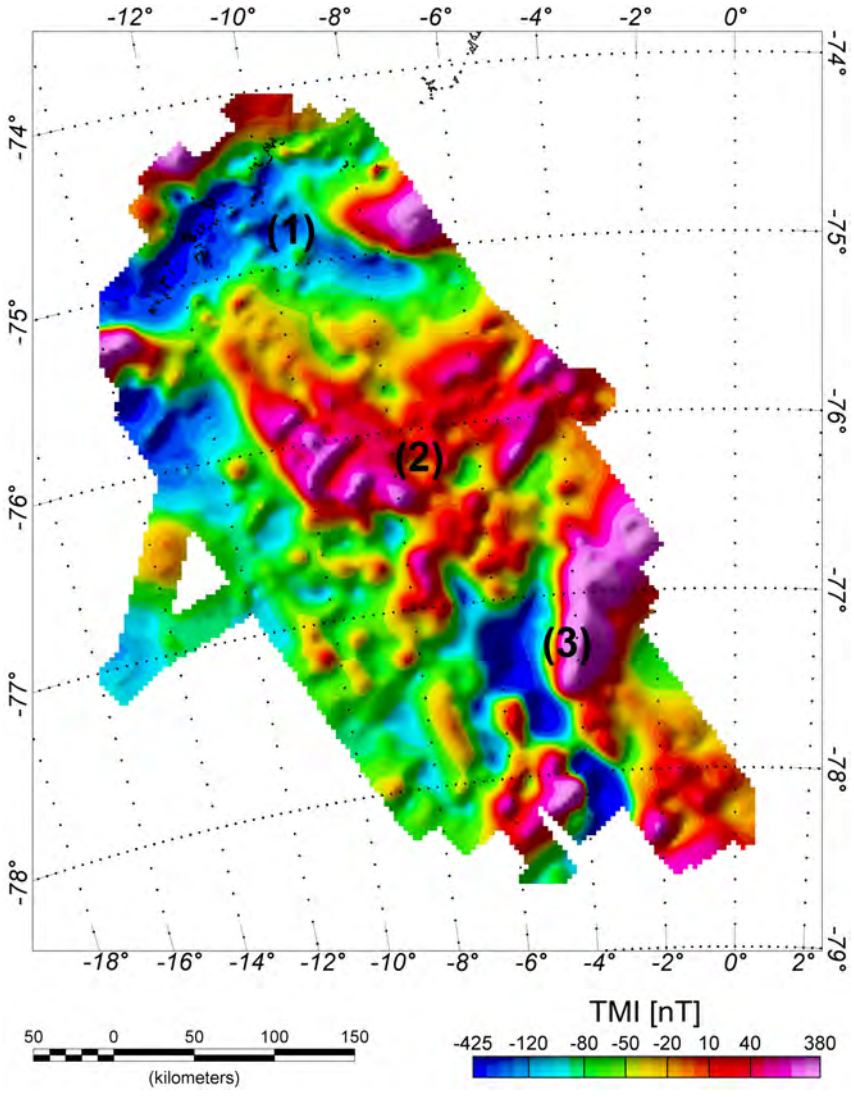

Figure 3.13: Total Magnetic Intensity map of VISA IV campaign.

3.5 Advices for future airborne operations

The investigations within the VISA project, which took place between 2001 and 2005 are combined here with a deeper understanding of the acquisition of potential field data in general as well as of solving detailed problems within data handling. This is some advice for future investigations; partially this material has been covered.

Gravity: It is essential to improve the quality of the absolute gravity estimation as a fundamental part of gravity investigations. This requires the correct estimation of a base value within the area of investigation as well as the verification of the airborne gravity sensor.
Furthermore, daily repeat readings at the base station before and after surveying is essential for the same task of quality control.
Twenty four hour heating of the gravity sensor ensures its stable operation and reduces the burden of pre-flight procedures on the operator.
For survey planning and acquisition, it is essential not to fly on pre-defined waypoints, because every correction of the flight trajectory during the flight causes in additional accelerations, which work on the gravity sensor and must be balanced within the system, leading to data gaps being introduced during the levelling procedure.

Magnetics: A correctly operating airborne environment is not the only essential prerequisite for the success of magnetic investigations. The measured data are mainly influenced by the later reduction techniques, for example the correction of daily variations of magnetic field activities. This requires the perfect completion of the base station recordings as well as their location with respect to the airborne component.

Generally: The levelling process is the essential tool to improve data quality. This is realized with the use of tie-lines, which must be flown in a rectangular pattern and with an approximate ratio of lines to tie-lines of 5:1. To ensure the highest quality of tie-lines (important, because these define the base level of the data) it would be advantageous to check the space weather forecast in advance. This can be easily done via internet access or satellite telephone, which is always available within the field. Investigations during night times are of no use due the mostly strong magnetic background activity. A detailed quality and quantity check of the measured data after each flight would be useful. An update of common processing software is strongly recommended.

Chapter 4

COMPILATION and INTERPRETATION

In the following chapter, the compilation of each dataset from the four parts of VISA, measured from 2001 until 2005 is described. Apart from these, and with respect to the huge extent of the surveyed area, different regions are displayed in more detail.

4.1 Topography

After merging the data into one common database, a systematic adjustment procedure was used to reduce the crossover errors between the different campaigns. The individual lines were adjusted by a first order polynomial fit, which reaches in a mean error of 2.5 m and a standard deviation of 2.4 m for the ice-topography. The bedrock-topography displays, due to stronger gradients and uncertainties, a mean error of 15.2 m, with an standard deviation of 11.1 m after levelling procedure.

The topographic features can be subdivided into three distinctive regions.
The most northern extent is dominated by the ice shelf region, which is more or less flat, with average height of 40 m above sea level. The seaward flow of ice streams dominates the topography and is also influenced by irregularities in the bedrock topography. A dominating feature is the tongue of the Jutulstraumen, which is up to 40 m higher then the surrounding ice of the Fimbul Ice Shelf. Other topographic features arise from bedrock topography, like ice rises (contact of ice with bedrock topography in the ice shelf region) and the Soerasen and Halvfarryggen.

The second remarkable area is the foreland of the mountain chains, which marks the mechanical and natural boundary of the ice. Here, from sea level to 2000 m above it, topographic changes with an average gradient of 2 mkm^{-1} are recognized. This area too is dominated by the Jutulstraumen, which follows a geologic trough that is of structural origin: here the ice sheet drains through the mountain range. This system can be subdivided into two branches.

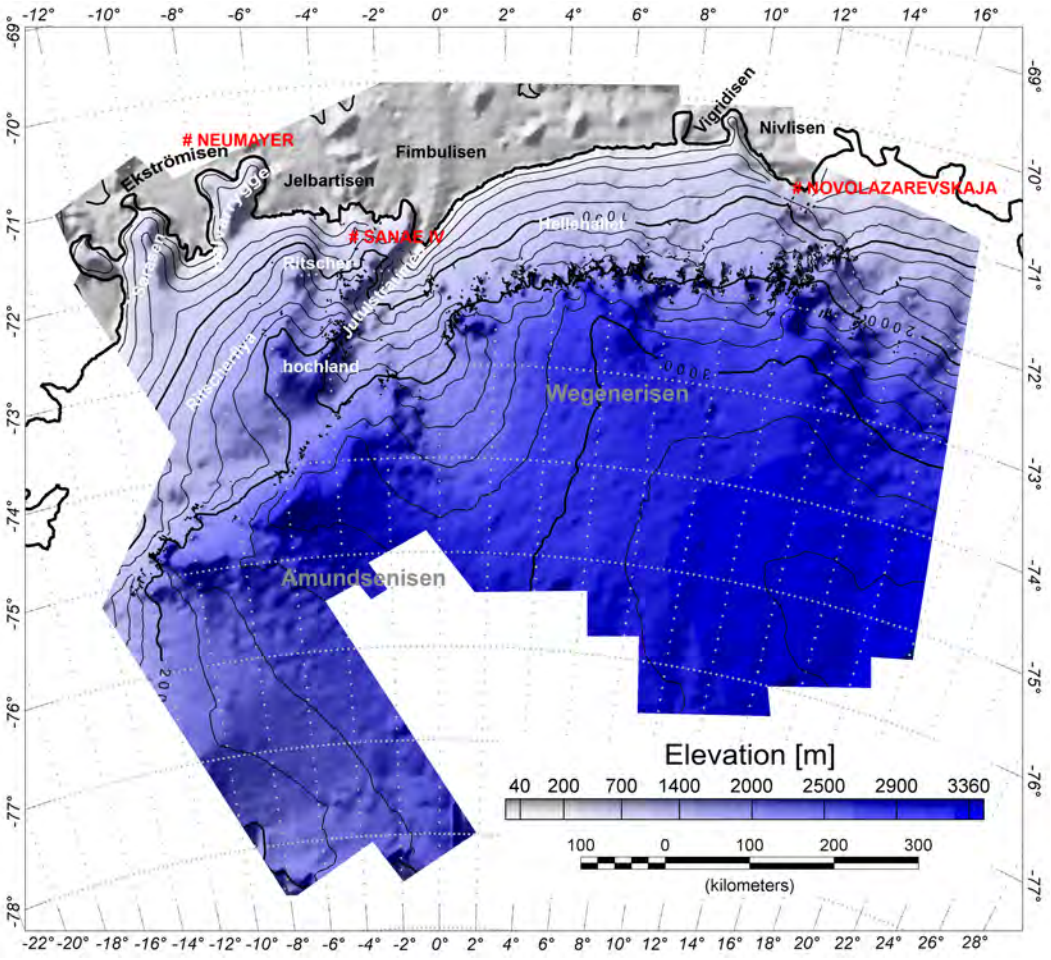

Figure 4.1: Compilation Ice Topography.

The outcropping mountains, at the 2000 m contour, mark the boundary with the highland plateau to the south, a more or less flat region, which has its maximum at 3400 m a.s.l..

The bedrock topography is more complex and has to be subdivided into the northern shelf, the central mountain chain and the hinterland, which displays deep basin structures within a highland plateau.

Contouring at sea level, which differs from the continent boundary displayed in widely available maps, the shelf region is characterized by huge basin structures, which are mostly orientated parallel to the coast. The average depth of these basins is around 500 m b.s.l.. Positive structures, albeit always below sea level, can be seen at the Soerasen and Halvfarryggen in the northwest and the ice rises Jelbartisen and Fimbulisen in the center-north. The Jutulstraumen- and Penksökket-trough-system seems to terminate at 0°. This tounge is the signature of both the speculative extent of the Jurassic trough system and the present mechanical erosion due to the glacier flow at $1\,\mathrm{kma}^{-1}$.

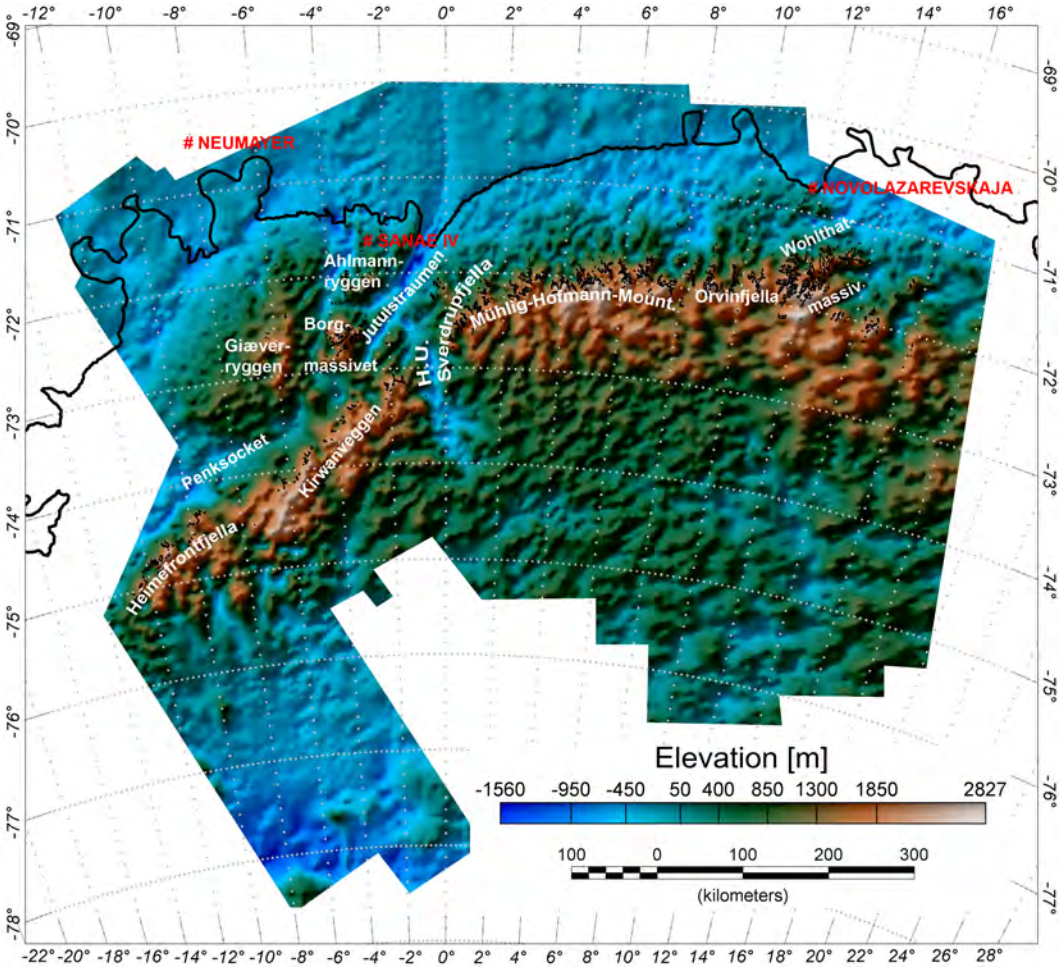

Figure 4.2: Compilation Bedrock Topography.

The mountain group was built up during the collision of East and West Gondwana, and can be described as an E-W striking band, 200 km in N-S extent, with maximum heights of 2000 m a.s.l.. This topographic massif is cut by the Jutulstraumen-Penksökket graben system. A N-S orientated branch of this trough, more than 10 km wide, with average heights of 400 m b.s.l., separates the EW segments of the mountain chain.

In the north-western area lie fragments of the Kalahari-Kapvaal Craton, which broke apart during Gondwana separation in Jurassic times. During the earlier collision with the old Antarctic craton, a crustal boundary was initiated that was much late reactivated as the Jutulstraumen-Penksökket graben system (72.5°S, 5°E). The graben system itself consists of four separate branches:
the E-W trending Penksökket, the NW-SE branch, west of Borgmassivet, parallel to the main branch of the Jutulstraumen trough, which reaches maximum depths of 1500 m b.s.l., and a N-S cutting branch.

The mountain-hinterland can be subdivided into two areas.
In the south western area, 200 km south of the Kottas mountains and Heimefrontfjella shear zone (Penksökket graben), a deep basin structure dominates the area of 270 x 300 km. The elevation decreases southward and reaches a minimum of 1000 m b.s.l.. At the edges of the surveyed area, only suggestive changes in topography can be recognized.

The hinterland of central DML (75°S, 10°W) displays average heights of 800 km above sea level. But internal segmentation is clearly visible on the basis of troughs, graben systems and highland plateaus. Numerous small trough-like features of maximum 20 km in width and below sea level may be highlighted as subglacial environments and may be worthy of more detailed investigation. A smoother plateau, well separated from the rest, can be recognized in the central southern area, measuring 300 km E-W and 150 km N-S, and may indicate an area of broad uplift.

4.2 Gravity

The free-air gravity map is characterized by long wavelength anomalies which represent deep seated crustal as well as upper mantle structures. As expected, there is a strong correlation between free-air gravity and sub ice elevation, as seen in the ice penetrating radar data. Due to the influence of these mass effects, the interpretative potential of the free-air anomaly is limited. The effect of the ice-rock density contrast can be compensated with the calculation of the Complete Bouguer anomaly, which is displayed in subsection 4.2.2.

4.2.1 Free-air Anomaly Map

After merging the data into one common database, a systematic adjustment procedure was used to reduce the crossover errors between the different campaigns. After this correction, the mean error can be given with 4.3 mGal, with an standard variation of 5.2 mGal.

The northern extent can be interpreted as typical of a stable continent-ocean transition. These positive anomalies of up to 100 mGal, which are oriented parallel to the coast, are induced by a crust thickness of 10 km including seaward dipping basalt segments (Jokat, 2003; 2004). These long wavelength anomalies portray in detail a more or less two dimensional continent-ocean transition zone. Only in the center, were the Jutulstraumen trough crosses onto the shelf, does the gravity field display any disturbance when compared to the surroundings **(1)**.

The continent-ocean transition zone is normally characterized by gradients of $5\,\mathrm{mGalkm^{-1}}$. From positive values the FAA decreases southward into gravity lows of around -70 mGal. Northern central DML displays a 200 km width gravity low **(2)**, while the western part shows a 100 km wide low between the shelf and the mountainous foreland **(3)**, caused by the increasing topography.

The Jutulstraumen-Penksökket graben system, with its four branches **(4)**, is still

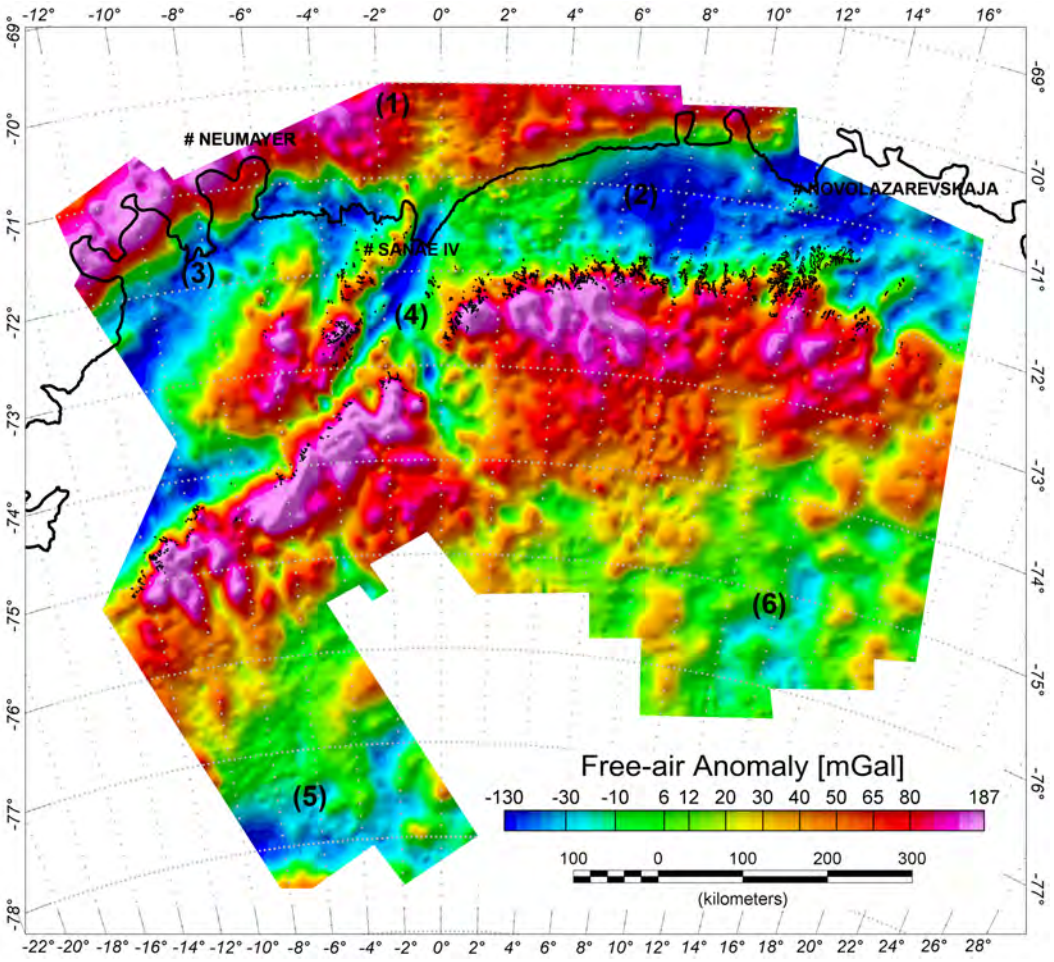

Figure 4.3: Compilation Free-air anomaly.

recognized as a set of gravity low structures with sharp flanking gradients. Here, minimum values of -130 mGal (comparable with the topographic minima of 1500 m b.s.l.) are measured.

The mountain chains display positive anomalies of 100 mGal and more, but show also internal segmentation, while the hinterland is characterized by values of around 0 mGal. In the southwest, a -50 mGal gravity low, 100 km in EW and NS extent, and with an additional N-S branch, is seen **(5)**. The center-east shows short wavelength anomalies (<50 km) strongly segmented, with both positive and negative values **(6)**.

4.2.2 Complete Bouguer Anomaly Map

The so-called Complete Bouguer anomaly reveals the internal crustal structure more clearly then the FAA, but is strongly influenced by the different calculation techniques used to derive it, especially the terrain correction. The Complete Bouguer Anomaly can be defined as the measured gravity field after subtraction of the gravity effect of a simple model of the crust. This effective tool allows comparisons of gravity anomalies worldwide.

Two main regional structures are visible:
The offshore region displays positive anomalies of around 100 mGal, striking parallel to the coastline and representing a crustal thickness of around 10 km and the presence of seaward dipping basalt sequences **(1)**. A southward decrease in gravity, with a gradient of 1.5 mGal/km represents this passive and stable continent-ocean transition, of a type known from numerous locations worldwide.

The second structure is entirely limited to the continental crust, but nonetheless shows significant changes in gravity.

The area of the Grunehogna Unit **(2)** is displayed by a rough and disturbed pattern of Bouguer Anomalies ranging from -100 mGal to 40 mGal. The geological history of this fragment of the Kalahari-Kapvaal Craton, including the formation of a failed rift system that appeared during Jurassic times is all recorded in this disturbed pattern.

Some additional observations:

- the Borgmassivet retwas a different CBA signal to those of the surrounding topographic blocks,
- the J-P trough system returns positive anomalies with respect to the surrounding mountainous areas, consistent with the presence of deep seated crustal material of high density. This might be interpreted as underplated mafic rocks, which can be in Jura related to a mantle driving mechanism for the failed rift,
- Receiver function analysis (Bayer, 2007) shows a crustal thickness of 38 km for Sanae station, situated on a block structure (mountain), which is represented in the CBA map by values of 40 mGal,
- the boundary to the Antarctic craton is marked by sharp gravity anomaly contrasts at the expected suture zone between the Grunehogna Unit and Maudheim Province.

The Antarctic craton itself displays various gravitational terranes:

In central DML, the Wohlthat Massif displays a remarkable gravity low **(3)** of up to -160 mGal, which may be influenced by the orogenic root of the mountain chain and which would be consistent with the crustal thickness of 48 km, from seismology. This anomaly differs from those of other mountainous regions with similar topographic elevations, which return gravity lows of around -80 to -100 mGal. Furthermore,

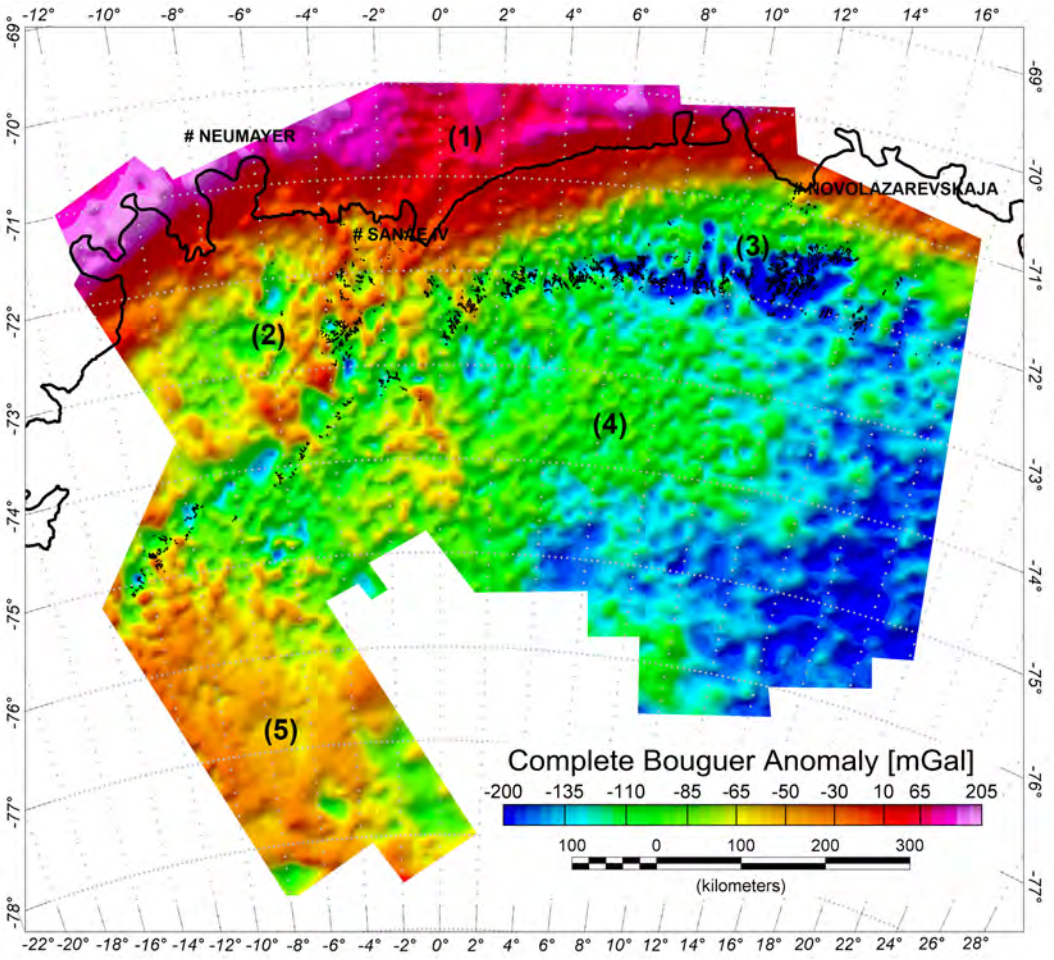

Figure 4.4: Complete Bouguer anomaly.

this gravity low (-140 mGal) strikes SE, with small segmentations in amplitude to -100 mGal and wavelengths of 15 km.

SW of the Wohlthat massif gravity low, a well defined pattern of stable gravity values of around -100 mGal is recognized. Internal structures, reaching values up to -40 mGal and with wavelengths around 20 km, with various orientations, are seen **(4)**.

A completely different gravity field is seen in the SW **(5)**. The small mountain group of the Heimefrontfjella is displayed by the expected values of -130 mGal, but its southern extension displays a much higher level of -40 to -20 mGal. This fundamental shift indicates a complete change in crustal behavior and may be induced by crustal thinning or the presence of a layer of denser material. Given the calculated crustal thickness of 53 km in the northern extent (Bayer, 2007), it is different to decide on which explanation is more reasonable. Whatever its source, the anomaly marks clearly a remarkable boundary.

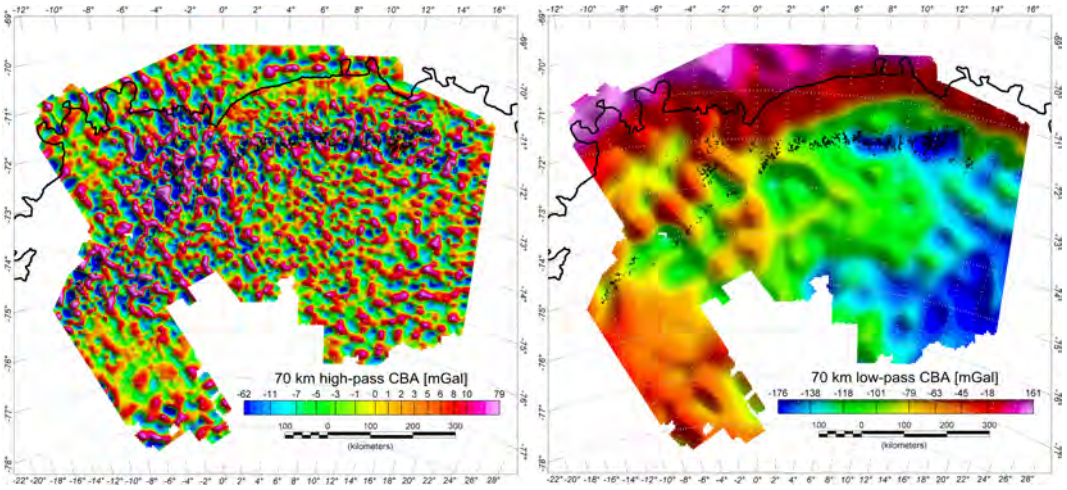

Figure 4.5: Results of filtering to separate gravity signals, *left:* 70 km high-pass, *right:* 70 km low-pass.

Wavelength filtering was applied in order to separate minor local inhomogeneities from regional gravity information. The filter length applied was 90 km (effective 70 km) for both the high and low pass filters. The high-pass focused on local inhomogeneities within the upper crust. Most of the positive anomalies revealed belong to causative sources that also give rise to magnetic anomalies. These anomalies might therefore be reasonably interpreted as due to gabbroic intrusions. Furthermore, granitic intrusions often poor in high susceptibility minerals. Gabbroic intrusions (also denser, hence positive CBA at short wavelength) often give rise to strong magnetic anomalies (magnetite, ilmenite). Additionally, this map suggests the presence of terrane structures (green level vs. dark blue) at the mountain chains and parts of the Grunehogna Unit.

Because of their great size, these units are better recognized following low-pass filtering. A better segmentation due to the crustal behavior is seen:
the continent-ocean transition zone (high anomalies), segments of the Grunehogna Unit, especially at the suture zone with the Maudheim Province (high anomalies), the Maudheim Province itself (medium anomalies, green) with some fragments, and, in the further SW a region of positive anomalies (high-orange), which may reveal a subunit of the MP (due to some internal layering) or, more speculatively, parts of the Coats Land Province (previous model suggestions would translate these units further to the SW, refer to Golynsky, 2007).

4.2.3 Isostasy Map

The isostatic models, which are based on topography that includes hard-rock material as well as load from the ice-sheet, display an idealized crustal behavior. The calculation considers an average crustal-density of 2670 kgm^{-3}, density contrast at the crustal-mantle boundary of 400 kgm^{-3} and an average crustal depth of 34 km.

The general trends of the isostatic anomalies are in good agreement with that of the Bouguer Anomaly. Differences in amplitudes can be interpreted as follow:

- The continent-ocean boundary cannot be described within the model suggestions. Here the Pratt model is favored,
- The extensive lows indicate the extent of the mountain range where the Airy model displays slightly better trend in gravity (not displayed here)
- Minor variations of Bouguer Anomaly cannot be realized within the isostasy based on local discontinuities
- Isostasy represents an idealized model and the residuals are used for interpretation purposes

The isostatic residuals are calculated by subtracting the isostatic gravity from Bouguer anomaly.

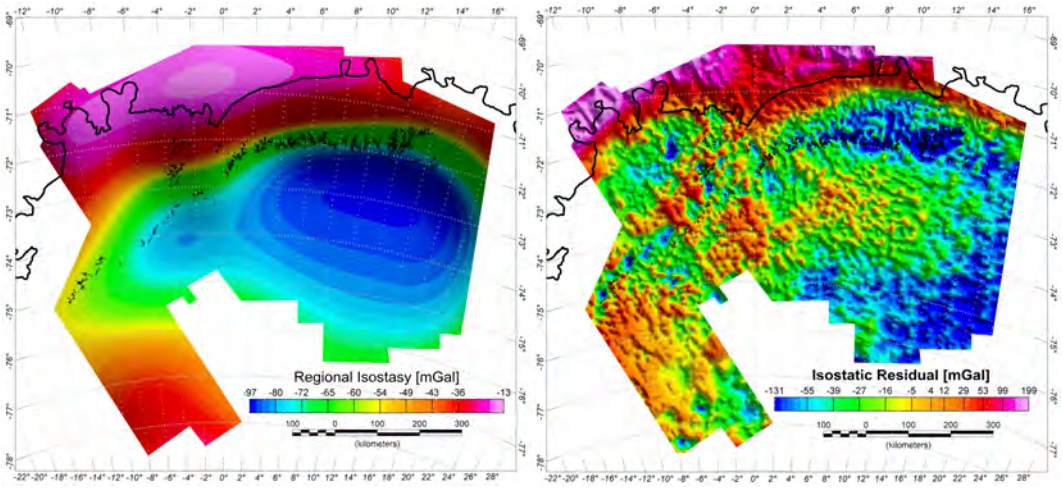

Figure 4.6: Isostasy. *left:* Regional Isostasy, *right:* Isostatic Residual.

Interpretation of the residual due to lift processes of the mountains lead to the assumption that negative amplitudes represent uplift structures. This is displayed within the mountain range, in correlation with the main trend. A remarkable low is situated around the Wohlthat massive (71.5°S, 12°E), including the foreland region. Two scenarios will explain this case:

- A mass deficit: due to a sediment basin with lower density
- Existence of orogenic root; the region is not in an isostatic equilibrium and the crust-mantle boundary layer is deeper than expected (root depth from seismology near 50 km, Bayer, 2007)

Both ideas are discussed by Reitmayer, (2005), GeoMaud expedition, 1995/96, who modeled the two cases (pers. comm.):

The mass deficit: Except the basin structure from RES data within the foreland region (no infill informations!), there is no direct indications and no additional data are available. Reitmayer modeled a basin with density contrast of $0.5\,\mathrm{gcm}^3$ and a depth of 3 km.
The orogenic root: The theory of the orogenic root leads to the question as to why the mountain range is not in equilibrium. An additional ice layer of 1.7-2.2 km would compensate the deficit- and glacial observations indicate reduction in ice sheet during the last thousands of years. The deficit are too high by a factor of 2-3 and not really realistic.

Positive anomalies indicates downlift processes (only in view of tectonic processes within the mountain range) or, if a correlation with the topography is given, the existence of masses within the upper crust. The resulting gravity force of the masses works in the opposite direction due to isostasy and is forced by horizontal tectonic and up- or downlift processes.

These suggestions correlate very well with the positive isostatic residual gravity within the Grunehogna Unit, which is characterized by rifting processes. All positive anomalies correlate with the main structures of the Jutulstraumen rift system indicating mass deficits in topography and moreover the positive gravity anomalies correlate with magnetic signatures as well.

Direct conclusions from isostatic residual gravity are difficult without the presence of additional information. Furthermore, it is well known that most of the mechanism working within the crust and mantle are represented within the gravity field. Crust to mantle processes includes oceanic subduction, continental subduction and delamination. Processes, which works from mantle to crust include underplating, intrusions and volcanism. All processes reported by geologists within this region.

4.3 Magnetic

As expected, the geologic structure of DML is rather complex and reflects several tectonic events resulting in different magnetic units. In the magnetic pattern, the western, central and eastern parts show similarities as well as their own characteristic pattern. Additionally, the data always display an overprint by magnetic anomalies that are associated with the fragments involved in Gondwana break-up.

4.3.1 Total Magnetic Intensity Map

After merging the data into one common database, a systematic adjustment procedure was used to reduce the crossover errors between the different campaigns. The data of VISA I/VISA III campaign are used as reference and data of VISA II campaign (by 20 nT) and VISA IV campaign (by 30 nT) were shifted. After this correction, the mean error can be given with 8.8 nT, with an standard variation of 7.3 nT.

Seaward dipping basalt sequences like those known from volcanic passive margins worldwide exist along the coast of DML. They are located within the continent-ocean transition zone and are marked by high amplitude magnetic anomalies, with strong gradients of up to 300 nT and with wavelengths of 25 km.

The western part of DML is dominated by the Grunehogna unit **(1)**, a cratonic fragment, with discrete, high intensity, spot-like and linear short-wavelength anomalies. A SW-NE, and coast parallel striking, linear anomaly of more than 150 km length displays amplitudes of 170 nT, with a wavelength of 15 km. Around this are scattered three dimensional anomalies with amplitudes of 220 nT and wavelengths of 15 km. Magnetic subunits situated in the western part of the GU are partially coexistent with topographic features, like the Borgmassivet, with wavelengths of up to 20 km.

In the central parts, prominent NE-SW striking anomalies in the H.U. Sverdrupfjella **(2)** with maximum amplitudes (in the south) of 1200 nT, and wavelengths of 30 km can be seen along with E-W trending anomalies of 300 nT in amplitude and 30 km width over the Penksökket. The prominent Jutulstraumen-Penksökket anomaly marks significant changes in magnetic strike direction **(3)**.

A WSW-ENE trending anomaly complex dominates the central part of the map **(4)**. The most eastern part of the complex consists of two individual anomalies, with wavelengths of 20 km and amplitudes of 200 nT. Very short wavelength anomalies are situated on the flanks. Further NE, the complex consists of a set of four parallel anomalies with amplitudes of up to 300 nT and wavelengths of 20 km. The overall length of this complex is nearly 350 km.

In the southeastern region, the magnetic anomaly pattern becomes less well organized **(5)**. Small circular and elliptical anomalies dominate the area, set on a background level of 50 nT, having maximum amplitudes of 200 nT and wavelengths of between 5 and 15 km.

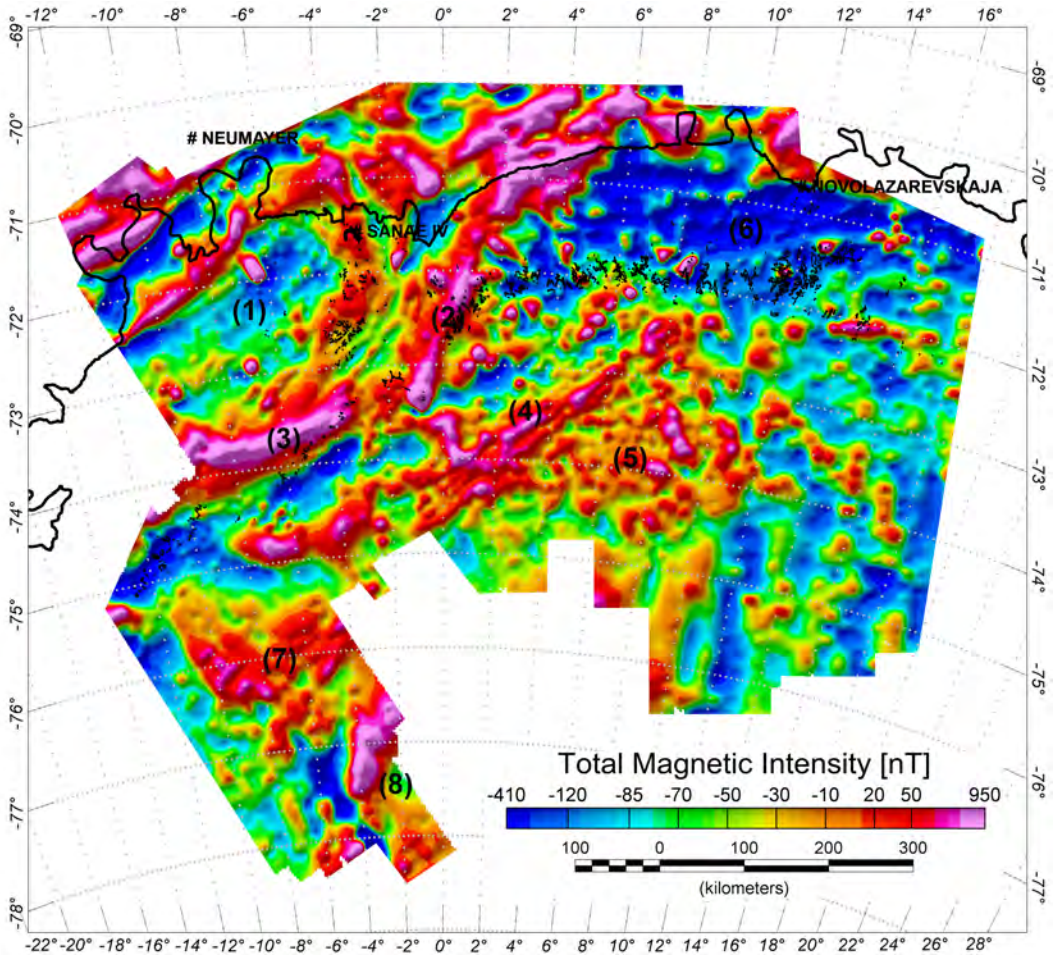

Figure 4.7: Compilation Total Magnetic Intensity.

The most easterly part of DML shows low amplitude, short wavelength anomalies with no or little continuity. A prominent structure is the magnetic low zone **(6)**, where the field is only disturbed by a small number of short wavelength anomalies.

The south-western region is dominated by two different magnetic anomaly complexes. The northern complex shows similarities to the central DML complex (4), like the parallel orientation, but at lower amplitudes of around 100 nT. The extent of this complex is also limited to an area of 50 km from E to W, as it dies out into a lower magnetic intensity background to the east **(7)**.
Further south a 150 km long, well defined anomaly complex **(8)**, strikes N-S. The anomaly shows two distinctive maxima with amplitudes from 200 to 400 nT, and has a wavelength of 40 km. On its eastern flank a 40 km wide magnetic low is situated, beyond which short wavelength anomalies with irregular structure occur.

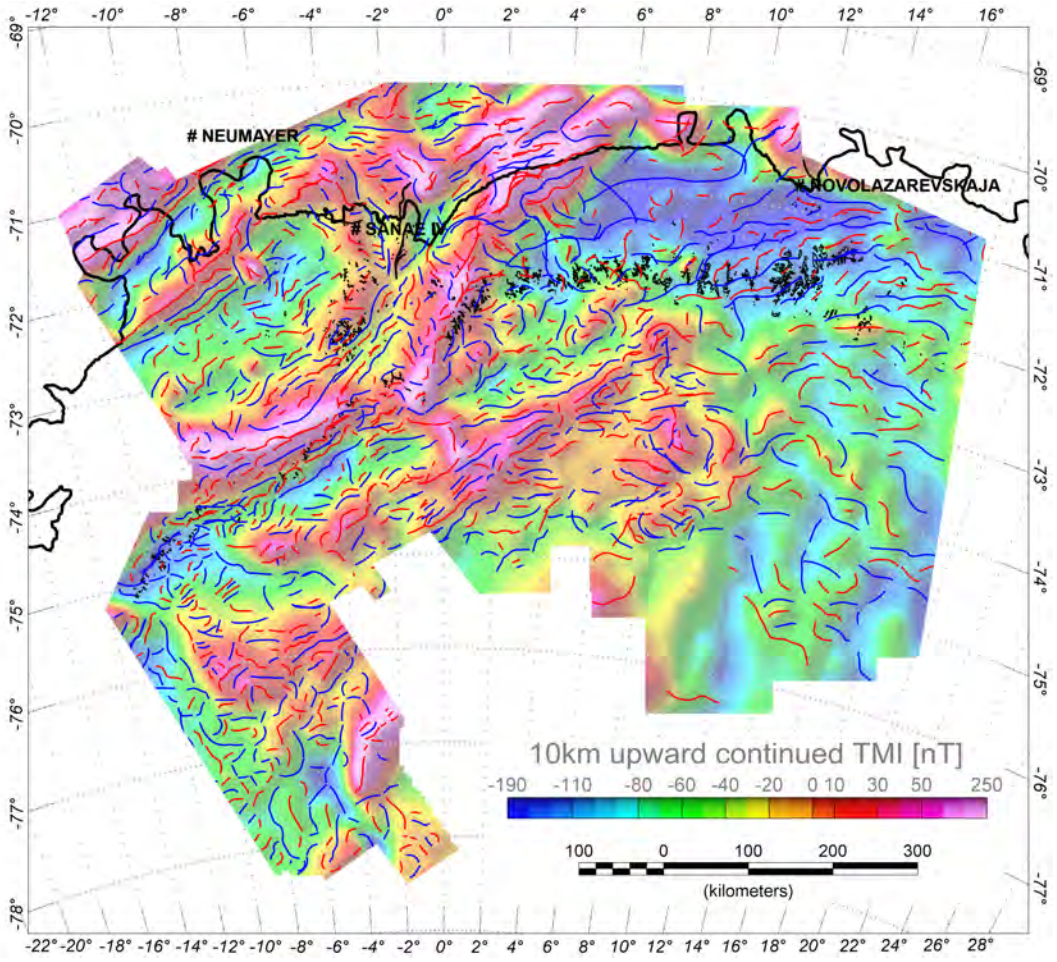

Figure 4.8: Main magnetic units (upward continued) with results of detailed mapping trend analysis overlaid.

To a first approximation, upward continuation of the TMI field will highlight the main magnetic structures and units, whereas highs sensitive trend mapping analysis can be undertake to display the complex pattern of the original. The overprinting character of magnetic anomalies varies somewhat throughout the study area, when interpreted from the different magnetic-tectonic trends. Various trend-regimes, ENE-WSW and E-W, as well as completely irregular pattern can be recognized, as displayed in figure 4.8, and must be interpreted in terms of different geotectonic histories of the various regions covered by the map.

4.3.2 Analytic Signal Map

The calculation of the Analytic Signal (AS) helps to reorientate magnetic anomalies directly over their sources, and gives more detail compared to the TMI, which is dominated by the superposition of neighboring anomalies. In comparison to the TMI map, a stronger segmentation of magnetic sources can be observed, combined with "zooning" (colourscale). The main structures, or deep-seated anomaly sources are highlighted in the displayed AS map, shown in figure 4.9. The following description is made with reference to the TMI map and so will highlight the observed differences:

The AS map is mainly characterized by more or less three dimensional anomalies: the loss of complex linear structures is clear. Neverless, linear alignments of the localized features are interpretable.

- The continent-ocean transition zone is now reduced to two main anomaly complexes, situated in the NE and the central north **(1)**. Between these, a band of circular anomalies is recognized. In the area of the Jutulstraumen ice tongue, a large circular anomaly **(2)** is now more strongly delineated than it was in the TMI map.
- The area of the Grunehogna unit displays 8 major anomalies **(3)**, which are irregularly orientated, while the rest of the unit shows rather incoherent magnetic signature.
- The H.U. Sverdrupfjella anomaly complex displays a new segmentation **(4)** and may be reinterpreted (see section Areas In Detail). The Penksökket anomaly can now be divided into a set of four single anomalies **(5)**.
- The WSW-ENE striking central anomaly complex **(6)** consists now of a set of well-separated elliptical anomalies arranged like in a chain. Similar chains but much lower in amplitude, can be recognized parallel to this to the north and south.
- In the most eastern part of DML **(7)**, three complexes of anomalies are highlighted: two of them, in the north and center, with a preferred EW orientation, and the third in the south centered region with a more NW-SE orientation.
- The northern part of the south-west displays a set of minor isolated anomalies, while the southern part displays a more massive anomaly complex striking NS **(8)**.

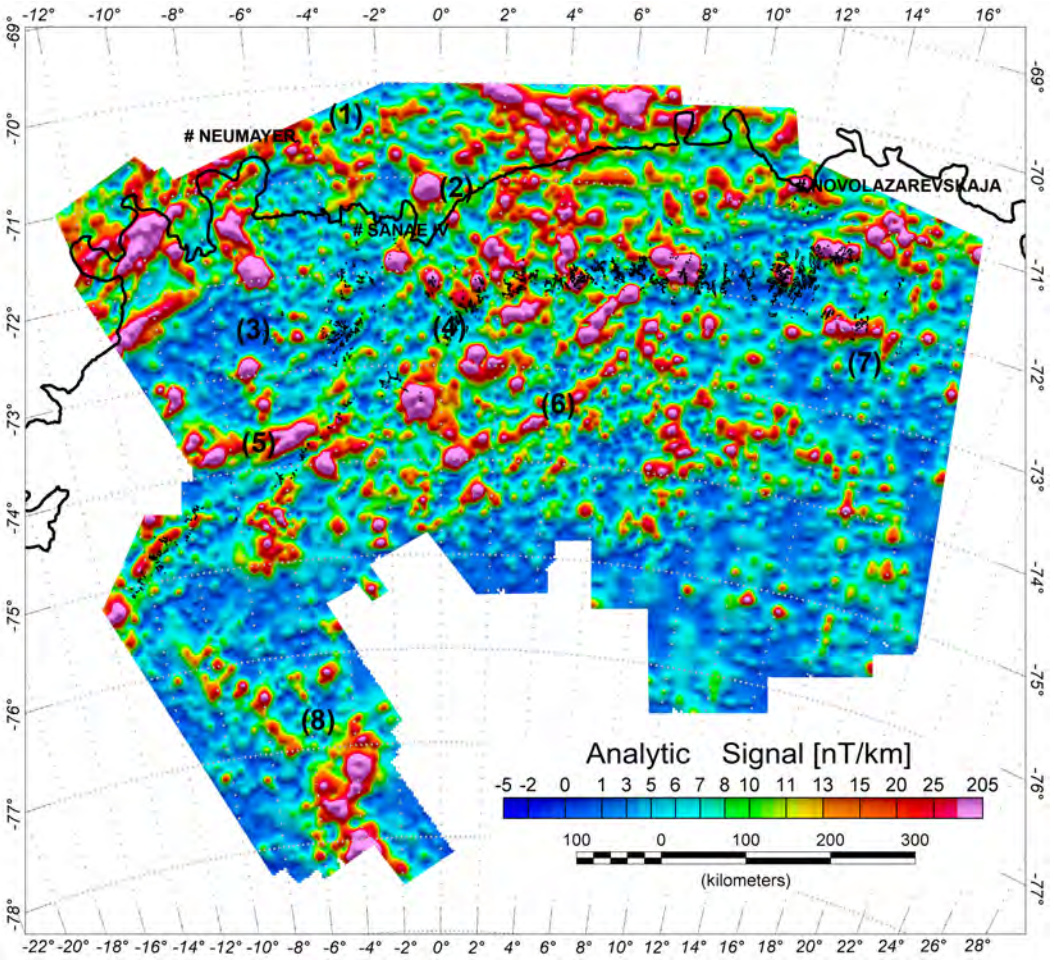

Figure 4.9: Analytic Signal analysis.

4.3.3 Tilt Derivative Map

Applying the tilt derivative highlights the signature of shallow magnetic sources and so gives some guidance on interpreting known lineaments and shear zones. In the displayed map, a frequency cut off is applied to focus on anomalies with positive contrasts in susceptibility. Red color belong to these positive anomalies, situated directly over their sources.

The main focus of this analysis is to find boundary structures between magnetic units, and so concentrate on the tectonic evolution. In general, the continent-ocean transition zone displays parallel striking complexes **(1)** but is disturbed in the eastern part, where it gives way to the GU. The GU can be identified by its circle-like structure **(2)**, displayed in the map. Internal segmentation of the unit is not strong.

The lineaments and shear zones **(3)** suggested by Golynsky, (2000), and the detailed interpretation of the small but highly detailed survey by Ferracioli, (2005), can be

confirmed and continued. These features mark the boundary between the GU and MP situated in the H.U. Sverdrupfjella and Penksökket.

The central anomaly complex **(4)** indicates the presence of WSW-ENE lineaments, and confirms geologic observations (Jacobs) further north in the Wohlthat Massif where they may change to be more EW orientated.

The south-western region becomes less clear **(x)**, because the TDR process highlights shifts between the flight lines at the expense of lithological signals. But, nevertheless, the northern part displays a parallel EW orientation, which is divided to the south by NS striking features.

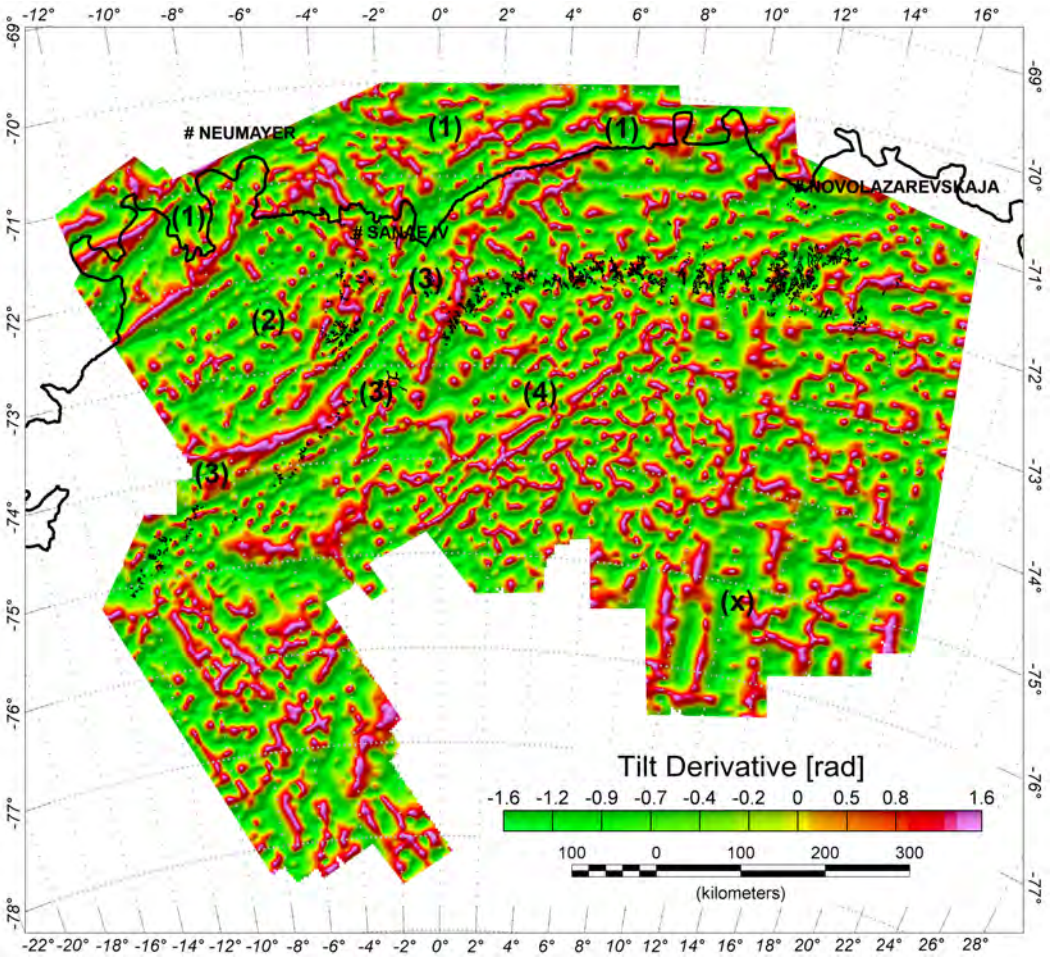

Figure 4.10: Tilt Derivative filter, to highlight only sources with positive susceptibility, low values are cut off.

4.4 Areas In Detail

The investigated area is to vast for a detailed description of it all to be made. Here, interesting patterns are extracted and investigated in detail. The huge, but geologically self-consistent Grunehogna Craton is focused on. Furthermore, different parts of the Maudheim Province are examined in detail.

4.4.1 Grunehogna Unit

The Grunehogna Unit corresponds to the Grunehogna (Province) Craton, a fragment of the Kalahari-Kapvaal Craton, consisting of Archaen granite basement overlain by undeformed Proterozoic sediments. Magnetically, the GU is characterized by broad featureless lows, with a few short wavelength anomalies. The widespread low amplitudes are situated in the center, while short wavelength spot-like highs and magnetic subunits are situated more towards the borders. The boundary to the MP can be followed along the E-W striking Penksökket Anomaly and the SW-NE striking Sverdrupfjella Anomaly complex.

GU-coast and shelf region: the offshore area is mainly influenced by linear, coast-parallel striking anomalies. These features, compared to purely continental anomalies, are huge in extent (more than 100 km in length), with average wavelengths of up to 50 km and amplitudes of 300 nT. Magnetic anomaly profile analysis suggest a slightly dip toward the south. These anomalies coincide with seaward dipping reflector sequences in seismic reflection data and mark the boundary between oceanic and continental crust. They connect the Princess Martha Coast Magnetic Anomaly (PMCMA) to the Explora Anomaly, both wide bands of coastal magnetic anomalies to the east and west. The AS-analysis supports the mostly linear nature of these anomalies, but also highlights amplitude maxima that can be interpreted as formed over large basaltic intrusion complexes. The TDR highlights shallow structures, which are connected to the wide, coast-parallel striking subcrop of basalts. Most of the anomalies are situated offshore, and there is no correlation with topography. The southern extension, toward the continent, is characterized by a magnetic low with amplitudes of around -300 nT, 400 km in E-W extent, with a width of 45 km.

GU-A unit: here, an E-W striking anomaly, nearly 250 km long, with amplitudes of 200 nT and a wavelength of around 25 km is prominent. While the TMI displays a more or less linear behavior, the AS separates this anomaly complex into a 100 km linear, E-W striking feature, with a depth-solution of between 7 and 2 km. The shape of magnetic anomaly suggests it may best be modeled as due to a thin dyke. Dipping slightly towards the south the anomaly betrays a more or less vertical source. Eastwards, two high amplitude and more N-S oriented elliptical anomalies are observed. Maximum amplitudes reach 500 nT for the southern and 900 nT for the northern anomaly, with estimated source depths between 2 and 1 km. The TDR suggests that more shallow sourced anomalies build the connection between these features as well as the presence of a EW oriented shear zone to the south.

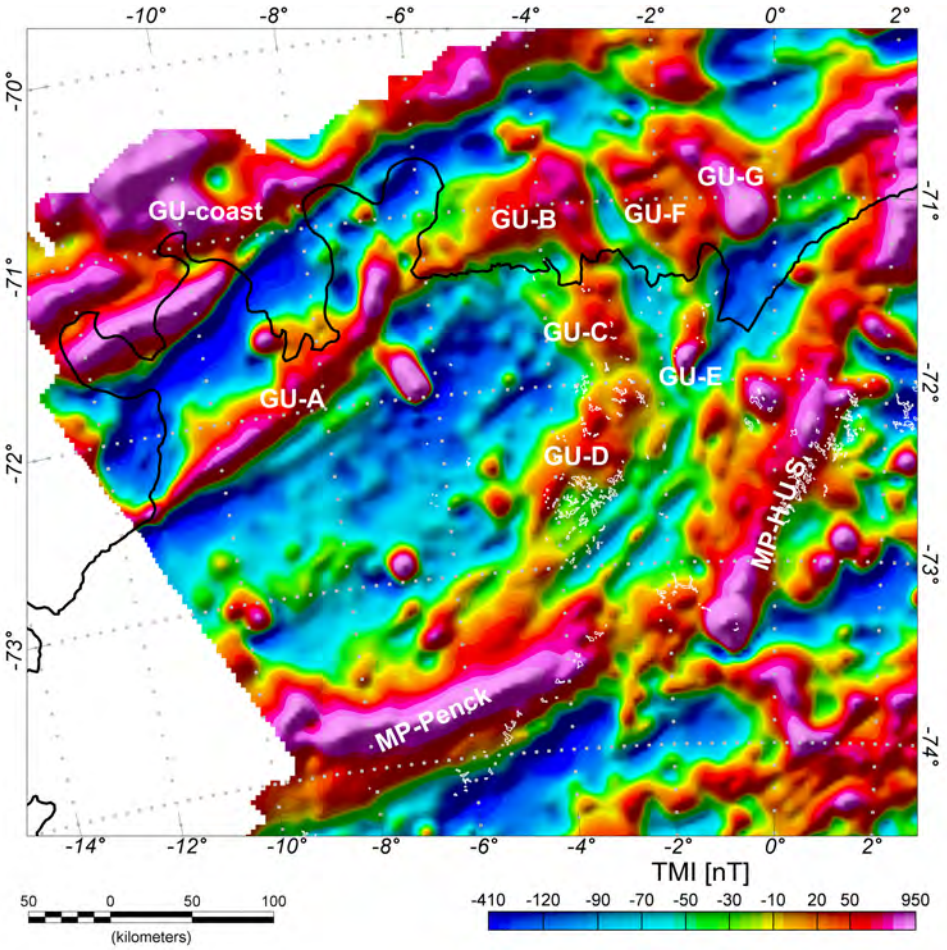

Figure 4.11: TMI, Grunehogna Province with its magnetic subunits, and the adjacent area of Maudheim Province, situated to the south and east.

Additionally, the abrupt changes in strike direction can be taken as indications for some lineaments. This corresponds well with the topography: the anomaly complex forms over a kind of channel, with topographic heights around 500 m b.s.l. that strikes dominantly parallel to the coast.

GU-B unit: this unit strikes NW-SE, for 75 km, with a maximum wavelength of 30 km and peak amplitudes of 100 nT. The response from AS displays several maxima, with diverse structures, while the TDR shows a network of EW and NS striking shallow sourced anomalies. Estimated depths for causative bodies lie within a range of 4 km at the flanks and 1 km over the center. The topographic background of this offshore region displays EW and NS trends at about 400 m b.s.l..

The southern continuation is the 60 km long, 40 km wide, **GU-C** unit. Moderate amplitudes of 60 nT, with four maxima, are seen in the TMI. A large block as magnetic source can be inferred from the shape of the magnetic anomaly. No special characteristics can be observed in the AS, but the TDR displays strong segmentation in a preferred NW-SE orientation.

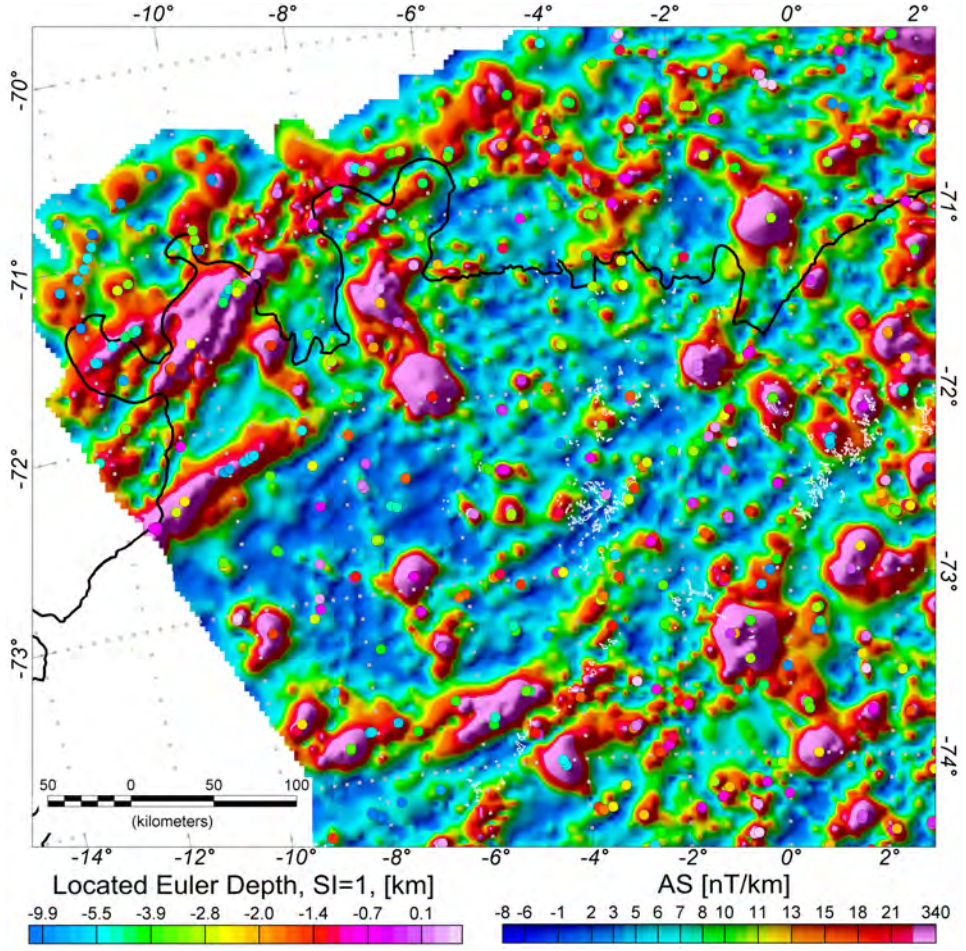

Figure 4.12: Analytic Signal, Grunehogna Province, AS overlain by Located Euler Deconvolution solution.

Indications for shear zones are given on each flank of this subunit. The eastern boundary in particular indicates a NW-SE striking shear zone, while the western flank is characterized by a chain of 8 km wide localized highs orientated NW-SE.

Topographically, the area is characterized by moderate gradients and the presence of the *Ahlmannryggen* nunatak group.

Southward, the **GU-D** unit, can be recognized, as a set of four distinctive highs, in total nearly 100 km in length and with a maximum width of 40 km, and maximum amplitudes of 75 nT. Strike changes between E-W and N-S and corresponds partially with the topographic terrain of the *Borgmassivet* complex. Significantly, most of the maxima correspond to strong topographic gradients, like the flanks of the trough system. Overall, the anomaly shape suggests another large block as the causative body. The AS displays no significant internal structures, while the TDR is characterized by slight NE-SW and EW trends. The Located Euler Deconvolution gives limited solutions for approximate depth, at 4 and 1 km.

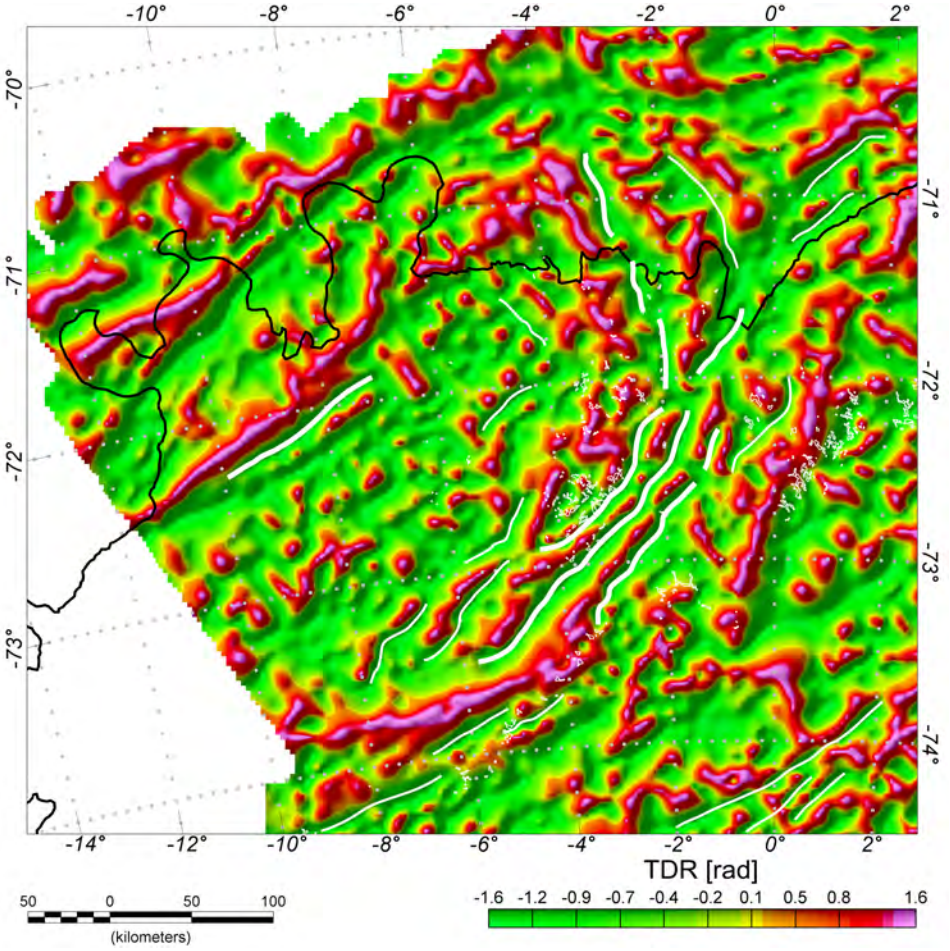

Figure 4.13: Tilt Derivative, Grunehogna Province, TDR to enhance shallow magnetic sources and interpreted lineaments.

The eastern and southern boundaries of this complex are connected with a lineament (shear zone). The boundaries are shallow sourced, linear SW-NE striking magnetic anomalies that display strong correlation with the strikes of bedrock topographic features.

Focusing on the strike of the boundary to the northeast, an abrupt change into western and eastern lineaments can be recognized. Additional subunits can be defined in each of these arms.

GU-E unit: high in amplitude at 600 nT, with a wavelength of 12 km and striking NS for 45 km, this anomaly coincides with the *Straumsnutane* nunatak group. A more or less vertical dyke source can be interpreted from the shape function of the magnetic anomaly. The AS marks a massive source with an approximate depth of around 0.7 km, while the TDR displays two separate bodies. Geographically situated on the eastern flank of the Jutulstraumen trough, this subunit covers a topographic horst structure.

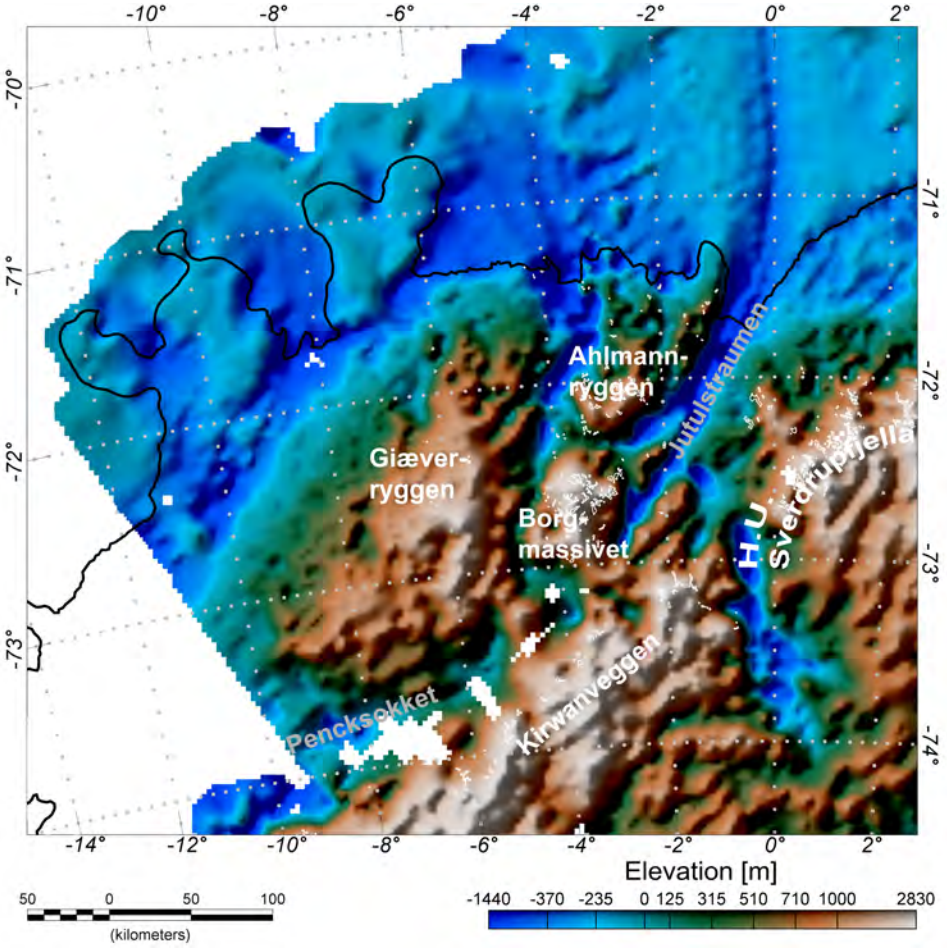

Figure 4.14: Bedrock Topography, Grunehogna Province, including some geographical names.

Two subunits bound in a kind of wedge, are seen further north: **GU-F**, NE of GU-E, consists of three, dominantly E-W striking anomalies with 10 to 20 km wavelength and moderate positive amplitudes of 130 nT. Only shallow responses from the TDR are recognized within the preferred E-W orientation. The eastern extent is characterized by sharp gradients, suggesting tectonic lineaments or shear zones.

Eastward, **GU-G** consists of a set of large circular anomalies arranged along a NW-SE line, 75 km long and up to 50 km wide. The TMI shows two maxima with amplitudes of 700 nT and 200 nT , whereas the AS and TDR show this complex as consisting of three parts. The most southern feature dominates in intensity and size. The source geometry can not be differentiated from the shape of the magnetic anomaly, but approximate depth of the causative bodies lies within the 4 - 3 km depth range. Relationships to bedrock topography are not well defined, but the main anomaly of this subunit is situated on the N-W flank of the Jutulstraumen trough system, offshore, where the topography displays rugged relief.

GU-others unit: There are numerous other less-well defined subunits in the GU's magnetic expression. In the center, where the TMI displays an extensive low, with a background level of -50 nT, there are several indications for localized magnetic sources. Simple zooming of color scale will highlight these features, but the AS and TDR analysis display several local anomalies with average wavelengths of 10 km. These features are dominantly symmetrical and round, but some minor linear trends can be recognized. These well separated features are all situated over strong gradients in bedrock topography. The anomalies are more or less irregularly oriented except in as much as the linear shallow sources are strongly correlated with subsurface topographic lineaments and trends.

Table 4.1: Subunits within the Grunehogna Craton.

unit	trends	amplitudes / wavelengths	approx. depth	topography	gravity
GU-coast	linear, coast-parallel, ≈100 km	300 nT, 50 km wide,	9 to4 km	normal shelf, ≈500 m b.s.l.	strong gradients
GU-A	E-W, linear, 250 km, local flanking highs, strike change to N-S	200 nT, 25 km wide 900/500 nT, 15 km wide	variable, 7 to 2 km 2 to 1 km	channel structure, 500 m b.s.l	linear, strong gradients
GU-B	linear,NW-SE, 75 km, strongly segmented	100 nT, 30 km wide	4 to 1 km	no significant, 400 m b.s.l.	disturbed
GU-C	NW-SE, irregular, 60 km long, weak, 3 maxima, strong flanking gradients, complex margins	100 nT, 40 km wide	no direct solution	variable, Ahlmannryggen, up to 1k m a.s.l.	disturbed
GU-D	tabular, E-W and N-S strike, 100 km long, three maxima, strong flanking gradients	100 nT, 40 km wide	4 to 1 km	strong gradients, Borgmassivet, up to 2k m a.s.l.	disturbed
GU-E	elliptical/tabular, 45 km NS trend	600 nT, 12 km wide	0.7 km	horst-flank structure	disturbed
GU-F	E-W trend, three sources, flank, strong flanking gradients	130 nT 10-20 km	1 km	rugged, 300 m b.s.l.	strong gradients
GU-G	NW-SE, 75 km, three maxima	200-700 nT, 50 km	4 to 3 km	flank of rift, rugged relief	strong gradients
GU-other	wide, broad, few, localized small anomalies	<100 nT, 10 km		variable	weak, smoothed

4.4.2 Maudheim Province

The suture zone between the Maudheim Province (MP) and Grunehogna Unit (GU) is characterized by strong magnetic anomalies. The boundary is marked with the Sverdrupfjella-Kirvanveggen Anomaly (SKA) and the Penksökket Anomaly, see figure 4.11.

The linear, E-W-trending Penksökket Anomaly, 220 km long and up to 50 km in wide, is the most prominent feature. While the TMI, with amplitudes from 200 to 450 nT, suggests a linear character, the AS displays segmentation into four different bodies with a SW-NE orientation. The dip direction, referred to a thin dyke model, varies over the whole extent from vertical to a slightly southward direction. The depth solution varies from 7 to 4 km. The sourced anomalies show the segmentation enhanced and highlights indications that might be interpreted as due to thrust and shear zones seen in outcrop. Geographically, the anomaly appears directly over the Penksökket trough, with average elevations of -300 m b.s.l. [MP-Penk].

To the east, at Kirvanveggen, the E-W trend bends towards the NE becomes much broader, and remains so until the region around Neumaerskarvet. There, a more S-N trend is observed, similar to thrust and shear zones seen in outcrop, as well as a set of shallow and irregular anomalies. Amplitudes of 40-80 nT and wavelengths of 5 to 10 km are observed. Topographically, the area is mountainous with the same S-N orientation.

The anomaly associated with the H.U. Sverdrupfjella dominates the eastern part of the map, shown in figure 4.11 and 4.15. This anomaly strikes SW-NE for 300 km and is 40 km wide with high amplitudes of up to 1200 nT. The anomaly consists of three distinctive segments with internal structure [MP-H.U.S.].

East of Neumearskarved, the maximum amplitude of 1200 nT is observed where the anomaly wavelength is 40 km. The AS highlights a wide tabular anomaly, which is situated on the eastern flank of a S-N-trending trough in a kind of bay. The dip direction of an intrusion interpreted from this anomaly is not clear from the shape of the anomaly, and tends from vertical to all possible dip directions. Estimated depths of causative sources vary between 5 and 0.5 km. TDR-highlighted shallow anomalies show a continuation towards the north and across the basement trough into the Sverdrupfjella mountain group.

At 72.5°S, the H.U.S. is offset by 20 km toward the east. The southern segment 130 km long with a wavelength of 35 to 40 km, and typical intensities of 250 nT are observed. Deep sources, 7 km, characterize the central part of this segment, while the flanks exhibit shallower-sourced anomalies, of 1 km. Maximum amplitudes are found over SW-NE trending topographic lineaments on the Sverdrupfjella mountain chain.

One main intrusion at *Straumsvola* and *Tvora* nunatak group, further NW, displays a NW-SE orientation, like some of the subunits of the GU. With a wavelength of 20 km, a length of 30 km and observed intensity of 270 nT, these anomalies are aligned along the eastern flank of the Jutulstraumen trough, where they are situated on a horst structure. A purely vertical source geometry is interpreted, and a depth solution gives

a value of 4 km. In additional, several localized anomalies (<15 km wavelength) can be seen in the surrounding area.

The third and northernmost segment of the H.U.S. anomaly occurs after a further eastwards offset of 20 km (71.5°S), and terminates at a coastline-parallel, directions and intensities are observed.

4.4.2.1 Central DML

Various magnetic patterns are recognized in central DML, as shown in figure 4.15.

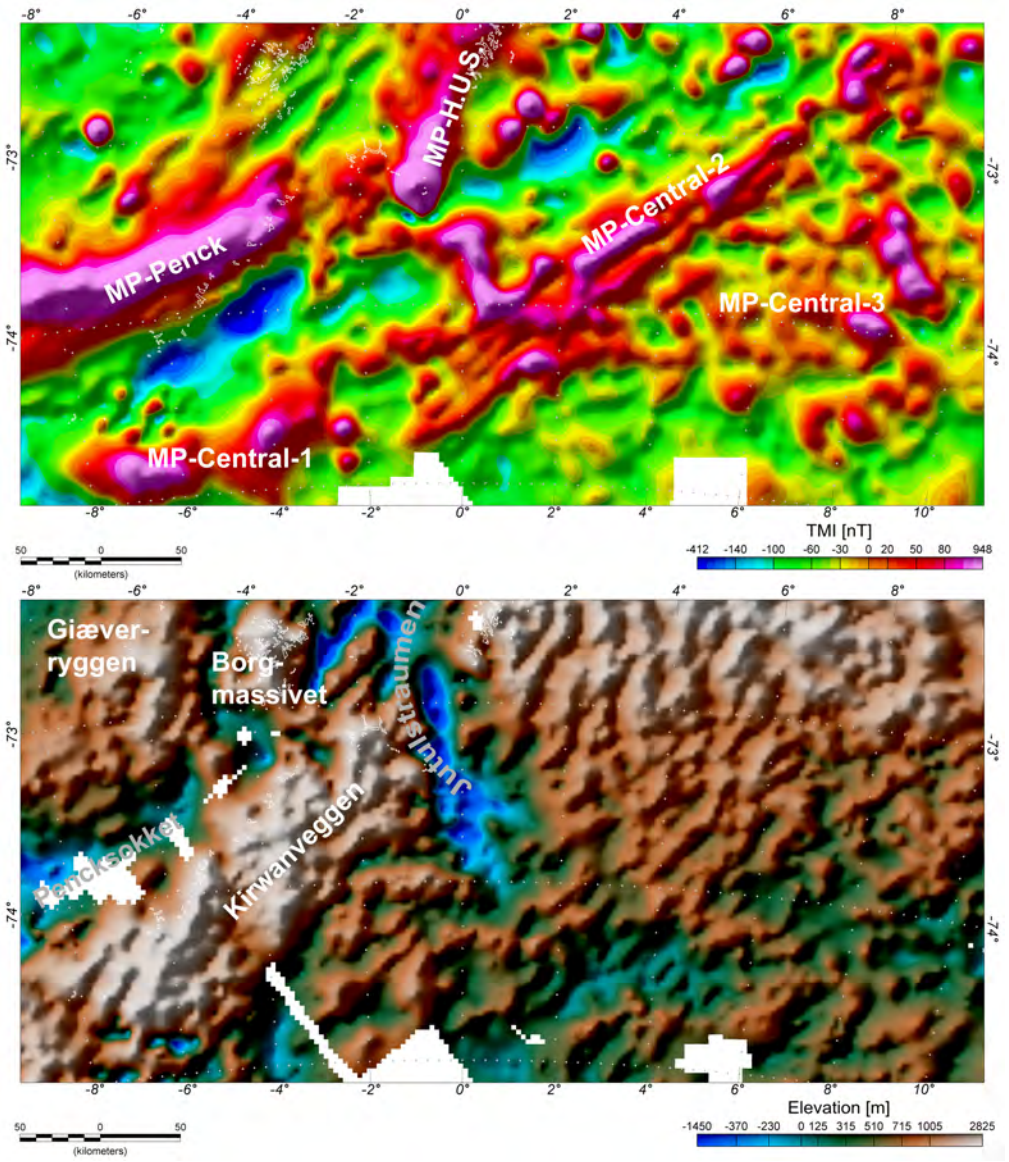

Figure 4.15: Maudheim Province, central DML, *top:* Total Magnetic Intensity, *bottom:* Bedrock topography.

We focus on the SW-NE trending anomalies. These mostly positive magnetic anomalies, displaying complete different pattern and their origins are unknown due to the lack of geological control.

MP-Central-1, situated in the most southwestern region, consists, with reference to the TMI, of two large anomalies. The western part strikes E-W for 75 km, with a wavelength of 35 km and amplitudes of 200 nT. The eastern anomaly strikes NE for 75 km with a width of 35 km and maximum amplitudes of 160 nT. The deep source characteristics and individual shapes of the anomalies, however, are dissimilar.

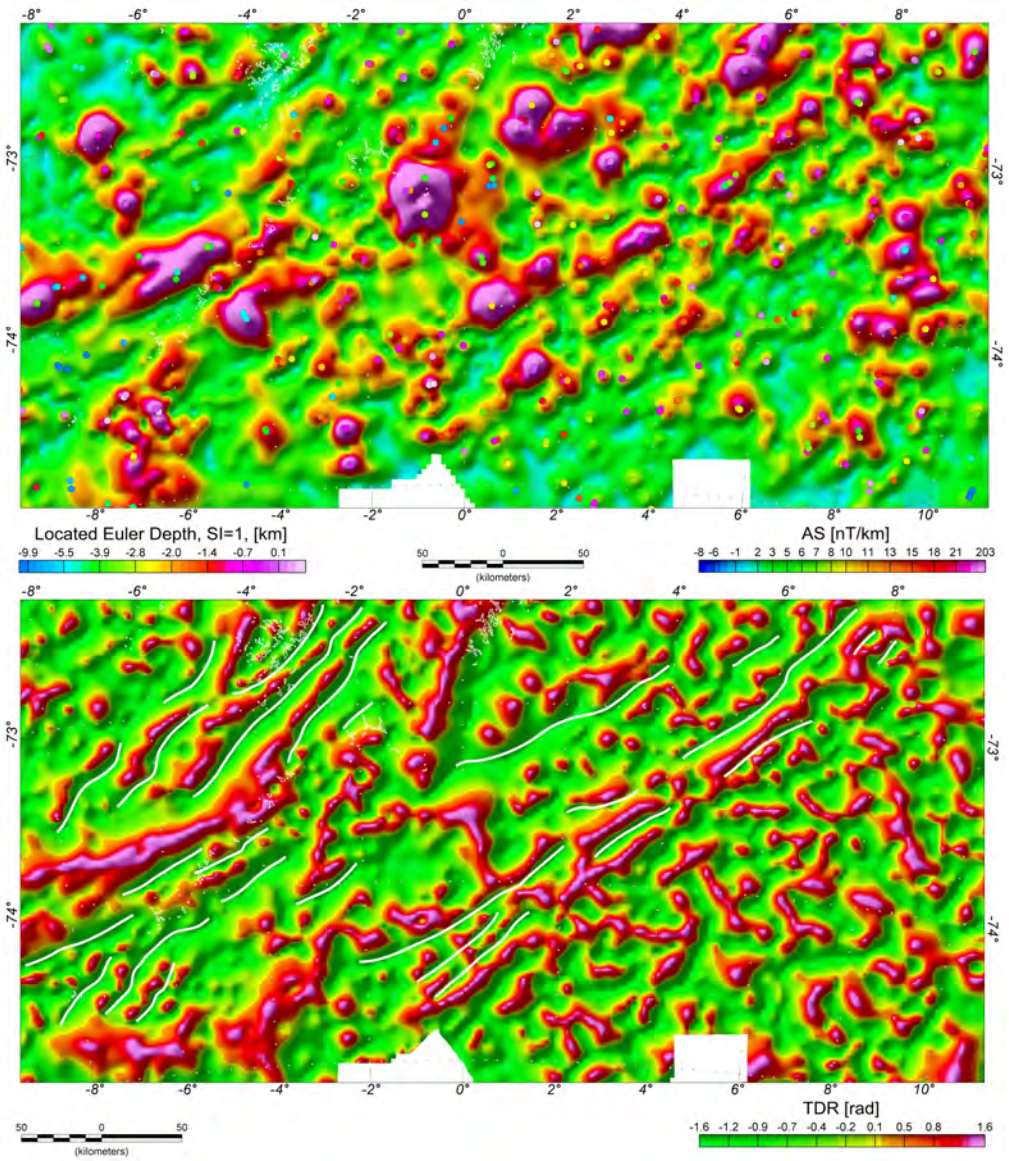

Figure 4.16: Maudheim Province, central DML, *top:* Analytic Signal, overlain by Located Euler depth solution, *bottom:* Tilt Derivative, overlain by interpreted lineaments.

The western unit consists of numerous well-separated features, with variable orientations and depth solutions of around 1 to 2 km. The source geometry is more or less vertical. The northern part consists of a chain of linked anomaly highs, trending NE and suggestive of shearing and related vertical thin dyke structures.

This part of MP-Central-1 is formed over a branch of the Kirvanveggen in the south and a chain of mountainous lineaments in the north.

The eastern part of MP-Central-1 consists of a main anomaly body situated in a NE-SW orientated trough. A approximate source depth of 4 km was calculated and may correspond to a large tectonic block. Shallow sources, characterized in the TDR, are related to changes in topography. On its western flank, two small circular anomalies are recognized with wavelengths of 15 km, intensity of 200 nT, and source depth of 0 km.

MP-Central-2 can be described as a system of linear parallel SW-NE trending anomalies. This unit is nearly 400 km long and has an average width of 65 km. Maximum amplitudes of 460 nT are measured for the individual striking anomalies, but averages are around 200 nT. Internally the anomalies displays N-S and E-W segmentation. The dominant source geometry is vertical. The AS highlights the northern substructures, with depths solutions ranging from 4 to 0.5 km. Shallow sources are mostly orientated parallel to the NE trend, consistent with a wide band of thrust and shear zones, marked in the figure 4.16. This interpretation is based on extrapolation of observations in the Wohlthat Massif.

The northern extent of MP-Central-2 displays several circular anomalies, with average wavelength of 30 km and intensities of up to 400 nT. The shapes of these magnetic anomalies suggest a vertical geometry of the causative bodies.

MP-Central-3 is characterized by a broad and weak anomaly pattern, with variable orientations. The background level is positive, with maximum amplitudes of 50 nT, and depth solutions around 1 km. Three main anomaly complexes disturb the background in the east, with wavelengths of 18 km and intensities of 150 nT. Estimated depths of these causative bodies are 6 km, 1.5 km and 0.7 km. Sub-ice topography provides some indications for an uplift structure related to MP-Central-3, both limited to the area of investigation.

4.4.2.2 Eastern DML

Figure 4.17 displays the most north-eastern part of the investigated area. Three significant changes in magnetic pattern are recognized and can be confidently related to the geology.

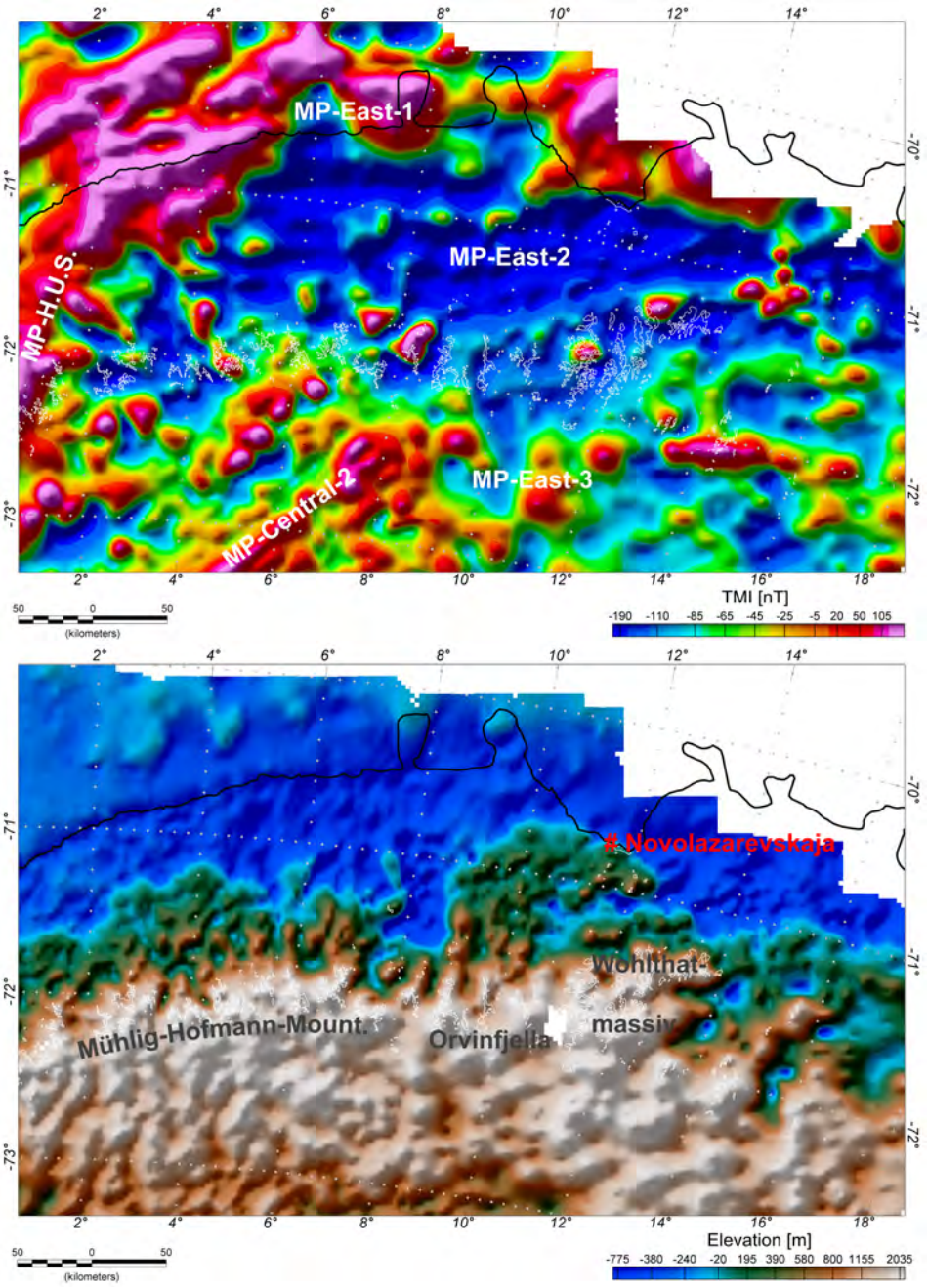

Figure 4.17: Maudheim Province, eastern DML, *top:* Total Magnetic Intensity, *bottom:* Bedrock topography.

The shelf unit in the north, **MP-East-1**, is dominated by extensive anomalies similar to those known from the other coastal regions of DML. Large in extent, at 70-130 km length and with wavelengths up to 35 km, the unit strikes parallel to the coast-line. Amplitudes of a few hundreds of nT, and a maximum of 500 nT, are observed. The focusing of magnetic anomalies over their sources, as shown in the AS, displays a more complex structure in orientation and extent. Segmentation from 10 to 40 km wavelength, for deep seated causative bodies, with 8 to 4 km depth, is established. Shallow anomaly complexes dominate parallel to the coast. The complete offshore region is dominated by more or less flat topography, which does not correlate with the magnetic anomaly pattern.

The **MP-EAST-2**-unit, is characterized by short wavelength low-amplitude magnetic anomalies superimposed on a negative background of -250 nT. Linear chains trend mostly E-W. Circular anomalies with average wavelengths of 12 km are recognized with amplitudes of -40 nT. The AS-filter highlights some additional features that are not evident in the TMI-map. Estimated depths for these anomalies' causative bodies range from 9 to 4 to 1 km, and they are mostly situated over topographic irregularities. Shallow and more linear sources are observed over the whole area, whose background field is negative. The dominant orientation in the central part is E-W. Orientations becomes less obvious in the western part, towards the H.U. Sverdrupfjella, where a more NE-SW trend is recognized. The eastern extent of this unit lies beyond the limits of the survey. An eastern complex consists of five isolated anomalies with wavelengths of 11 km and intensities of 200 nT, but does not define the boundary of this subunit. The estimated depth of these anomalies lies in a range between 2 and 0.5 km. Topographically, the area is underlain by a huge basin structure. Minor structures, especially south and south-east of the Russian base Novolasarewskaja and around the Schirmacher Oasis disturb these deep seated structures with average topographic heights of 500 m b.s.l for the basin structure and 160 m for the Schirmacher Oasis and outcrops.

A change in the magnetic pattern is recognized within the mountain chains, where the **MP-EAST-3**-unit is situated. MP-East-3 continues beyond the southern edge of this map.
A negative background of -80 nT characterizes the study area and is disturbed by smaller local anomalies without any obvious geometric or geological signature. The AS displays a number of prominent circular anomalies that partially correlate with outcrops of A-type granitoides within and around the Wohlthat-Massif. Intensities of 100 to 200 nT are recognized, with average wavelengths of 10 km. Various depth solutions are calculated, varying from 4 to 1 km. The TDR signal reflects better correlation between geologically-defined granite localities and shallow magnetic sources. Geographically, these intrusions are based within areas of strong topographic gradients.

Due to the incomplete success of the levelling process, any detailed interpretations that aim to map geological boundaries would be inappropriate for the more southern parts of this area. With respect to these, the AWI will fly more tie-lines in January 2008, which should lead to a better levelling solution for this survey and so help in further interpretation.

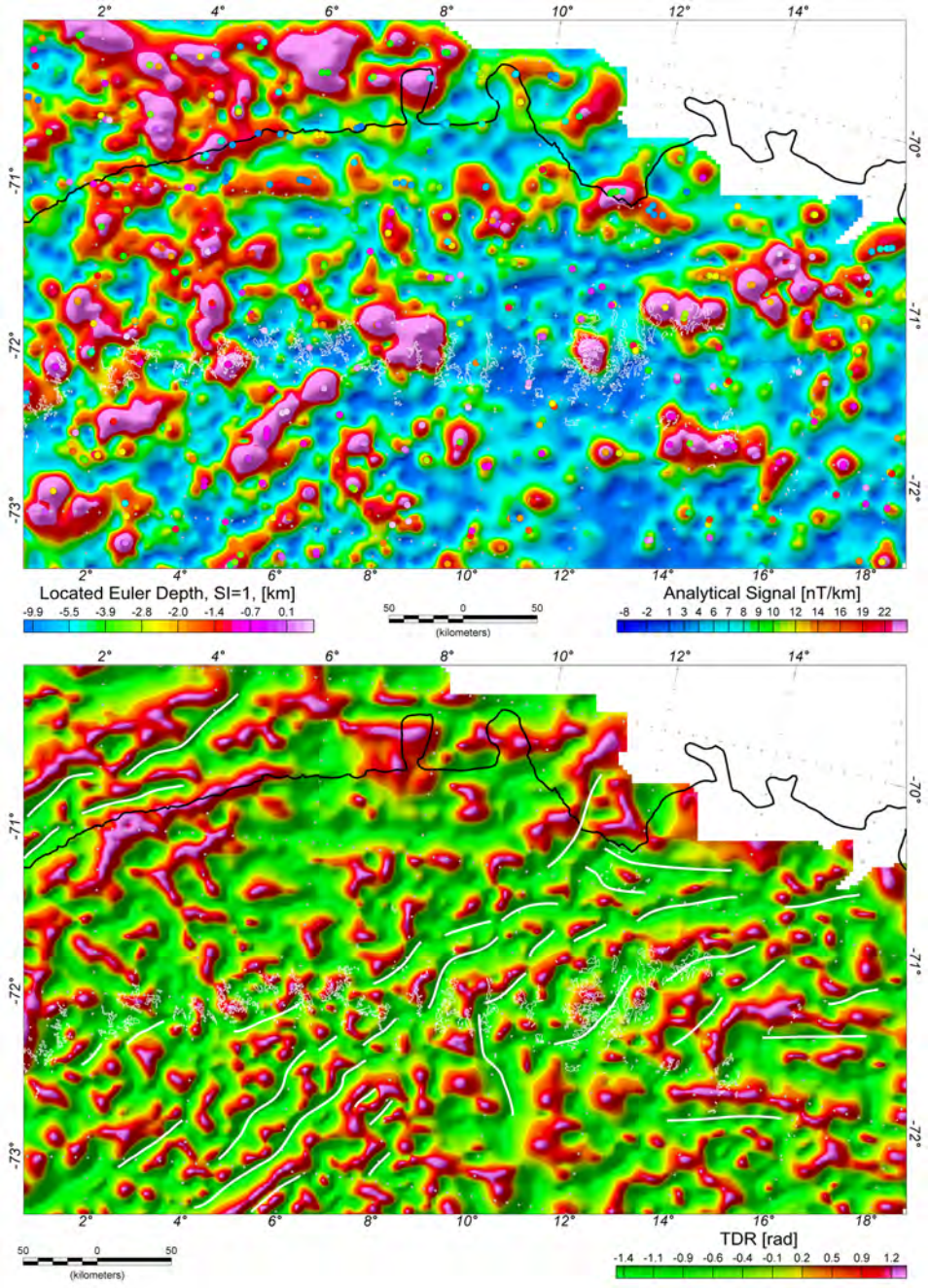

Figure 4.18: Maudheim Province, eastern DML, *top:* Analytic Signal, overlain by Located Euler depth solution, *bottom:* Tilt Derivative, overlain by interpreted lineaments.

Table 4.2: Subunits within the Maudheim Province.

unit	trends	amplitudes / wavelengths	approx. depth	topography	gravity
MP-Penk	E-W, linear, ≈220 km, segmented, four units	200-400 nT, 50 km wide,	7 to 4 km	trough, 300 m b.s.l.	disturbed
MP-HUS	SW-NE, linear, 300 km, segmented, three unit trends	ave.200 nT, 1200 nT max., 40 km wide	variable, 7 to 0.5 km	trough system, mountainous	disturbed
MP-Central-1	linear, 75 km, EW and NE trend, 2 segments, flanking circular intrusion, strong flanking gradients	200 nT, 35 km wide	2 to 1 km 4 km,	strong gradients on mountainous flanks	disturbed
MP-Central-2	SW-NE trend, 400 km, parallel, strong flanking gradients	200 nT, 460 nT max. 65 km wide	4 to 0.5 km	1k m a.s.l., mountainous	segmented, broad
MP-Central-3	weak, broad, various, shallow sourced, circular anomalies	50 nT, 18 km wide, 150 nT	1 km 6 to 1 km	800 m a.s.l., SW-NE segmentation, uplift structure	broad
MP-East-1	70-130 km, various, coast parallel	200-500 nT, 10-40 km wide	8 to 4 km	offshore, ≈500 m b.s.l.	strong, smoothed
MP-East-2	mostly E-W, magnetic low zone, several circular anomalies	-40 nT, 200 nT, 11 km wide	9 ,4 ,1 km 2 to 0.5 km	basin, 500 m b.s.l., topogr. irregularities, 160 m a.s.l.	broad, weak, isostatic- interest
MP-East-3	undifferentiated, several circular anomalies	200 nT, 10 km wide	4 to 1 km	strong gradients, mountainous	broad
MP-others	wide, broad, single circular anomalies	200 nT, 10-15 km wide		related	

4.5 Geologic model suggestions

The suggestions for a combined geological model are based on a detailed mapping strategy, as shown in the previous chapters, in combination with the Curvature analysis, displayed in the Appendix D. The displayed models are consistent with each other, including potential field data and the bedrock topography..

The Grunehogna Unit corresponds to the Grunehogna (Province) Craton, a fragment of the Kalahari-Kapvaal-Craton and is characterized:

- topographically: by a well-separated units in combination with a complex graben structure. Strike and direction of the mountainous region emphasizes the collision with the East Antarctic Craton.
- gravitational: the lithospheric response is characterized by strong gradients within the transpression zone, the central part displays a stable pattern.
- magnetically: widespread low amplitudes and spot-like highs in combination with several subunits towards the border.

The southern extension of the Grunehogna Craton is the Maudheim Province, which has Grenvillian age. The suture zone is characterized by strong anomalies. The mobile belt system displays:

- topographically: three well separated main structures: mountain, highland plateau and basin
- gravitational: various units which corresponds with the magnetic subunits
- magnetically: magnetic units are very variable and display various trends, overprinting character is always visible

The suggested separation of the mobile belt, in Maudheim Province and the Central Dronning Maud Land, Golynsky (2007), cannot be verified. An internal segmentation due to terranes is clearly seen and corresponds with all three datasets, but the exact definition in terms of geological provinces is limited with reference to the surveyed area.

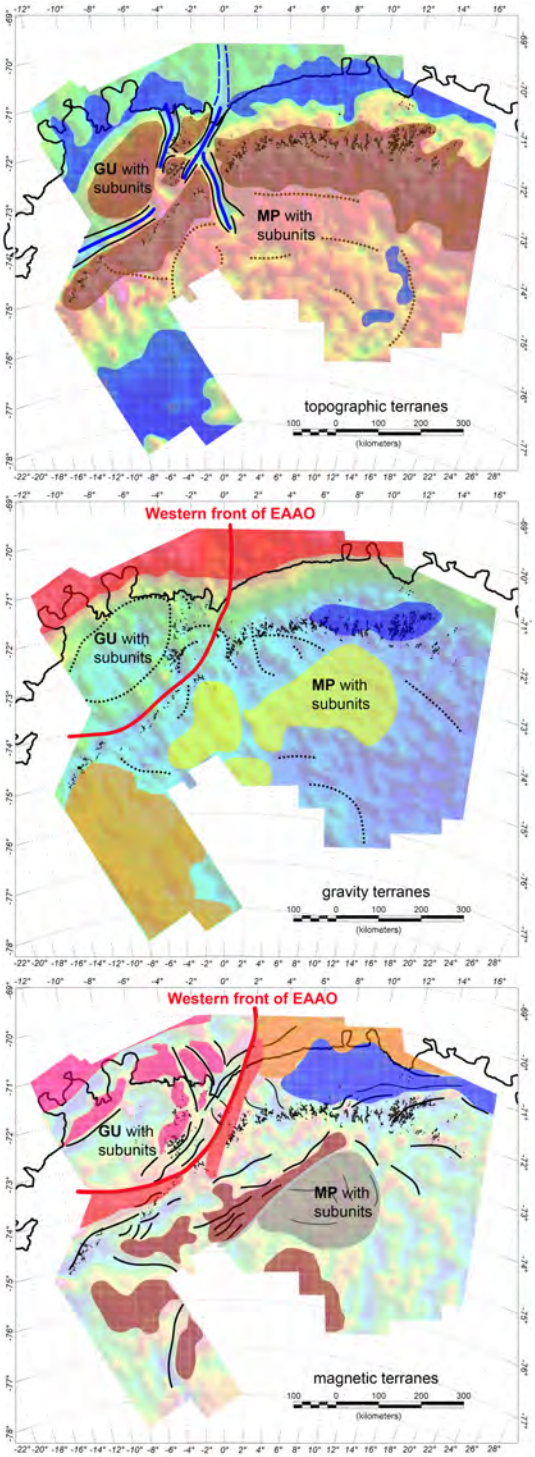

Figure 4.19: Geologic model suggestions, *top:* topographic units, *middle:* gravity units, *bottom:* magnetic units.

Chapter 5

SUMMARY

Within the VISA project the continental lithosphere of DML was systematically mapped and geophysically investigated in order to achieve a better understanding of the geology of Gondwanaland. This investigation covers a very large region of more than 1.2 Million km^2, which is about four times the size of Germany at 350000 km^2. Within this long-term collaborative project between the TU-Dresden and AWI, which includes a variety of multidisciplinary targets, this thesis concentrates on airborne potential field data and the interpretation of the Antarctic lithosphere. Since only the highest peaks of the DML mountain chains can be geologically sampled, indirect geophysical methods are required. Given this and the limited time window for scientific campaigns during the austral summer, fast and highly detailed investigation techniques are required.

Aero-magnetic and gravity surveys have been flown during the past 20 years. The development of airborne techniques have contributed toward a better understanding of the variety of regional tectonic provinces of the Antarctic continent. The extent of the survey area, from 14° W to 20° E and from 70° S to 78.5° S, is large enough to fully recognize long-wavelength anomalies. However, smaller features could also be mapped, owing to an average line spacing of about 10 km. With this spacing, the line spacing permits a good regional interpretation.

Old lithospheric boundaries between the Archean Craton, the Grunehogna Province, and the Proterozoic to Early Paleozoic mobile belt, the Maudheim Province, could be interpreted. Thrust faults have also been mapped, and their formation must be related to tectonic events that occurred in both Grenvillian and Pan-African times.

The Archaen to Mid-Proterozoic Grunehogna Province consists of Archean granites, which crop out in the Annandandagstoppane region and is overlain by the Mid-Proterozoic Ritscherflya supergroup of relatively undeformed sedimentary and volcanogenic rocks of the Ahlmannryggen and Jutulstraumen groups. Intrusions, theoleiitic sills and dykes, are reported within the Ritscherflya supergroup. The Straumsnutane Formation, andesitic lava flows with pyroclastics and sediments, forms a further element of the Ritscherflya supergroup (e.g. Groenewald et al., 1991; Martin, 1986).

The Grunehogna unit is associated with a broad and relatively featureless magnetic low, with a few circular short-wavelength anomalies, whose low amplitudes and short wavelengths suggesting a shallow magnetic basement. The central part is transected by the PMCMA, and may delineate a structure of crustal weakness. This anomaly pattern can be traced further west into the Weddell Sea shelf. To the east, two circular magnetic anomalies, which may locate mafic intrusions, define the eastern limit. Other magnetic units are recognized on the eastern extent, next to the Jutulstraumen. These units are mostly low in amplitude and display various trend characteristics, most of which can be related topographically-defined horst structures. The gravity field displays an undisturbed pattern in the central part

Of special note is the Jutulstraumen area. This region may represent a branch of a Jurassic-aged rift system. This system may be related either to active rifting processes involving the mantle plume that sourced the Karoo-Ferrar large igneous province in Africa and Antarctica (Cox, 1992), or may represent a passive rift structure.
A NE-SW oriented thrust fault crosses this region, and the topography may point to complex deformation. This area is occupied by a major structural boundary between the Grunehogna- and Maudheim Provinces and may have been part of a major transpressional fault system which was active during Pan-African deformation. The non-magnetic zone over the proposed Jutulstraumen rift is difficult to explain, but may reflect the presence of post-Jurassic sedimentary rock or sedimentary infill, or, alternatively an amagnetic rifting process. Prominent trends could be mapped. The NE-SW trend has already been recognized (Ferraccioli, 2005) and a highly perpendicular NW-SE trend can also be defined. Notably, these trends are found over the entire transpression zone, i.e. in the H.U. Sverdrupfjella and in the adjacent subunits of the GU. This leads to the suggestion that the rift was a region of active extension at different times and in directions.

The boundary to the Maudheim Province is defined by continuous linear magnetic highs: the Penksökket Anomaly in the south and the H.U. Sverdrupfjella Anomaly complex in the east.

The Maudheim Province, and its Sverdrupfjella supergroup displays two lithostratigraphic ensembles: amphibolite facies calc-alkaline metavolcanic rocks in the west and granulite facies para- and ortho-gneisses in the east, which are intruded by Pan African-age granites. Outcrops at Kirvanveggen, Heimefrontfjella and Vestfjella display continental flood-basalts that can be interpreted as remnants of the Karoo-Ferrar large igneous province. At the H.U. Sverdrupfjella, Jurassic alkaline intrusions are observed (Straumsvora and Tvora) and may relate to crustal extension and the presence of a rift system .
The central area of DML hosts Grenvillian rocks that were entirely transformed during Pan-African reactivation. These events altered the metamorphic assemblages as well as reactivating older tectonic structures. The reactivation and intrusion of magma into the Grenvillian crust at 600 Ma was followed by tectonism, metamorphism and a late stage of magmatism at 500 Ma (e.g. Shiraishi, 1994, Jacobs, 1998).

Different magnetic trends could be mapped, and these vary from NE-SW to E-W. Irregular patterns are also present. Low amplitudes with weak linear trends, are recognized. Only a few circular highs interfere with this magnetic pattern. On the basis of changing gradients in the TMI, the MP can be subdivided into several units: the continent-ocean transition zone, marked by a strong anomaly pattern, followed southward by a distinctive magnetic low. The Central Dronning Maud Land is characterized by a WSW-ENE linear anomaly complex and further south, by a weak zone in terms of amplitudes. The southwestern region can be divided into three distinctive pattern. Nearly all units of the entire region display numerous, mostly circular, magnetic highs, which are well separated.

The overprinting character of magnetic anomalies is very variable within the area and shows various trends separating subunits as well as many indications of shearing and thrust faults. The sources of many anomalies are obvious, where they correspond to known outcrop geology. Others, and these are the majority, relate to structures concealed under ice-cover, and their origin is more speculative.

Often, mismatches are recognized between magnetic observations in the TMI field, and well recognized bodies in outcrop geology. Problems like this can be addressed in different ways. Observation techniques, line spacing and sample interval which define the lateral resolution, were chosen to detect structure in the order to regional studies. On the other hand, the geological observations will always take precedence over the remote sensing techniques- and, of course, the Earth is not homogeneous. Normally, granitoids are associated with high susceptibility values, and so they ought to be detectable with magnetic methods. In field studies, however, such bodies often occur with an anorthositic component which has a low susceptibility, and granitoids are confined to its flanks (Piech et al., 2005). This arrangement may give rise to variations in size and susceptibility that, when combined with the resolution limits of a given survey, lead to only the larger magnetized bodies being recognized. The applied TDR technique correlates well with known geological sample areas.

Attempts to match cratonic fragments on the basis of potential field methods alone are always difficult in particular with low resolution data with line spacings of 10 km. On the other hand, airborne-based investigations are a proper tool to provide first insights of large-scale tectonic features. As such, further investigations are necessary, based on seismic and geological techniques and using more detailed airborne investigations, based on closer line-spacings.

Chapter 6

OUTLOOK

Aircrafts serving as multi-instrumentation platforms provide measurements of magnetic intensity, gravity, bedrock- and ice topography, and result in a fast and effective observation technique for the interpretation of lithospheric boundaries. The resulting data are only as valuable as their resolution and homogeneity allow, and this depends mainly on the flight line spacing and used equipment. For a comprehensive classification of tectonic units and subunits, full coverage is essential. This criterion was not achieved within this first project, and leads naturally to some uncertainties. The gaps will be closed with further investigations.

These future investigations may target also subglacial environments, a continental phenomenon that occurs below ice sheets. These isolated environments are natural separated microcosms and of interest understanding evolution of fauna and flora in the antarctic region. For this purpose, the topographic maps compiled here define a good data base.

Apart from the calculation of Free-air- and Bouguer anomalies for interpretation of the crustal structure, the data are useful for the calculation of a new geoid-model (see PhD thesis (in preparation), Jan Müller, TU-Dresden). The calculated free-air anomaly provides an excellent database for improving the regional geoid by combining gravity and topographic data from aero-geophysical observations with long wavelength information from global gravity models.

Furthermore, with respect to one of the aims within the VISA project, the new datasets will contribute to the validation of new data provided by satellite missions CHAMP, GRACE and GOCE.

ACKNOWLEDGEMENTS

I sincerely thank Prof. Dr. H. Miller who gave me constant support and the opportunity to carry out this work.

The project was initiated from Dr. Wilfried Jokat. I particularly thank him for the support over many years of my work.

Special thanks go to Dr. Graeme Eagles for his continued and detailed corrections which contributed to the success of this work.

I also like to thank my close friend Dr. Tobias Boebel and OPTIMARE Sensorsysteme AG, not only for the instrumentation support of the flight campaigns as well as Tobias fundamental work with airborne gravity at the Alfred Wegener Institute.

Furthermore, thanks go to Dr. Oliver Ritzmann, Dr. Vera Schlindwein and Dr. Matthias Koenig for suggestions and corrections of the final thesis.

Dr. Joachim Jacobs introduced me to the amazing geology of the Antarctic continent. His work is strongly dedicated to Dronning Maud Land and provided substantial models for understanding geological history.

Many thanks go to the Bundesanstalt für Geowissenschaften und Rohstoffe (BGR), to Dr. Uwe Meyer, for his software support, to Dr. Gernot Reitmayer for his help referring to gravity data, to Dr. Detlef Damaske for his discussion of magnetic data interpretation and Felix Goldmann for technical assistance in data processing.

Colleagues from TU-Dresden, Planetary Geodesy Division, i.e. Dr. Mirko Scheinert, Axel Rühlke and Jan Müller, are thanked for their teaching of processing GPS data.

Thanks to all the members of the working groups of geophysics and glaciology, particularly Dr. Alfons Eckstaller, Dr. Daniel Steinhage and Christine Wesche, for all the advice and support during the normal daily work.

Preparation of this work was supported by the Deutsche Forschungsgemeinschaft (DFG) through the VISA Project, founded under grants Di 473/17-1 and Jo 191/8-1.

References

Aleshkova, N., Golynsky, A., Kurinin, R., Mandrikov, V. (1998). *Gravity mapping in the southern Weddell Sea region*, Abschlussbericht zum Forschungsprojekt BMFT 03F08GUS, Teilprojekt 4.

Bamber, J.L. and Blindschadler, R.A. (1997). *An improved elevation dataset for climate and ice-sheet modelling: Validation with satellite imagery*, Anals of Glaciology **25**: 439–444.

Bayer, B. (2007). *Untersuchungen der Lithosphäre des Dronning Maud Landes, Antarktis, mit geophysikalischen Methoden*, PhD thesis, University Bremen, Bremen, Germany.

Bell, R., Childers, V., Arko, R., Blankenship, D. and Brozena, J. (1999). *Airborne gravity and precise positioning for geological applications*, Journal of Geophysical Research **104** (7): 15281–15292.

Boebel, T. (2000). *Flugzeuggestützte Topographie- und Schweremessungen: Messsystem und Anwendung auf die Region Framstrasse, Spitsbergen und Nordostgrönland*, PhD thesis, University of Bremen, Bremen, Germany.

Brozena, J.M. (1991). *Airborne gravity, topographic and magnetic mapping of an entire continent*, in Colombo, O.L., From Mars to Greenland Charting Gravity with Space and Airborne Instruments, Band **110**, IAG Symposium Series, Springer, Berlin,: 203–214.

Brozena, J.M., and Peters, M.F. (1988). *An airborne gravity study of eastern North Carolina*, Geophysics **52**: 245–252.

Childers, V., Bell, R. and Brozena, J. (1999). *Airborne gravimetry: An investigation of filtering*, Geophysics **64** (1): 61–69.

Cox, K.G. (1992). *Karoo igneous activity, and the early stages of the break-up of gondwanaland*, in: Storey, B.C., Alabaster, T. and Pankhurst, R.J. (eds), *Magmatism and the Causes of Continental Break-up*, Special Publication **68**, Geological Society London, pp. 137–148.

Damaske, G., Marcinkowski, V., Möller, H.D. (2005). *Aeromagnetic survey in Central Dronning Maud Land, East Antarctica, during the 1995/1996 GeoMaud*

expedition: Layout, execution and data processing, Geologisches Jahrbuch, **B97**:pp. 53–83.

Ferraccioli, F., Jones, P., Curtis, M., Leat, P. and Riley, I. (2005). *Tectonic and magmatic patterns in the Jutulstraumen rift (?) region, East Antarctica, as imaged by high-resolution aeromagnetic data*, Earth Planets and Space **57** (8): 767–780.

Ferraccioli, F., Jones, P.C., Curtis, M.L. and Leat, P.T. (2005). *Subglacial imprints of early Gondwana break-up as identified from high resolution aerogeophysical data over Western Dronning Maud Land, East Antarctica*, Terra Nova **17**: 573–779.

Golynsky, A. and Jacobs, J. (2001). *Grenville-age versus Pan-African magnetic anomaly imprints in Western Dronning Maud Land, East Antarctica*, Journal of Geology **109**: 136–142.

Golynsky, A.V. (2007). *Magnetic anomalies in East Antarctica: a window on major tectonic provinces and their boundaries*, in: Cooper, A.K. and Raymond, C.R. et al. (eds), *Proceedings of the 10th ISAES*, USGS Open-File Report.

Golynsky, A.V. and Aleshkova, N.D. (2000). *New aspects of crustal structure in the Weddell Sea region from aeromagnetic studies*, Polarforschung **67** (3): 133–141.

Golynsky, A.V., Chiappini, M., Damaske, D., Ferraccioli, F., Ferris, J., Finn, C., Ghidella, M., Isihara, T., Johnson, A., Kim, H.R., Kovacs, L., LaBrecque, J.L., Masolov, V.N., Nogi, Y., Purucker, M., Taylor, P. and Torta, M. (2001). *ADMAP - Magnetic anomaly map of the Antarctic, 1:10000000 scale map, BAS (Misc.)10*, Morris, P. and von Frese, R. (eds), British Antarctic Survey.

Golynsky, A.V., Grikurov, G.E. and Kamenev, E.N. (2000). *Geological significance of regional magnetic anomalies in Coats Land and Western Dronning Maud Land*, Polarforschung **67** (3): 91–99.

Groenewald, P., Grantham, G. and Watkeys, M. (1991). *Geological evidence for a proterozoic to mesozoic link between southeastern Africa and Dronning Maud Land, Antarctica*, Journal of Geological Society, London **148**: 1115–1123.

Harlan, R.B. (1968). *Eotvos corrections for airborne gravimetry*, Journal of Geophysical Research **73** (14): 4675–4679.

Jacobs, J. and Thomas, R.J. (2004). *Himalayan-type indenter-escape tectonics model for the southern part of the late neoproterozoic-early paleozoic East African Antarctic Orogen*, Geology **32** (8): 721–724.

Jacobs, J., Bauer, W., Fanning, C.M. (2003a). *Timing of grenville-age vs. pan-african medium- to high grade metamorphism in Western Dronning Maud Land (East Antarctica) and significance for correlations in Rodinia and Gondwana*, Precambrian Research **125**: 1–20.

Jacobs, J., Bauer, W., Spaeth, G., Thomas, R. J. and Weber, K. (1996). *Lithology and structure of the Grenville-aged (? 1.1 Ga) basement of Heimefrontfjella (East Antarctica)*, Geologische Rundschau **85** (4): 800–821.

Jacobs, J., Klemd, R., Fanning, C.M., Bauer, W., and Colombo, F. (2003b). *Extensional collapse of the late neoproterozoic-early palaeozoic East African-Antarctic Orogen in Central Dronning Maud Land, East Antarctica*, Geological Society, Special Publication pp. 271–287.

Jokat, W. (2004). *East antarctic tectonics and sedimentation history from 40W to 60E*, Marine Geophysical Researches **25** (3-4): 181–182.

Jokat, W., Boebel, T., König, M. and Meyer, U. (2003). *Timing and geometry of early Gondwana break-up*, Journal of Geophysical Research **108** (B9): 2428.

Kane, M.F. (1962). *A comprehensive system of terrain correction using a digital computer*, Geophysics **27** (4).

Kirchner, M. (2002). *Kinematische Modellierung von GPS-Referenzstationen auf Eis für flugzeuggestützte Messvorhaben*, Diploma, Technical University Dresden, Dresden, Germany.

König, M. (2005) *Processing of shipborne magnetometer data and revision of the timing and geometry of the Mesozoic break-up of Gondwana*. PhD thesis, University Bremen, Bremen, Germany.

Kollersberger, T. (2005). *Anwendung von Krümmungsattributen zur Visualisierung und Interpretation von Potentialfeldern und Gradienten*, Diploma, Freie Universität Berlin, Berlin, Germany.

LaCoste, L. (1967). *Measurement of gravity at sea and in the air*, Reviews of Geophysics **5** (4): 477–526.

LaCoste, L., Ford, J., Bowless, R., and Archer, K. (1982). *Gravity measurements in an airplane using state-of-the-art navigation and altimetry*, Geophysics **47** (5): 832–838.

LaCoste, L.J.B. (1988). *The zero-length spring gravity meter*, Geophysics **7**: 20–21.

LaFehr, T. and Nettleton, L. (1967). *Quantitative evaluation of a stabilized platform shipboard gravity meter*, Geophysics **32**: 110–118.

LaFehr, T.R. (1991). *An exact solution for the gravity curvature (bullard b) correction*, Geophysics **56**: 1179–1184.

Lythe, M. B., Vaughan, D. G. (2001). *BEDMAP: A new ice thickness and subglacial topographic model of Antarctica*, Journal of Geophysical Research **106(B6)** (11): 335–352.

Meyer, U., Boedecker, G., Pflug, H. (2003). *Angel - airborne navigation and gravimetry ensembles and laboraty - introduction and first airborne tests*, Scientific Technical Report, GFZ-Potsdam.

Meyer, U., and Heyde, I. (2004). *Entwicklung und Anwendung von aerogravimetrischem Messsystemen*, DGG Kolloqium Aerogeophysik, pp. 17–44.

Nagy, D. (1966). *The gravitational attraction of a right rectangular prism*, Geophysics **31**(2).

Nettleton, L., LaCoste, L., and Harrison, C. (1960). *Tests of an airborne gravity meter*, Geophysics **25** (1): 181–202.

Olesen, A.V. and Fosberg, R. (1997). *Airborne gravimetry using Lacoste & Romberg gravimeter- An error analysis*, Geomatics and Navigation, Intern. Symp. on Kinematic Systems in Geodesy, pp. 613–617.

Piech, H.J. (2005). *Present Knowledge of the Geology of Central Dronning Maud Land, East Antarctica: Main results of the 1995/1996 GeoMaud expedition*, Geologisches Jahrbuch **B97**: 341–408.

Piech, H.-J., Bauer, W., Piazolo, S., Jacobs, J., Markl, G. (2005). *Comparison of the Geology of Central Dronning Maud Land, East Antarctica, with other areas of the Gondwana Supercontinent*, Geologisches Jahrbuch **B97**: 309–340.

Reid, A.B., Allsop, J.M., Granser, H., Millet, A.J., Somerton, I.W. (1990). *Magnetic interpretation in the three dimensions using Euler Deconvolution*, Geophysics **55**: 80–91.

Reitmayr, G. (2005). *Gravity survey in Central Dronning Maud Land, East Antarctica, during the 1995/1996 GeoMaud expedition*, Geologisches Jahrbuch **B97**: 141–164.

Roberts, A. (2001). *Curvature attributes and their application to 3d interpreted horizons*, First Break **19** (2): 285–100.

Roest, W.R., Verhoef, J., Pilkington, M. (1992). *Magnetic interpretation using the 3d analytic signal*, Geophysics **57** (1): 116–125.

Spector, A. and Grant, F.S. (1970). *Statistical models for interpreting aeromagnetic data*, Geophysics **35** (2): 293–302.

Steinhage, D. (2001). *Beiträge aus geophysikalischen Messungen in Dronning Maud Land, Antarktis, zur Auffindung eines optimalen Bohrpunktes für eine Eiskerntiefbohrung*, PhD thesis, University of Bremen, Bremen, Germany.

Swain, C. (1996). *Horizontal acceleration corrections in airborne gravimetry*, Geophysics **61** (1): 273–276.

Thompson, D.T. (1982). *Euldph: A new techniquw for making computer-assisted depth estimates from magnetic data*, Geophysics **47**: 31–37.

Torge, W. (1989). *Gravimetry*, Walter de Gruyter, Berlin, 465pp.

Torge, W. (1991). *Geodesy*, Walter de Gruyter, Berlin, 264pp.

Valliant, H. (1991). *Gravity meter calibration at LaCoste & Romberg*, Geophysics **56**: 705–711.

Valliant, H. (1992). *The LaCoste & Romberg Air/Sea Gravity Meter: An overview*, In Hydrocarbons, Band 1, CRC Press, Inc.

Valliant, H. and LaCoste, L. (1976). *Theory and evaluation of the Lacoste & Romberg three-axis inertial platform for marine gravimetry*, Geophysics **41**: 459–467.

Wesche, C., Riedel, S., Steinhage, D. (submitted). *Precise surface topography of the grounded ice tounge at the Ekstroemisen, Antarctica, based on several geophysical data sets*, Journal of Photogrammetry and Remote Sensing.

Wesche, C., Riedel, S., Steinhage, D. Eisen, O. and Oerter, H. (in prep.). *An improved DEM and refined ices divides location for Central Dronning Maud Land, Antarctica*, Journal of Glaciology.

List of Tables

List of Figures

APPENDIX A

DGPS SETTINGS

A.1 Parameters

Table A.1: DGPS processing parameters, listed for 1 s and 30 s data. Optionally the standard settings are listed.

settings	parameter	1 s		30 s	standard
primary	elevation mask	15°		10°/15°	13°
	ephemerides		precise		broadcast
	solution		float/fixed		fixed
static	min. observation				120 s
	max. baselength broadcast		5 km		200 km
	max. baselength precise				2000 km
kinematic	min. time reference	3600 s		600 s	600 s
	min. time stat. init	600 s		120 s	120 s
	min. init try				3
	min. OTF time		600 s		200 s
gobal	frequency				L1
	max. phase jump	10 s		300 s	600 s
	max. iterations				10
	max. time calc.	120 min		90 min	30 min
quality	dismiss, if RMS > ...		0.2 m		0.03 m
	dismiss, if variance < ...				1.5
	dismiss, if ref-variance > ...		20	10	
	RMS			3.5	
troposphere	modell		Niell		Hopefield
	interval		2h		2h
ionosphere	solution at		5 km		10 km
OTF	method				optimal

For all calculations, the use of the precise ephemerides was applied. The final observations include observations at an elevation mask of 10°. Irregularities are observed due to this, and so the elevation mask settings are changed to 15°. Forcing the program to calculate a fixed solution was not always possible. Due to this, a float solution was used. Phase jumps are only corrected if the disturbing effect is longer then ten epochs (only static). The tropospheric model of Niell was used, including a parameter interval of two hours. The ionosphere free linear combination of the measurements will be used at baselength of 5 km.

APPENDIX B

GRAVITY READINGS and TYING-PROCESS

B.1 Tying VISA I

Table B.1: Gravity base readings, VISA 1.

date	station	land-reading [mGal]	S56-reading [mGal]
01.12.2001	Poller94	3159.48	-
01.12.2001	Poller94	3159.55	-
01.12.2001	Polarstern	3158.67	-
02.01.2002	Neumayer	6249.80	12771.9
02.01.2002	Neumayer	6249.80	12771.1
04.01.2002	Neumayer	-	12771.9
04.01.2002	Neumayer	-	12770.9
04.01.2002	Neumayer	-	12771.3
04.01.2002	Neumayer	-	12770.4
05.01.2002	Neumayer	-	12770.4
07.01.2002	Neumayer	-	12771.2
08.01.2002	Neumayer	6249.91	12768.7
08.01.2002	Neumayer	-	12769.1
10.01.2002	Neumayer	-	12768.4
13.01.2002	E-Base	-	12743.9
14.01.2002	E-base	-	12744.1
16.01.2002	E-base	-	12743.2
16.01.2002	E-base	-	12743.4
18.01.2002	E-base	-	12742.0
21.01.2002	E-base	-	12741.5
21.01.2002	E-base	-	12742.0
21.01.2002	E-base	-	12742.1
22.01.2002	E-base	6224.99	12741.6
23.01.2002	E-base	-	12740.9
23.01.2002	E-base	-	12740.5
24.01.2002	E-base	-	12740.6
25.01.2002	E-base	-	12740.2
26.01.2002	E-base	-	12739.8
27.01.2002	E-base	6225.06	12739.1
27.01.2002	E-base	-	12737.4
28.01.2002	E-base	-	12737.4
28.01.2002	E-base	-	12739.3
29.01.2002	E-base	-	12738.8
29.01.2002	E-base	-	12739.5
09.02.2002	Neumayer	-	12763.6
09.02.2002	Neumayer	-	12763.5
12.02.2002	Neumayer	-	12762.9
13.02.2002	Neumayer	-	12763.6
23.02.2002	Neumayer	6224.99	-
28.01.2002	Poller94	3160.04	-

Table B.2: Tying process, VISA I, Calculation of absolute gravity readings refers to Poller 94 station (South Africa) with an absolute g=979657.904 mGal.

station	absolute gravity value [mGal]	measured relative gravity value [mGal]
Boreas Passat	982648.49	6150.11
Neumayer Station	982748.67	6250.28
E-Base	982723.41	6225.03

Table B.3: Sensor drift, VISA I. The drift process of the S56 gravity meter was subdivided into 3 stages due to the locations and times of operations. The observed values might be too high, but take into account that both stations are situated on the ice shelf, which moves continuously by glacier flow as well as being influenced by tidal movement.

base station	observed drift [mGal]
Neumayer (9 days)	3.5
E-Base (17 days)	6.7
Neumayer (15 days)	0.7

B.2 Tying VISA II

Table B.4: Gravity base readings, VISA II.

date	station	land-reading [mGal]	S56-reading [mGal]
28.12.2002	Neumayer	-	12760.02
28.12.2002	Neumayer	-	12770.00
29.12.2002	Neumayer	-	12760.24
29.12.2002	Neumayer	-	12770.00
31.12.2002	Neumayer	6240.42	12759.88
31.12.2002	Neumayer	-	12759.44
13.01.2003	Neumayer	-	12758.32
13.01.2003	Neumayer	-	12756.90
13.01.2003	Neumayer	-	12757.64
13.01.2003	Neumayer	-	12756.30

Table B.5: Tying process, VISA II. Calculation of absolute gravity readings refers to Poller 94 station (Cape Town, South Africa) g=979657.904 mGal using readings taken the year before due to the absence of direct measurements.

station	absolute gravity value [mGal]	measured relative gravity value [mGal]
Neumayer Station	982738.83	6240.42

Table B.6: Sensor drift, VISA II. The observed drift of the S56 gravity meter, of 3.9 mGal, seems to be good in view of Neumayer Station's movement.

base station	observed drift [mGal]
Neumayer (16 days)	3.9

B.3 Tying VISA III

Table B.7: Gravity base readings, VISA III.

date	station	land-reading [mGal]	S56-reading [mGal]
22.12.2003	Novo	-	12496.20
23.12.2003	Novo	-	12495.98
23.12.2003	Novo	-	12492.58
24.12.2003	Novo	6104.93	-
25.12.2003	Novo	-	12493.78
27.12.2003	Novo	-	12491.92
29.12.2003	Novo	-	12492.36
30.12.2003	Novo	6105.01	-
06.01.2004	Sanae	-	12480.94
07.01.2004	Sanae	6095.17	12480.72
07.01.2004	Sanae	6095.06	12480.74
09.01.2004	Sanae	-	(12752.84)
09.01.2004	Sanae	6095.17	12480.72
09.01.2004	Sanae(seismo)	6099.63	-
10.02.2004	Novo(abs.)	6215.32	-
13.02.2004	UCT	3254.19	-

Table B.8: Tying process, VISA III. Calculation of absolute gravity readings refer to UCT station (South Africa).

station	absolute gravity value [mGal]	measured relative gravity value [mGal]
Cape Town (UCT)	979616.80	3254.19
Novo (airfield)	982467.58	6104.98
Sanae (airfield)	982457.72	6095.12

Table B.9: Tie errors, VISA III. During the same summer season, Mäkinen (2003) made some absolute g measurements. His results compare to the tying process as listed.

station	measured absolute gravity [mGal]	difference gravity value [mGal]
Novo (reference)	982579.43	1.50
Novo (airfield)	982468.35	0.77
Sanae (Seismo)	982463.47	1.23

Table B.10: Sensor drift, VISA III.

base station	observed drift [mGal]
Novo (9 days)	4.3
Sanae (4 days)	0.2

B.4 Tying VISA IV

Table B.11: Gravity base readings, VISA IV.

date	station	land-reading [mGal]	S56-reading [mGal]
26.11.2004	UCT	3255.60	-
26.11.2004	BM3	3277.68	-
17.12.2004	NM-U	6372.28	-
20.12.2004	NM	6368.42	-
20.12.2004	NM	-	12760.5
25.12.2004	NM	-	12760.8
25.12.2004	NM	-	12760.8
26.12.2004	Kottas	-	12339.6
27.12.2004	Kottas	-	12339.4
27.12.2004	Kottas	-	12399.4
28.12.2004	Kottas	-	12339.1
28.12.2004	Kottas	-	12339.3
29.12.2004	Kottas	-	12338.5
31.12.2004	Kottas	-	12337.1
02.01.2005	Kottas	-	12336.5
02.01.2005	Kottas	-	12337.1
02.01.2005	Kottas	-	12337.4
03.01.2005	Kottas	-	12340.5
03.01.2005	Kottas	-	12337.6
04.01.2005	Kottas	-	12337.0
04.01.2005	Kottas	-	12337.0
04.01.2005	Kottas	-	12336.7
05.01.2005	Kottas	-	12337.1
05.01.2005	Kottas	-	12337.6
05.01.2005	Kottas	-	12337.4
05.01.2005	Kottas	-	12336.4

Table B.12: Tying process, VISA IV. Calculation of absolute gravity readings refer to UCT station (South Africa). Measurements and calculations are done by TU-Dresden.

station	absolute gravity value [mGal]	measured relative gravity value [mGal]
Neumayer (construction)	982733.47	6372.29
Neumayer (airfield)	982729.61	6368.43
Kottas (campsite)	982311.87	-
Kottas (airfield)	982310.57	-

Table B.13: Sensor drift, VISA IV.

base station	observed drift [mGal]
Kottas-airfield (11 days)	2.9

APPENDIX C

DEPTH ESTIMATION SOLUTIONS

C.1 Source depths, VISA I

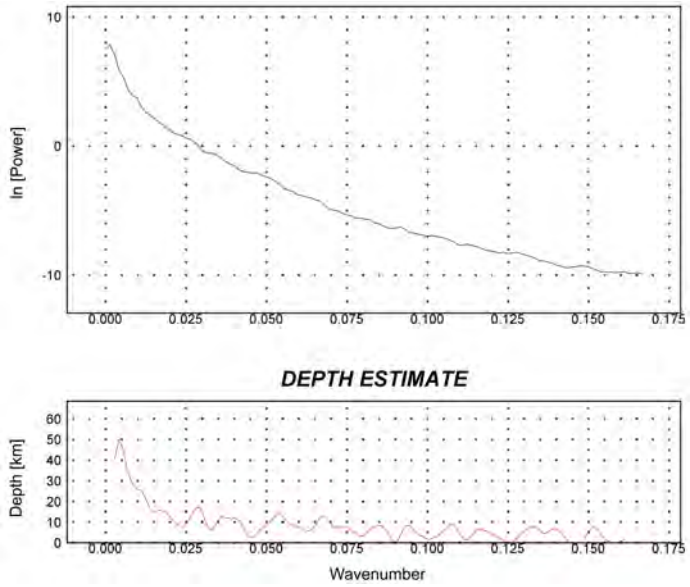

Figure C.1: Radially averaged power spectra of gravity, VISA I. Different ensembles of causative bodies or layers at depths of 27 km, 15 km and 9 km can be recognized. These will correlate with the results of receiver function analysis of seismological data, processed and interpreted by Bayer, 2007.

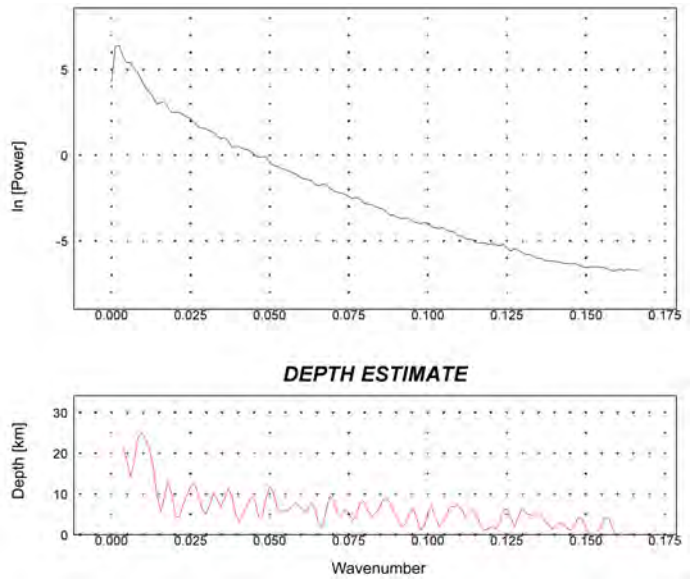

Figure C.2: Radially averaged power spectra of magnetics, VISA I. Suggestive magnetic sources at depths of 10-12 km, 8 km and 5 km.

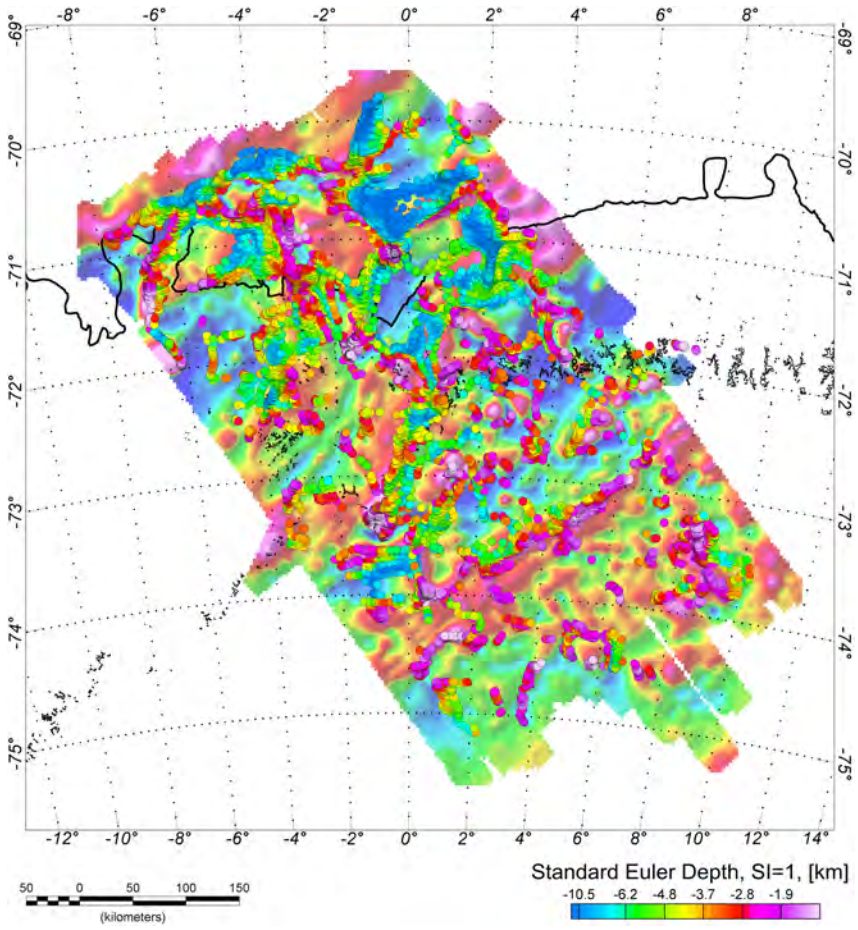

Figure C.3: Euler Deconvolution, magnetic, VISA I, for sill and dyke structures (SI=1).

C.2 Source depths, VISA II

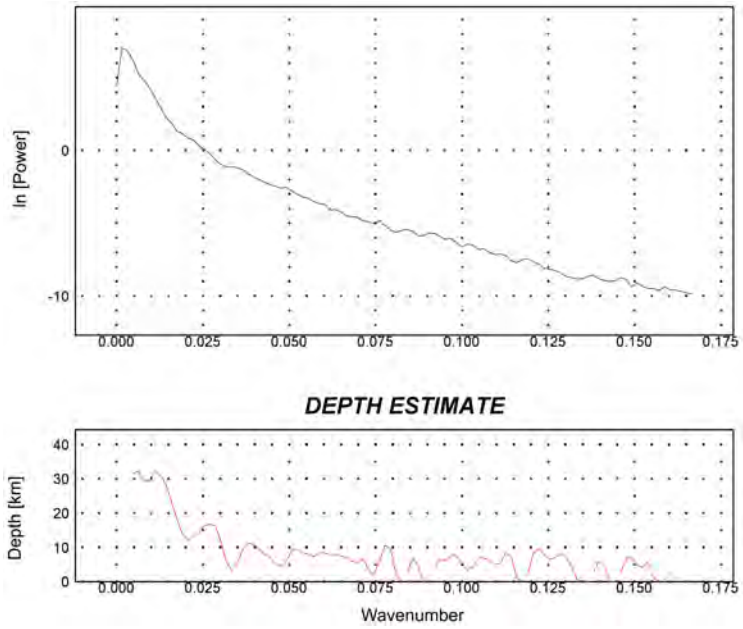

Figure C.4: Radially averaged power spectra of gravity, VISA II. Ensembles of causative bodies vary with depth and wavelength. Sources may be recognized at depths of 30 km, 16 km and 8 km.

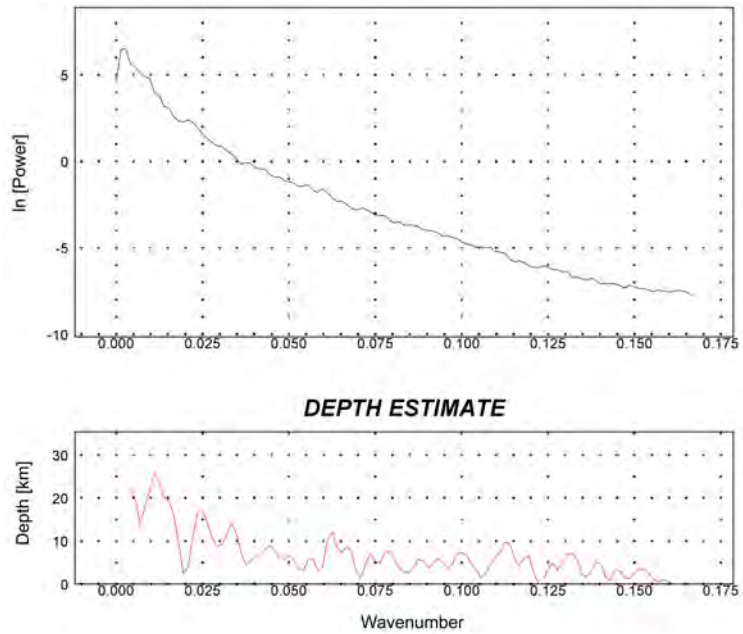

Figure C.5: Radially averaged power spectra of magnetics, VISA II., The approximate depth solution for magnetic sources suggests bodies at 15 km, 10 km, 7 km and 5 km depth.

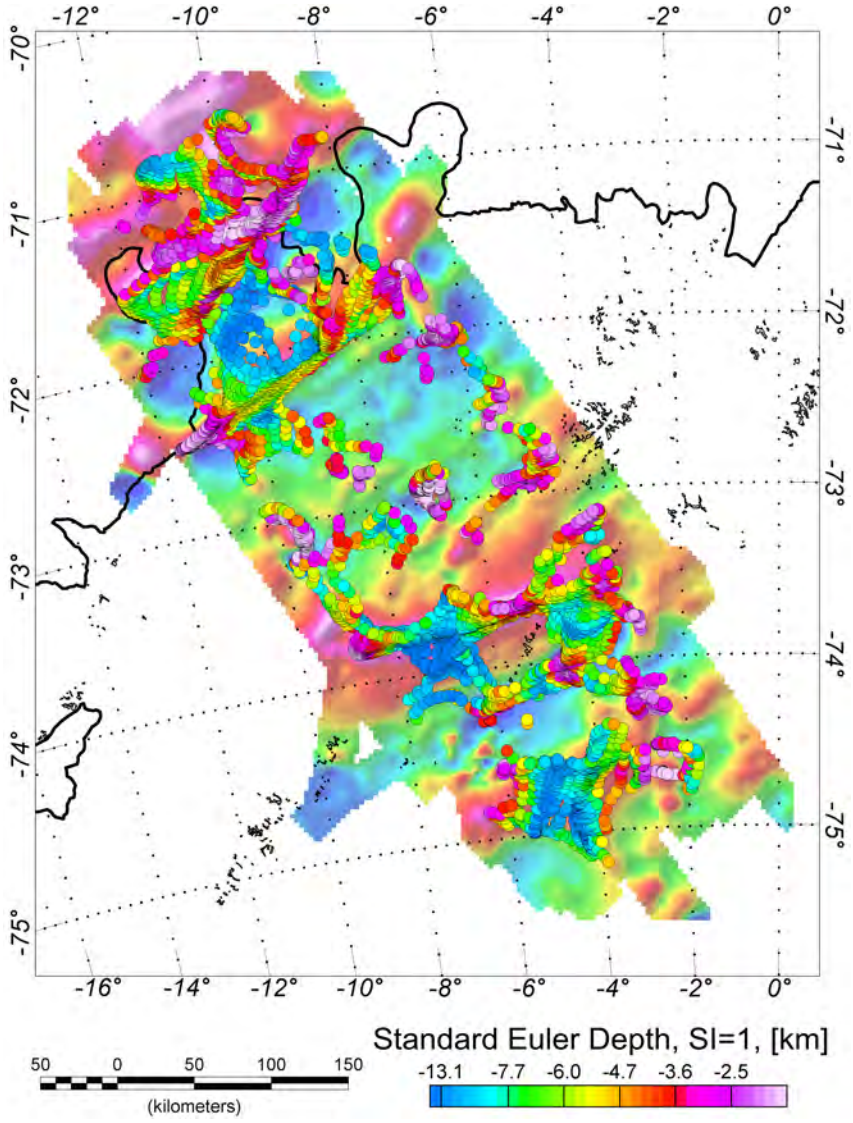

Figure C.6: Euler Deconvolution, magnetic, VISA II, for sill and dyke structures (SI=1).

C.3 Source depths, VISA III

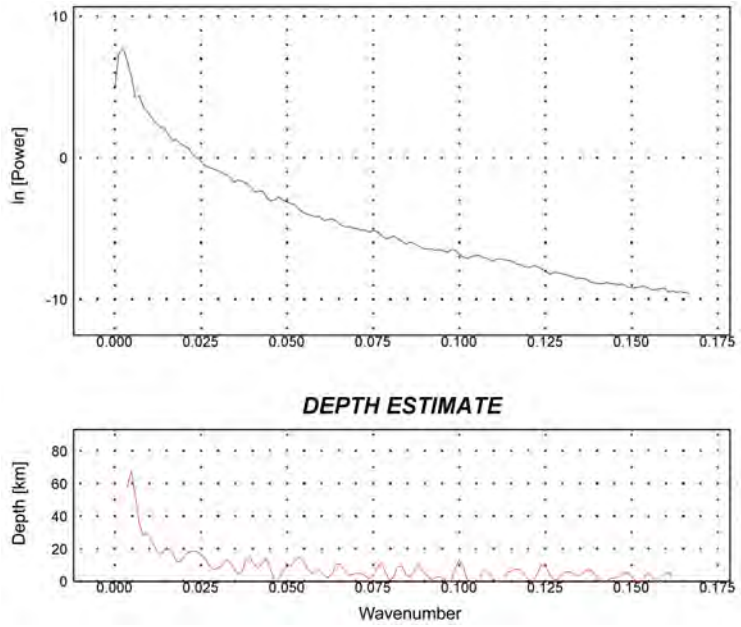

Figure C.7: Radially averaged power spectra of gravity, VISA III., Suggestive source horizons exist at 42 km, 16 km and 10 km.

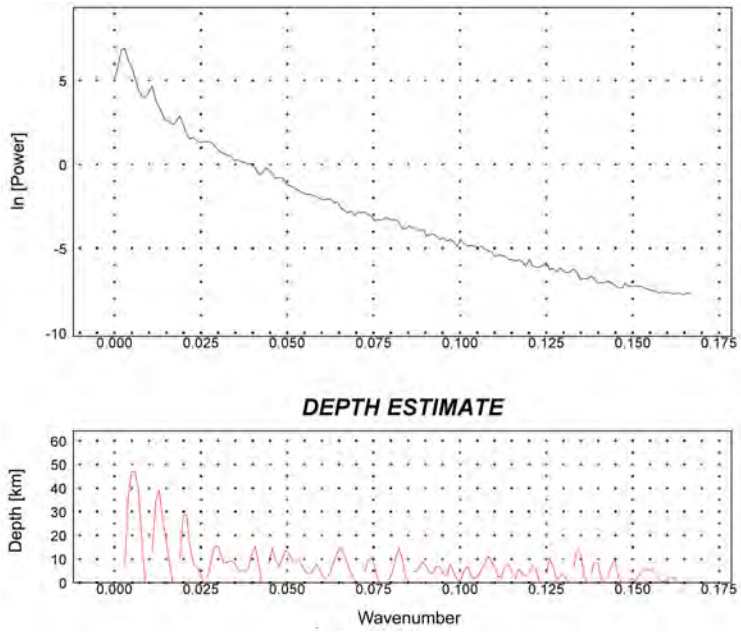

Figure C.8: Radially averaged power spectra of magnetics, VISA III. Magnetic sources are located at depths of nearly 12 km and 7 km.

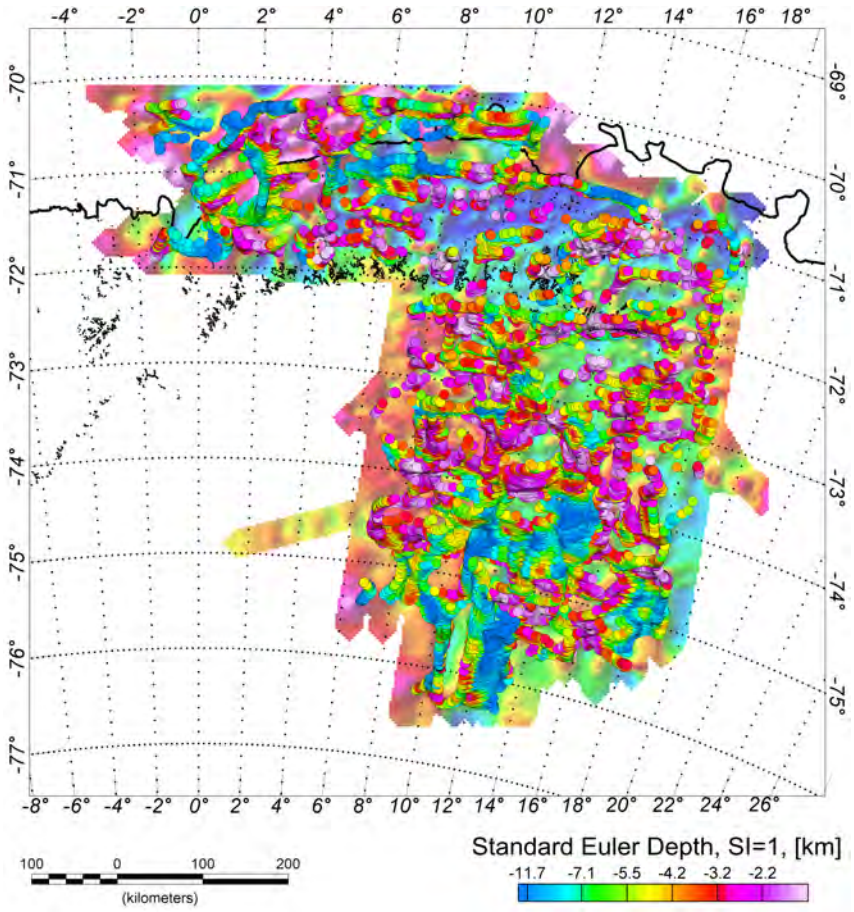

Figure C.9: Euler Deconvolution, magnetic, VISA III, for sill and dyke structures (SI=1). As mentioned, at 74° S, the results became less clear and must be interpreted with caution.

C.4 Source depths, VISA IV

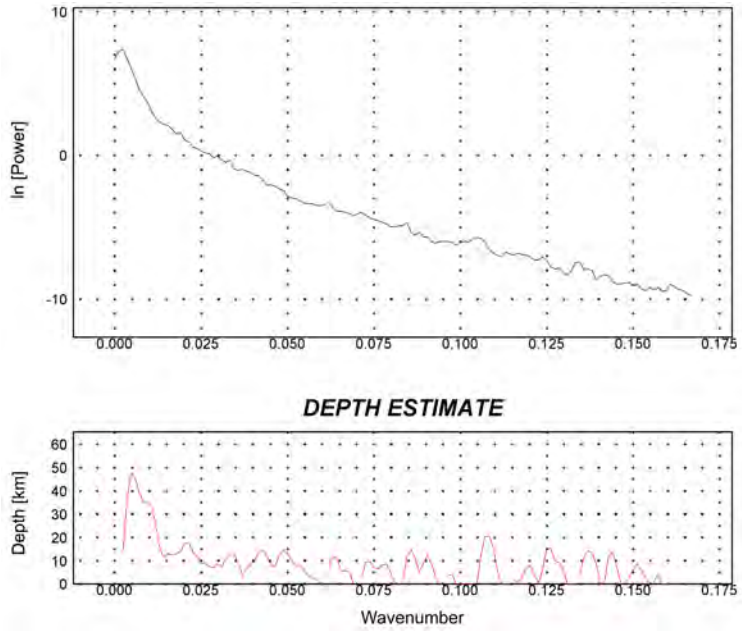

Figure C.10: Radially averaged power spectra of gravity, VISA IV, suggests horizons at 40 km, 20 km, 12 km and 5.5 km depth.

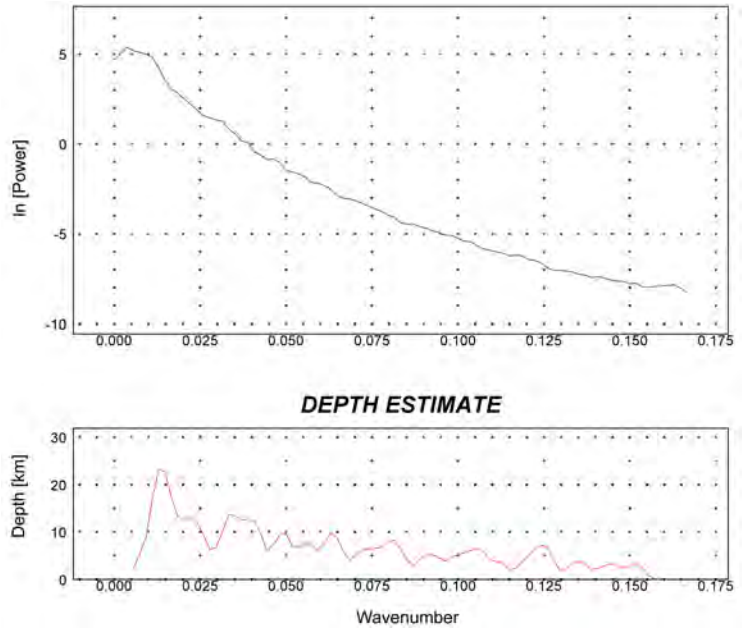

Figure C.11: Radially averaged power spectra of magnetics, VISA IV, suggests ensembles of causative magnetic sources at 12 km, 7 km and 5 km depth.

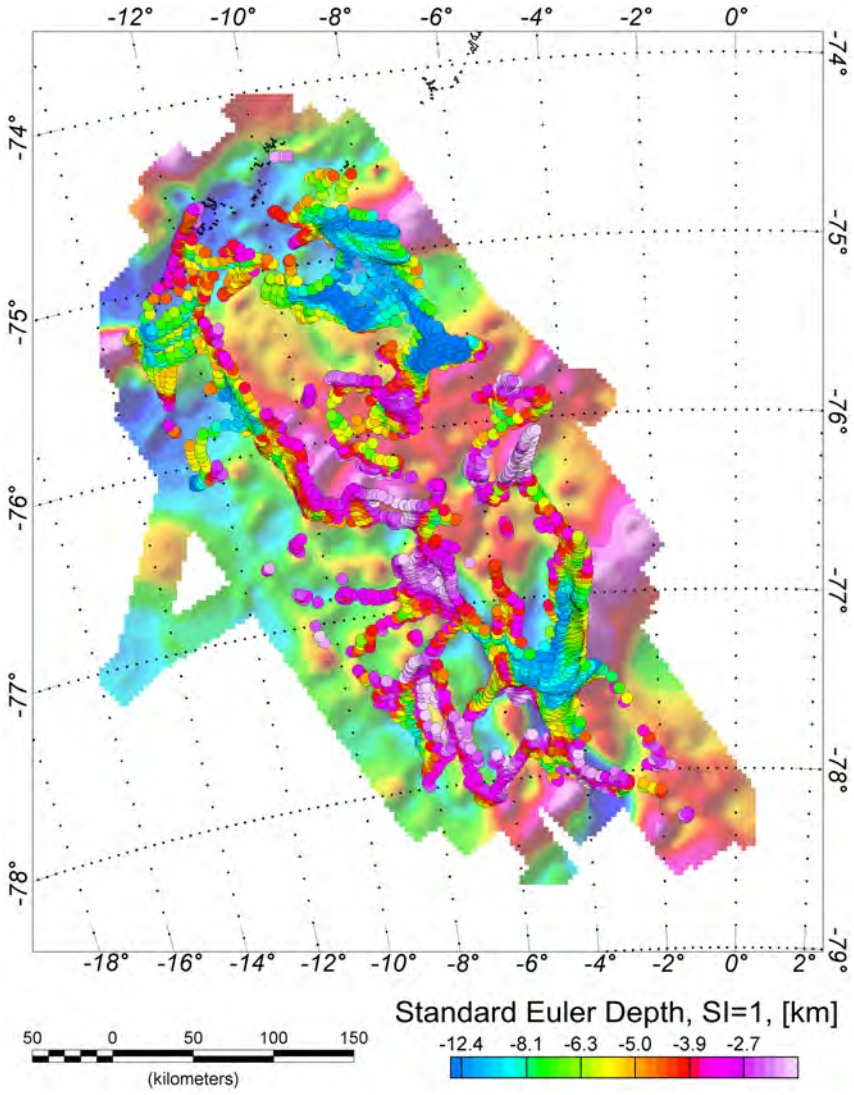

Figure C.12: Euler Deconvolution, magnetic, VISA IV, for sill and dyke structures (SI=1). Additionally, the strike directions are confirmed within this solution, especially so for the Heimefrontfjella shear zone [Jacobs and Golynsky, 2001].

.

APPENDIX D

CURVATURE DISCUSSION

D.1 Regional and local observations

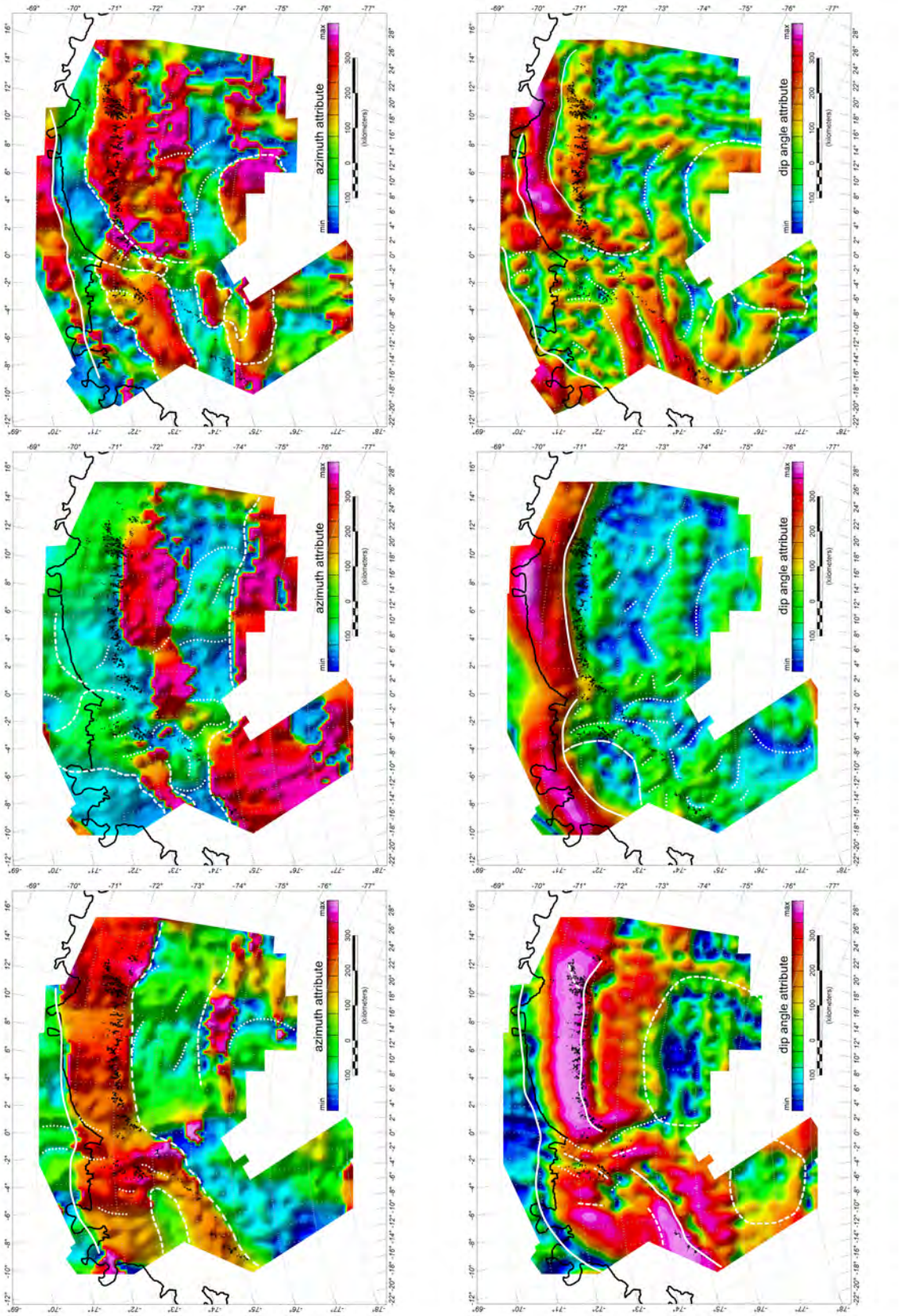

Figure D.1: Curvature attributes, regional observation (50 km window), *left:* topography, *middle:* gravity, *right:* magnetic.

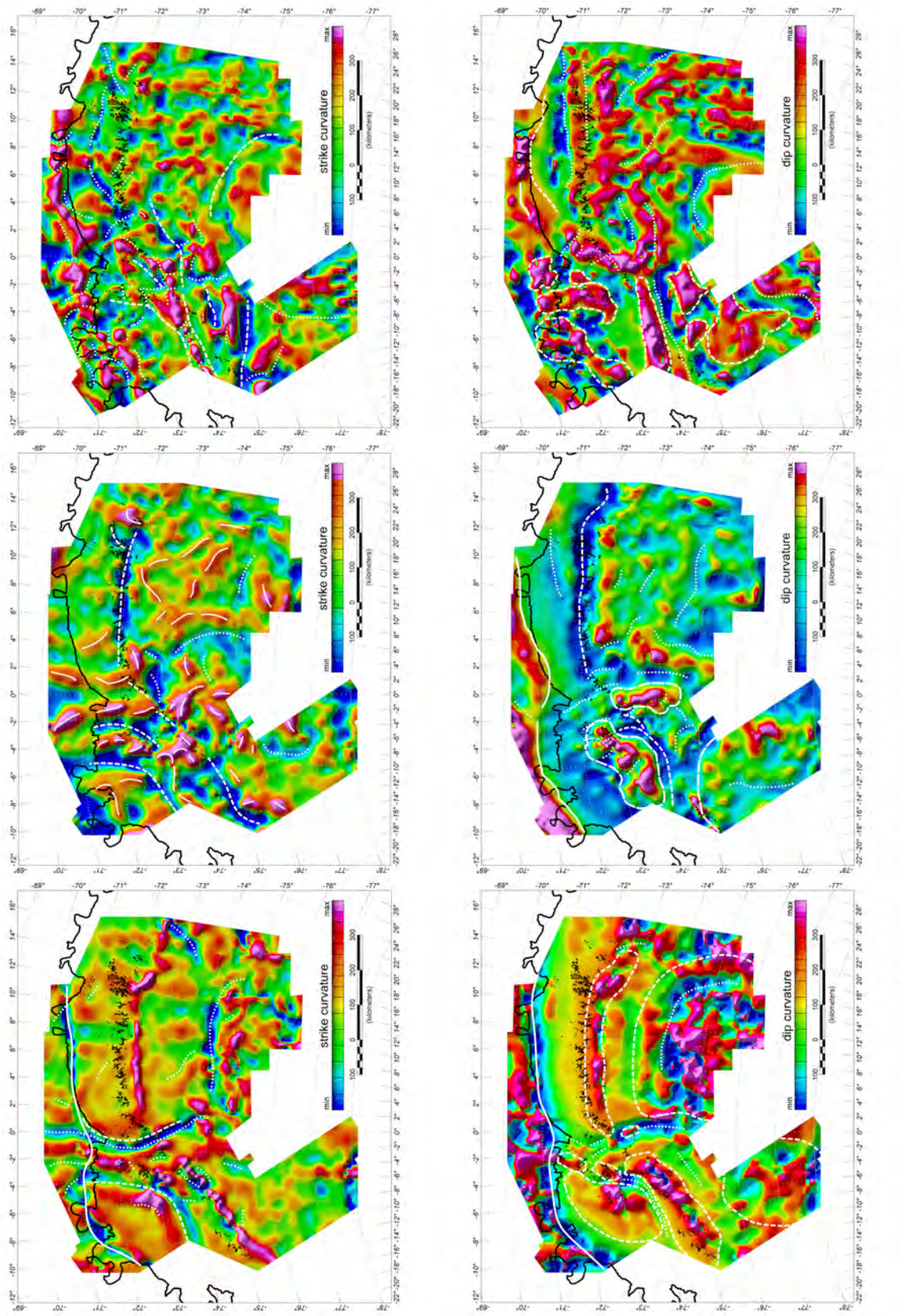

Figure D.2: Curvature attributes, regional observation (50 km window), *left:* topography, *middle:* gravity, *right:* magnetic.

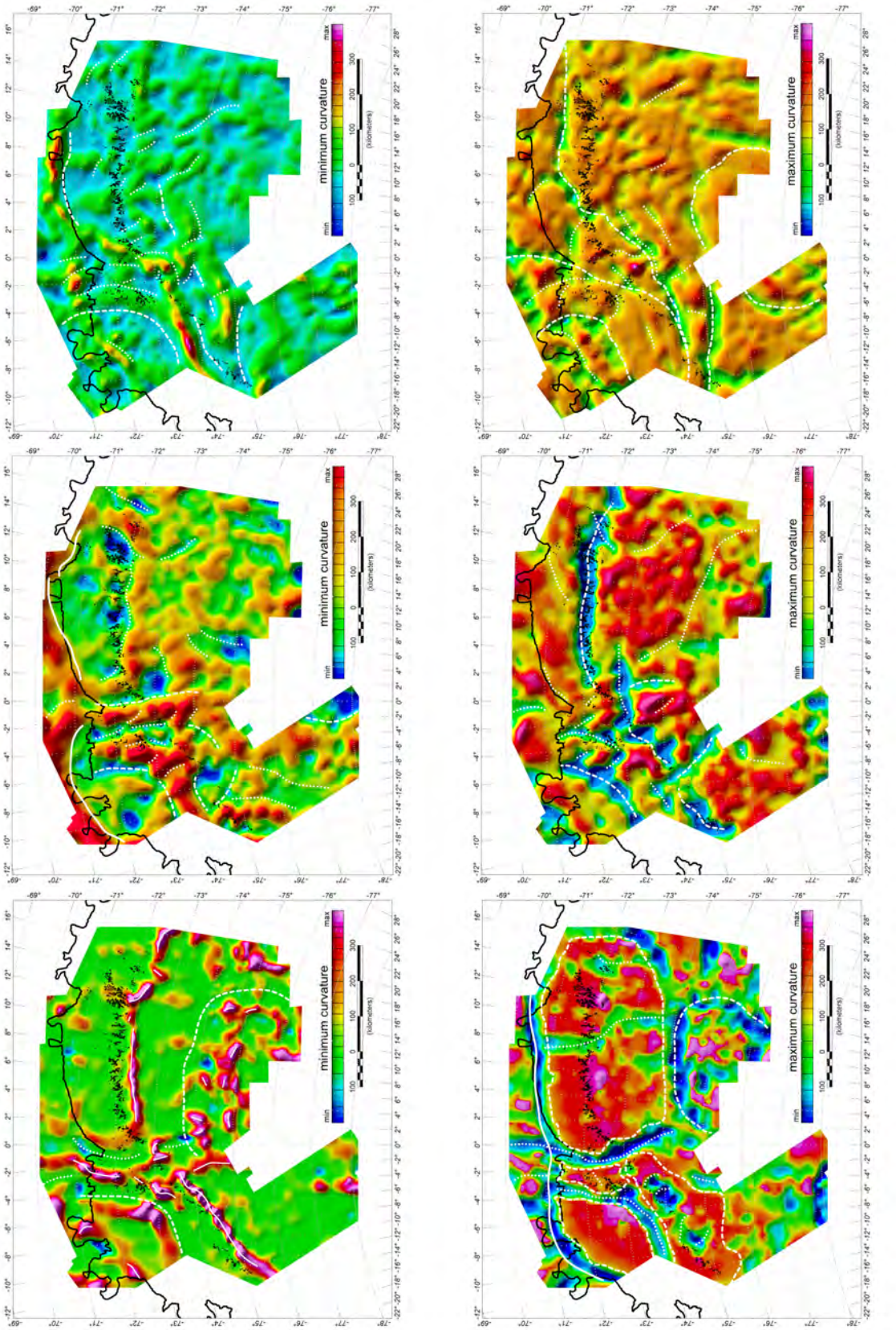

Figure D.3: Curvature attributes, regional observation (50 km window), *left:* topography, *middle:* gravity, *right:* magnetic.

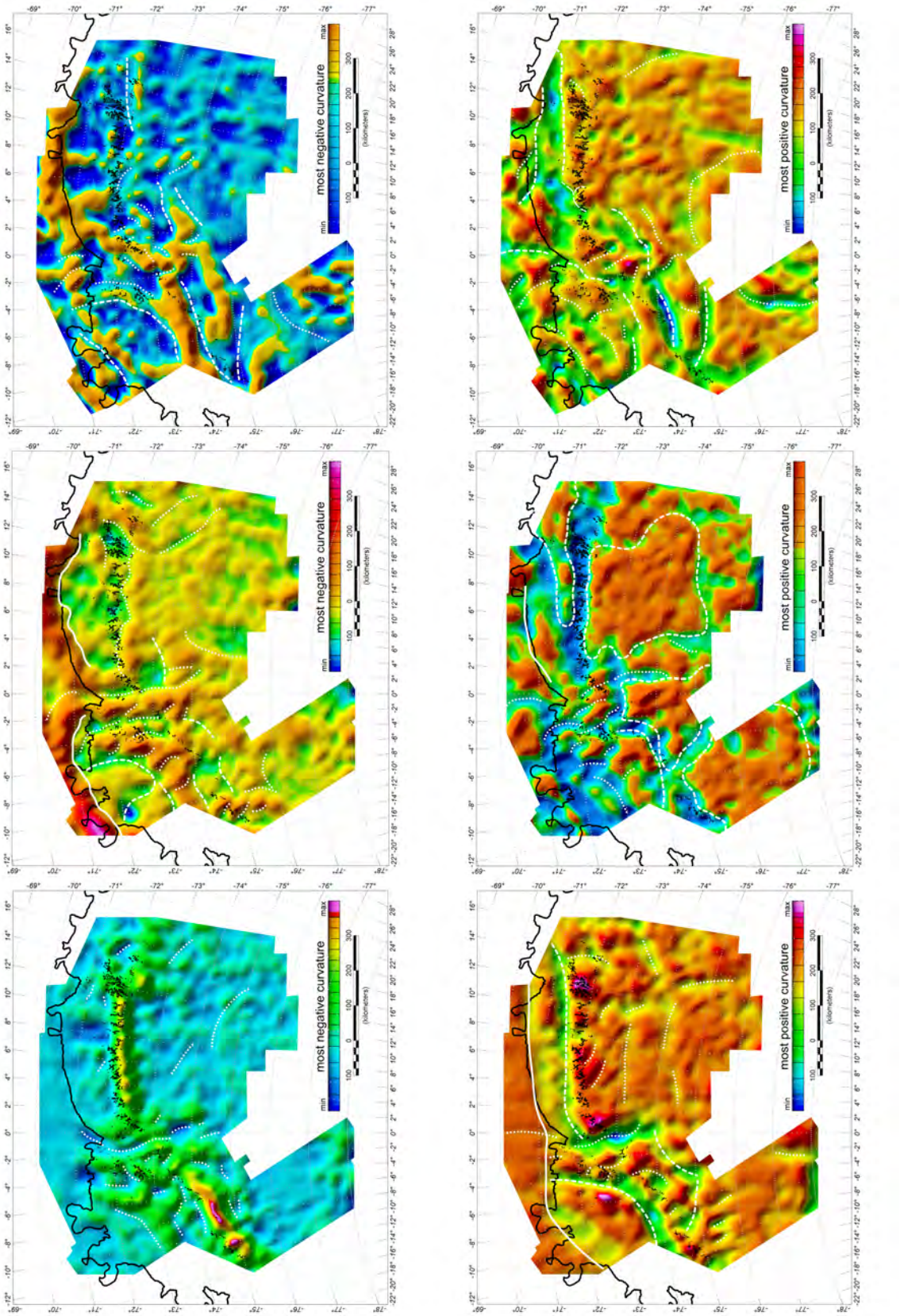

Figure D.4: Curvature attributes, regional observation (50 km window), *left:* topography, *middle:* gravity, *right:* magnetic.

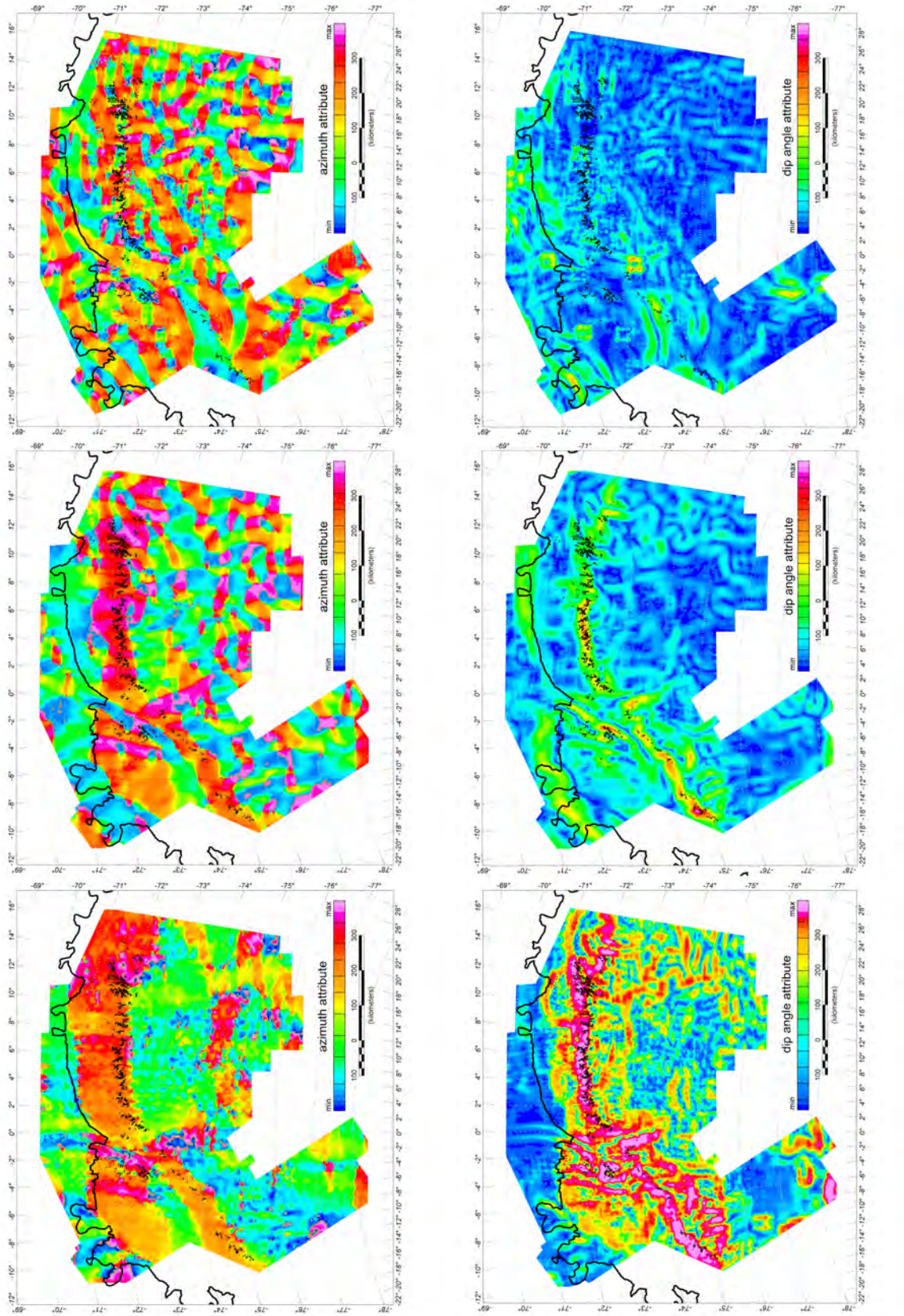

Figure D.5: Curvature attributes, local observation (10 km window), *left:* topography, *middle:* gravity, *right:* magnetic.

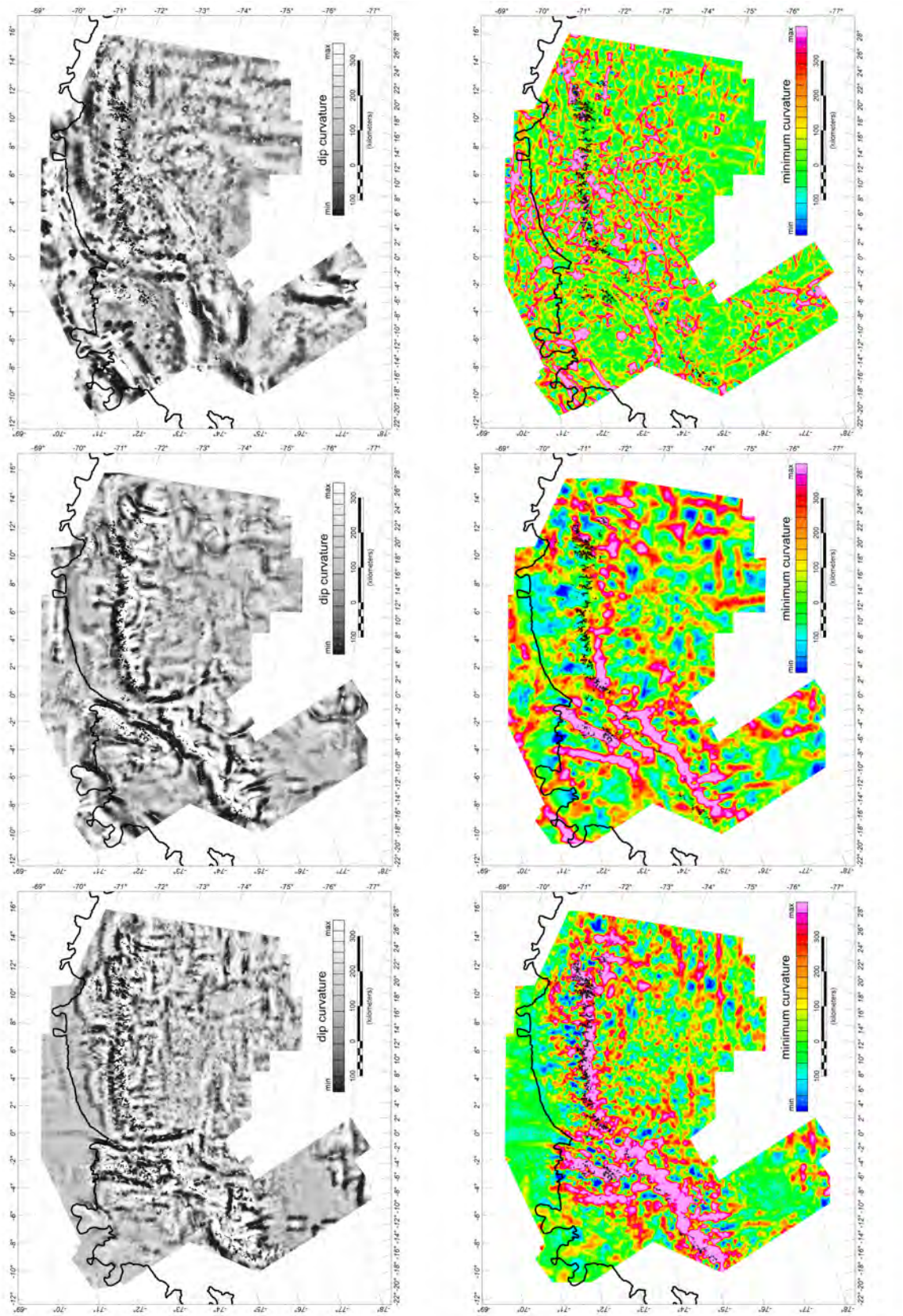

Figure D.6: Curvature attributes, local observation (10 km window), *left:* topography, *middle:* gravity, *right:* magnetic.

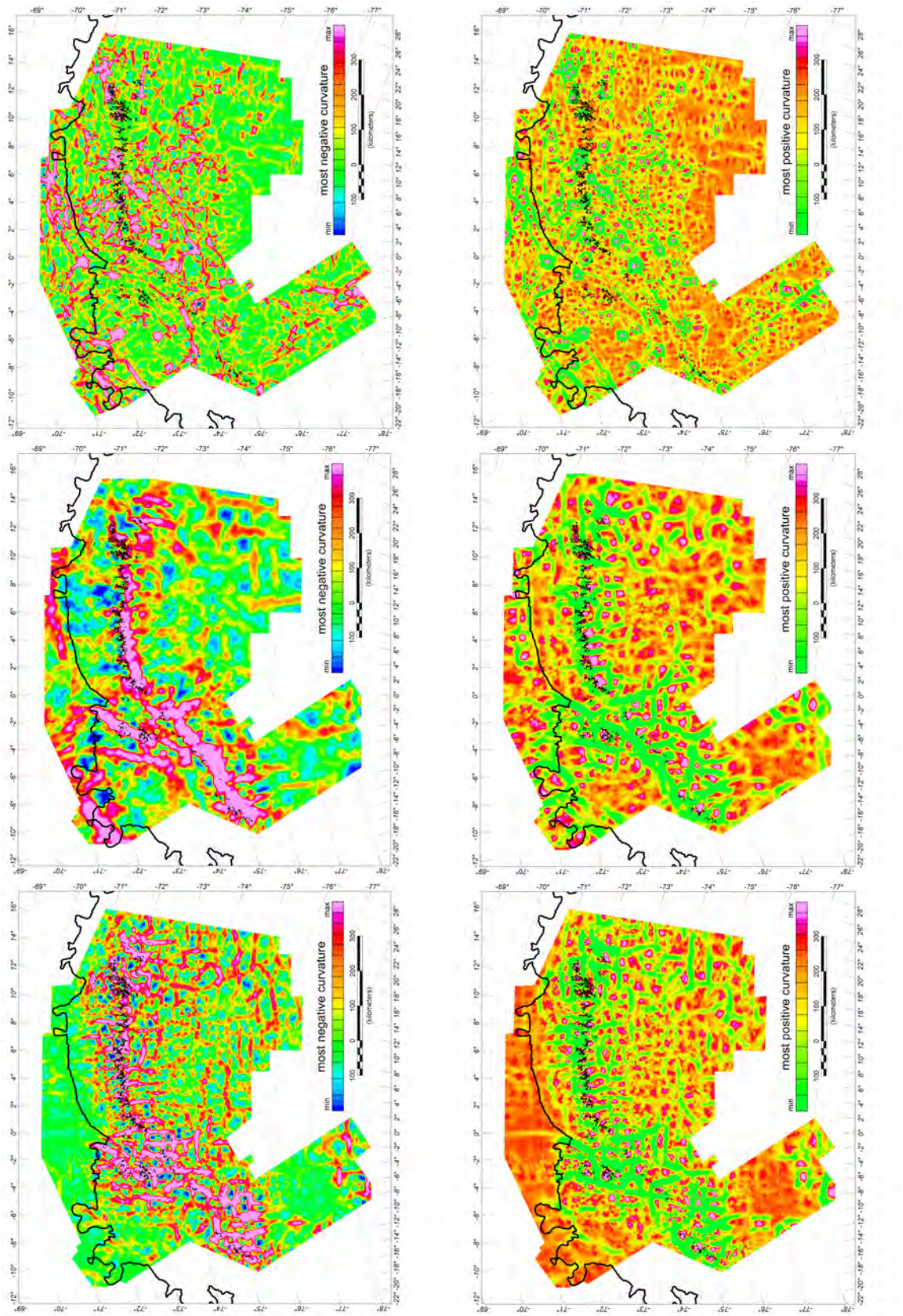

Figure D.7: Curvature attributes, local observation (10 km window), *left:* topography, *middle:* gravity, *right:* magnetic.